

RICE UNIVERSITY

**Optical Spectroscopy of Single-Walled Carbon
Nanotubes Under Extreme Conditions**

by

Thomas A. Searles, Jr.

A THESIS SUBMITTED
IN PARTIAL FULFILLMENT OF THE
REQUIREMENTS FOR THE DEGREE

Doctor of Philosophy

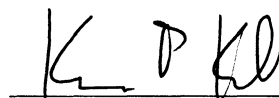
APPROVED, THESIS COMMITTEE:



Junichiro Kono, Chair
Professor of Electrical & Computer
Engineering and Physics & Astronomy



Naomi J. Halas
Stanley C. Moore Professor in Electrical
& Computer Engineering
Professor of Biomedical Engineering
Professor of Chemistry
Professor of Physics & Astronomy



Kevin F. Kelly
Associate Professor of Electrical &
Computer Engineering

Houston, Texas

August, 2011

ABSTRACT

Optical Spectroscopy of Single-Walled Carbon Nanotubes Under Extreme Conditions

by

Thomas A. Searles, Jr.

Single-walled carbon nanotubes (SWNTs) are one of the leading candidate materials to realize novel nanoscale photonic devices. In order to assess their performance characteristics as optoelectronic materials, it is crucial to examine their optical properties in highly non-equilibrium situations such as high magnetic fields, low temperatures, and under high photoexcitation. Therefore, we present our latest result on the magnetic susceptibility anisotropy of metallic carbon nanotubes due to the Aharonov-Bohm effect. Here, we performed magnetic linear dichroism on a metallic-enriched HiPco SWNT sample utilizing a 35 T Hybrid Magnet to measure absorption with light polarization both perpendicular and parallel to the magnetic field. By relating these values with the nematic order parameter for alignment, we found that the metallic carbon nanotubes do not follow a strict diameter dependence across the 7 chiralities present in our sample.

In addition to the studying the absorption properties exhibited at high magnetic field, we performed temperature-dependent (300 K to 11 K) photoluminescence (PL) on HiPco SWNTs embedded in an ι -carrageenan matrix utilizing intense fs pulses from a wavelength-tunable optical parametric amplifier. We found that for each temperature the PL intensity saturates as a function of pump fluence and the saturation

intensity increases from 300 K to a moderate temperature around 100-150 K. Within the framework of diffusion-limited exciton-exciton annihilation (EEA), we successfully estimated the density of 1D excitons in SWNTs as a function of temperature and chirality. These results coupled with our results of magnetic brightening, or an increase in PL intensity as a function of magnetic flux through each SWNT due to the Aharonov-Bohm effect, yield great promise that in the presence of a high magnetic field the density of excitons can be further increased.

Acknowledgements

I would first like to thank my Lord and savior Jesus Christ for giving me strength and guidance; and most importantly for ordering my steps in this journey called graduate school.

I am very thankful for my wife, April D. Farley, MD for her continued support and encouragement; without her I am certain that I could not have completed this stage in my career. Also a very special thanks to my parents, in-laws and sisters for being very loving and understanding during this work.

I would like to acknowledge The National Society of Black Physicists and my professors at Morehouse College showed me very early in my career that great science is done everyday by those that look like me and I am forever indebted to both organizations for their influence.

Thank you to Dr. Kono for affording me the opportunity to learn and grow as a budding young scientist in his research group. Also for the knowledge that I've gained as his student. Also, thanks to my committee for their patience and acting as true mentors to me throughout graduate school.

For all of my colleagues and friends that I've met in graduate school thank you very much for allowing me to keep my personality and for serving as a resource for borrowing things for my experiment and support for when experiments don't work.

Thanks to my funding agencies, especially the Office of Naval Research who has allowed me a freedom that only other Fellows know is possible. Also to Ms. Theresa L. Chatman for being my "auntie" in Houston and running the very busy AGEP office.

To my collaborators on this project and the many others that were not as successful, thank you for your patience and knowledge that I've gained along the way learning from you at various magnet labs around the world. I'd also like to thank Dr. Lee Johnson of NRL for the best summer intern experience of my life.

“Darkness cannot drive out darkness; only light can do that.
Hate cannot drive out hate; only love can do that.”

- Dr. Martin Luther King, Jr. '48

Contents

Abstract	ii
1 Introduction	1
2 Optical Spectroscopy of Single-Walled Carbon Nanotubes	4
2.1 Crystal Structure	4
2.2 Band Structure	8
2.3 Nanotube Optics	14
2.3.1 Optical Selection Rules for Carbon Nanotubes	14
2.3.2 Structure Assigned Photoluminescence of Carbon Nanotubes .	16
2.3.3 Excitons in Carbon Nanotubes	18
3 Magnetic Properties of Carbon Nanotubes	24
3.1 Diamagnetism of Graphite	24
3.2 Aharonov-Bohm Effect in Carbon Nanotubes	28
3.2.1 Optical Signatures of the Aharonov-Bohm Effect in Carbon Nanotubes	31
3.2.2 Magnetic Brightening of Excitons in Carbon Nanotubes	34
3.3 Novel Magnetic Properties of Single-Walled Carbon Nanotubes	37
3.3.1 Derivation of Magnetic Alignment Energy for Carbon Nanotubes	40
3.3.2 Static Magnetic Alignment in Carbon Nanotubes	42
3.3.3 Dynamic Magnetic Alignment in Carbon Nanotubes	43
3.4 Anisotropy in the Magnetic Susceptibility of Semiconductor Carbon Nanotubes	45

3.4.1	Estimation of $\Delta\chi$ using Magneto-Photoluminescence	45
3.4.2	Chirality Dependence of $\Delta\chi$ in Semiconductor Nanotubes	46
4	Magnetic Susceptibility Anisotropy in Metallic Carbon Nanotubes	49
4.1	Experimental Methods	49
4.1.1	Sample 1: (6,5)-Enriched CoMoCAT Solution	49
4.1.2	Sample 2: Armchair-Enriched HiPco Solution by Density Gradient Ultracentrifugation	53
4.1.3	Hybrid Magnet at Tsukuba Magnet Laboratory, National Institute for Materials Science	56
4.1.4	Experimental Setup	58
4.2	Large Anisotropy in the Magnetic Susceptibility of Metallic Carbon Nanotubes	59
4.2.1	Fitting Methods	62
4.2.2	Fitting Results	64
4.2.3	Discussion	67
4.3	Diameter Dependence of $\Delta\chi$ in Metallic Carbon Nanotubes	72
4.4	Future Work on Magnetic Susceptibility Anisotropy in Metallic Nanotubes	76
5	Light Emission from High Density 1D Excitons	78
5.1	Previous work on High Density 1D Excitons in Single-Walled Carbon Nanotubes	78
5.1.1	Room Temperature Upper Limit of Exciton Density in SWNTs	78
5.1.2	Diffusion Limited Exciton-Exciton Annihilation Model	81
5.1.3	Temperature Dependent Theory of High Density 1D Excitons in Single-Walled Carbon Nanotubes	83

5.2	Experimental Methods	85
5.2.1	Sample 1: HPR 188.1 HiPco Solution	85
5.2.2	Sample 2: HPR 188.1 HiPco Single-Walled Carbon Nanotubes in <i>ι</i> -carrageenan film	85
5.2.3	Nonlinear Photoluminescence Spectroscopy Experimental Setup	87
5.3	Results	90
5.3.1	Room Temperature Results	90
5.3.2	Temperature Dependent Results	93
5.4	Analysis	96
5.5	Discussion	98
5.6	Future Work	101
6	Conclusion	102
	Bibliography	103

Illustrations

2.1	Two-dimensional hexagonal lattice of graphene in real space (a) and reciprocal space (b). Sites labeled A and B represent carbon atoms contained within a parallelogram corresponding to the dotted primitive unit cell. In (b), the symmetry points of the bandstructure are labeled: Γ , K, and M in reference to the 1st Brillouin Zone (shaded). The lattice vectors $\mathbf{a}_{1,2}$ and $\mathbf{b}_{1,2}$ of this figure are defined in the text. Adapted from Ref. [?].	5
2.2	The graphene sheet corresponding to an unrolled (4,2) nanotube in real space. The chiral vector, \vec{C}_h is shown as the vector between the points O and A . Similarly the translational vector, \vec{T} is the vector from points O to B . The chiral angle is also shown as defined in the text. Adapted from Ref. [?].	7
2.3	The optical selection rules of (left) metallic ($\nu = 0$) and semiconducting (right) ($\nu = \pm 1$) nanotubes for light incident parallel to the nanotube axis. The indices n correspond to the optical transitions from optical transitions with equal momentum angular momentum.) (Ref. [5])	14
2.4	Mirror symmetry planes for the (4,0) zigzag nanotube. The horizontal mirror symmetry plane (σ_h) is transversed by the vertical mirror symmetry plane, σ_v The nanotube axis or z -axis in this figure is labeled as the 8_4 screw axis. (Ref. [6])	15

2.5	Photoluminescence excitation spectroscopy of SWNTs in solution. Each resonance corresponds to a different (n, m) depending on the structure and bandgap of the carbon nanotube (Ref. [10]).	17
2.6	Energy dispersion of singlet exciton states for the (9,4) nanotube. The $1u$ bright band (solid) is a few meV above the lowest $1g$ dark state (large dashes). The higher energy states (small dashes) are dark due to finite angular momentum. Adapted from Ref. [23]).	19
2.7	Two photon photoluminescence Excitation spectroscopy of SWNTs in solution. The red line corresponds to the energy at which the laser excitation would be equal to half of the optical transition. Each resonance falls above this energy corresponding to a difference and experimental evidence of excitons at room temperature in SWNTs. (Ref. [10]).	21
2.8	Photoluminescence intensity as a function of Temperature for different (n, m) SWNTs. For the nanotubes shown, there is a temperature maximum dependent on chirality and then a drop in intensity at lower temperature. (Ref. [44]).	22
3.1	Temperature dependence of magnetization in graphene laminates with a) parallel magnetic field and b) perpendicular magnetic field (inset). The Curie law behavior with temperature is exhibited in (b) (Ref. [49]))	25
3.2	Magnetic susceptibilities as a function of temperature of various carbon derivatives where CGS ppm/mol = emu $\times 10^{-6}$ /mol. Adapted from [2, 55].	26
3.3	Bandgap as a function of magnetic flux through the nanotube. Note that it oscillates with a period of ϕ (as defined in Section 3.2 for both semiconducting ($\nu = \pm 1$) and metallic ($\nu = 0$) nanotubes. (Ref. [8]))	29

3.4	Magneto-absorption of SWNTs above 20 T using the Hybrid magnet at NHMFL. At fields above 30 T, there is splitting that occurs in each absorption peak (Ref. [61]))	30
3.5	Near-infrared magneto-absorption in semiconducting SWNTs at high magnetic fields for (a) polarization parallel to B up to 74 T (b) B parallel and perpendicular up to 67 T. In each case, splitting occurs at fields above 55 T. Adapted from [63].	32
3.6	Schematic of Magnetic Brightening. For K-K' degeneracy and intervalley mixing results in dark state (1g) to be below the only optically-active (1u) state. After a finite B, then the distance between the two states increase causing the 1g state to become bright. Adapted from [63].	33
3.7	(a) Magneto-PL of the (9,4) SWNT up to 56T as a function of temperature (b) Magnetic Brightening as a function of magnetic field for several temperatures [43].	34
3.8	Single nanotube μ -PL at 5 K of the (a) (12,5) nanotube in the Voigt configuration (b) and (10,5) nanotube in the Faraday configuration. Note that only in the Voigt case is there the commencement of a low energy peak and that peak increases with increasing magnetic field. Adapted from [65].	35
3.9	(a) Band dispersions for metallic and semiconducting nanotubes: Wavevector as a function of Fermi energy, E_f . (b) χ_{\perp} for semiconductor ($\nu = \pm 1$) and metallic nanotubes ($\nu = 0$) as a function of E_f . (c) χ_{\parallel} for semiconductor and metallic nanotubes as a function of E_f (Ref. [66]).	37

3.10	Angular dependence of magnetic susceptibility χ for (6,6) and (6,5) SWNTs at 300 K, where $\theta = 90^\circ$ is χ_\perp and $\theta = 0^\circ$ is χ_\parallel . Note that $\Delta\chi$ for metallic nanotubes (red) is almost 5 times larger than $\Delta\chi$ for semiconductor nanotubes (blue) when $\theta = 0^\circ$	38
3.11	Single carbon nanotube in the presence of magnetic field H in real space (x, y, z coordinates).	39
3.12	Optical transmission as a function of incident polarization angle at magnetic fields up to 19 T. Fields above 10 T showed the highest alignment as the transmitted signal for those fields had the highest signal at 90° and the lowest signal at 0° . Adapted from Ref. [69]. . .	42
3.13	Transmission of laser light as a function of time at magnetic fields up to 60 T. The magnetic field pulse (yellow) is shown with the red perpendicular transmission and blue parallel transmission traces. Therefore, the increase (decrease) in transmission is directly from the alignment of the nanotubes with the magnetic field pulse. From this information, one can calculate the dynamic magnetic linear dichroism. Adapted from Ref. [70].	43
3.14	Three magneto-photoluminescence spectra of HiPco SWNTs at 0 T (bottom), 45 T with light polarized perpendicular to B (middle), and 45 T with light polarization parallel to B from Ref [71]. Note that for all chiralities present, there is a substantial redshift for each peak from 0T to 45 T. The inset shows the diameter dependence of u as defined in Section 3.4.1 and each of the cartoons correspond to the spectra highlighting the alignment of the nanotubes at each field. . .	44
3.15	$\Delta\chi$ as a function for diameter for semiconductor CoMoCAT nanotubes from Ref [73]. The data in (a) is fit to the family dependent theory shown in (b) for many nanotubes.	46

4.1	Photoluminescence excitation map of our NIST (6,5)-enriched length-sorted CoMoCAT sample. Note that there are only a few chiralities present. Also note that in the “Valley of the metals”, from excitation wavelength 400 to 500 nm, there is no luminescence present.	49
4.2	Absorbance spectra from absorption spectroscopy of our NIST (6,5)-enriched length-sorted CoMoCAT sample.	50
4.3	Absorbance spectra with respect to each colored band in the photograph (left) from a density gradient ultracentrifugation process. Note the spectra are intentionally offset to match the layer of the gradient with the most chirality separation occurring at the top layer. Adapted from [77].	52
4.4	(a) Photograph of metallic and as-produced SWNTs (b) Absorbance spectra of our DGU sample and the as-produced SWNTS. Note that the semiconductor portion of the spectra is not present in the metallic enriched SWNTs. (c) PLE of as-produced SWNTs (d) PLE of metallic-enriched sample. Adapted from [80].	54
4.5	Resistive Magnet Insert Coils of Bitter Magnet for the NIMS 35 T Hybrid Magnet, Tsukuba, Japan. There are three coils that together with the superconducting magnet allow for users to attain a maximum DC magnetic field of 35 T. Adapted from [81].	55
4.6	Ramping up-sweep of the Tsukuba Magnet Laboratory Hybrid magnet from 0 to 35 T. The initial rise is due to the increase of B from the superconducting magnet up to 14.2 T. Then there is a sharp rise to 35 T using the resistive magnets.	56
4.7	Optical path of Magnetic Linear Dichroism Spectroscopy Probe [82].	57

4.8	Magnetic linear dichroism spectroscopy of (6,5)-enriched CoMoCAT nanotubes from 0 to 35 T. Each peak corresponds to a different (n, m) nanotube. As the magnetic field is increased the absorbance increases/decreases with light polarized parallel/perpendicular to B .	58
4.9	Absorbance spectra (solid black) for 0 T and 35 T with all peaks assigned from our sample. The unpolarized isotropic absorbance (dashed red) is calculated from the magnetic field data and agrees well with that of the 0 T data.	59
4.10	Reduced linear dichroism vs Energy (eV) from measured data. The largest peak is from metallic nanotubes (6,6) and (7,4). This is opposite of the case for the Absorbance spectra from Fig. 4.9, where the semiconductors (6,5) and (6,4) dominate the spectra.	60
4.11	Fitting results for 0 T and 35 T. The data (black) is fit by the sum of each individual chirality nanotube (blue) and the addition of a susceptible offset (blue). The sum of these individual fits is shown as a red line. All spectra were fit simultaneously and data for subsequent fields was performed in the same manner.	62
4.12	Lorentzians for different chirality nanotubes at 0 and 35 T.	64
4.13	LD^r vs. Energy (eV) derived from fitting for each individual chirality nanotube in our sample. The metallic tubes (red) are higher than the semiconducting nanotubes (blue dotted).	65
4.14	S vs B for all (n, m) nanotubes present in (6,5) enriched carbon nanotubes. The lines are not fits, but are used to guide the eye. Also, the red metallic nanotubes all have higher S values as a function of B than the blue semiconductor nanotubes.	66
4.15	Theoretical model of S vs. u , where S is the nematic order parameter and u is a dimensionless quantity relating the alignment energy and the thermal energy as defined in the text.	67

- 4.16 S vs. B of (6,6) vs. (6,5). The nematic order parameter S is a measurement for the degree of alignment determined from Linear Dichroism theory. A higher S value corresponds to a higher degree of alignment. For the case shown in this figure the metallic (6,6) nanotube (red) has a higher S as a function of B than the semiconducting (6,5) nanotube (blue) 68
- 4.17 Calculated magnetic field dependence of the parallel magnetic susceptibility of (6,6) nanotube for $T = 30$ K and 300 K in units of $\chi^* = 1.46 \times 10^{-4}$ emu/mol. 69
- 4.18 Magnetic linear dichroism spectroscopy of metallic-enriched carbon nanotubes from 0 to 35 T. Each peak corresponds to a different (n,m) nanotube. As the magnetic field is increased the absorbance increases/decreases with light polarized parallel/perpendicular to B . Linear dichroism theory dictates that A_0 shown as red dotted line is equal to that of 0 T (black). 72
- 4.19 (a) Absorbance as a function of magnetic field and energy for light parallel to the magnetic field. As the field increases you can see that the absorbance peaks corresponding to the metallic carbon nanotubes in our sample increase with increasing field. (b) Absorbance as a function of magnetic field for light perpendicular to B . As the field is increased, you see a decrease in the absorbance peaks with B 73
- 4.20 S vs. B of (6,6) vs. (7,7) deduced from magnetic linear dichroism spectroscopy. The smaller diameter metallic (6,6) nanotube (red) has a higher S as a function of B than larger diameter metallic (7,7) nanotube (blue). The black dashed line corresponds to the theoretical curve for (6,6) nanotube. And the dashed navy line is for the semiconducting (6,5) nanotube. 74

5.1	Nonlinear photoluminescence excitation (PLE) spectroscopy of CoMoCAT SWNTs at low (left) and high photoexcitation (right). The low fluence PLE is similar to that of CW PLE but the high excitation PLE shows complete flattening of the excitation spectra [32].	78
5.2	PL Intensity as a function of fluence for the (7,5) nanotube at three different excitation wavelengths. There is a sharp rise at low fluence for the green triangles, or resonant excitation (654 nm). This rise results in a higher saturation value than the other wavelengths shown; 570 nm (black circle) and 615 nm (red squares) . The data is fit to a diffusion-limited exciton-exciton annihilation model. Adapted from [32].	79
5.3	Model function of ζ vs. ψ (red). At low excitation intensity, the slope = 1 representing the CW linear regime. The dashed line corresponds to the model is $\zeta = \psi$.	81
5.4	Diffusion length as a function of temperature. T^* denotes a critical temperature at which the diffusion length reaches a minimum and begins to increase to infinity at lower temperature. The dashed line represents the value of the diffusion length if dark excitons were not taken into account. Adapted from Ref. [92].	83
5.5	Photoluminescence excitation (PLE) map of HPR 188.1 HiPco solution sample. The red line corresponds to the slice of the excitation wavelength 658 nm for all experiments in Chapter 5. Also note that the (6,5) nanotube is the brightest nanotube in this sample with other small d_t chirality nanotubes present.	84
5.6	Photograph of four ι -carrageenan films after process described in the text.	86

5.7	Schematic of experimental setup for nonlinear photoluminescence spectroscopy of HiPco SWNTs. There are two sources of single wavelength excitation, CW from a 658 nm laser diode and high energy pulsed excitation from OPA. The photoluminescence, created by either form of excitation, is collected with a monochromator and detected by an InGaAs 1D camera.	87
5.8	Power dependent PL spectra for Sample 1 solution. The diode excitation (top) scales linearly for each chirality present in the sample. This is in stark contrast to the case of high photoexcitation (bottom). Note that the relative intensities are different from the diode to the OPA cases.	89
5.9	Power dependent PL for (7,5) in HPR solution. The diode excitation (navy) is completely linearly over the entire power range. Conversely, at high photoexcitation (red squares), the PL from OPA excitation saturates at high fluence. The saturation corresponds to the upper limit on exciton density at room temperature.	91
5.10	Power dependent PL spectra for HPR SWNTs embedded in polymer matrix at 15 K. The diode excitation (left) is linear up to 2 mW maximum average power. At high photoexcitation (right), PL from OPA excitation saturates at high powers. Both data are fit to extract peak are as a function of power plots.	92
5.11	Power dependent PL as a function of pump power for HPR SWNTs embedded in polymer matrix at 295, 100, and 15 K. The separation of between two traces of each at higher power indicates the efficiency of the EEA process at that temperature.	93
5.12	Normalized relative quantum efficiency for (7,5) at room temperature (left). The normalized nonradiative rate γ_{xx}/Γ_0 for (7,5) nanotube at 295 K (right). The dashed line corresponds to the line where $\gamma_{xx} = \Gamma_0$.	97

- 5.13 The normalized nonradiative rate γ_{xx}/Γ_0 for (7,5) nanotube from 295 K to 125 K (left). γ_{xx}/Γ_0 decreases until it reaches a minimum at 125 K. Temperatures < 75 K are plotted to the right with 15 K and 295 K as references in both figures. Here the dashed line corresponds to the values where $\gamma_{xx} = \Gamma_0$ (both defined in text). 98

Tables

- 2.1 Table of wavelengths and energies corresponding to E_{22} and E_{11} of (n, m) semiconductor nanotubes studied in this thesis. The values are those presented in Ref. [10]. 18
- 4.1 Comparison of values of magnetic susceptibility anisotropy from previous theoretical and experimental studies and this work. For each chirality nanotube (n, m) , the diameter d and the chiral index ν is given followed by estimated theoretical and experimental values of $\Delta\chi$. All values for $\Delta\chi$ are $\sim 10^{-5}$ emu/mol with the first two columns of $\Delta\chi_{th}$ corresponding to theoretical predictions for 30 K and 300 K respectively. For the last two columns, $\Delta\chi_{exp}$ are measured values for $\Delta\chi$ with the last column for the present work. . . 70

Chapter 1

Introduction

This work is primarily motivated by the great promise of carbon-based nanomaterials for next generation components in optoelectronics.. We chose semiconducting single-walled carbon nanotubes (SWNTs) because these direct bandgap nanostructures have the potential for creating novel light generators and detectors due to their low dimensionality and unique electronic structure. Both of these attributes are advantageous for the realization of nanoscale lasers and multi-wavelength photonic devices, respectively. Research on the optical spectroscopy of SWNTs has produced a vast literature over the past 10 years, but most of these studies have been carried out under weak excitation in the quasi-equilibrium regime. In order to realize device operating conditions, it is important to study the optical properties of SWNTs under highly non-equilibrium conditions, or extreme conditions, such as high photoexcitation, high magnetic fields, and low temperatures.

The magnetic properties of SWNTs are unlike any other graphene derivative. Graphite is widely known as one of the strongest diamagnetic materials in nature. This magnetism is due to the induced ring currents exhibited by the carbon atoms of the benzene rings in each layer of graphene [1]. For any graphene allotropes with similar benzene structure, like many carbon nanomaterials including SWNTs, it has

also been found that they exhibit strong diamagnetism [2]. But SWNTs have an additional component as a result of Aharnov-Bohm physics, that comes into play when they are in the presence of a parallel magnetic field. At a finite B field, the magnetic field flux thru the carbon nanotube causes a change in the bandstructure. For the case of a metallic nanotube, the band gap begins to increase resulting in an unusual large orbital paramagnetism that increases with higher B and alignment of the SWNT in the direction of B . This opening as a function of magnetic field is opposite for metallic carbon nanotubes and semiconducting ones. This thesis includes optical spectroscopy at high magnetic fields in the form of magnetic linear dichroism spectroscopy that unfolds this phenomenon for the first time.

Another aspect of this dissertation work, which is related to the development of a carbon nanotube based laser/gain medium, is the emission from high density 1D excitons in semiconducting carbon nanotubes under high photoexcitation. It was previously found that this emission at room temperature saturates as a function of pump laser intensity. The saturation at room Temperature indicates very efficient nonradiative decay processes such as diffusion-limited exciton-exciton annihilation. This is opposite of what one would desire for a gain medium in which the emission increases not only linearly, but super-linearly at room temperature with increasing photoexcitation. The exciton diffusion length decreases as a function of temperature, inferring that the exciton density should increase with decreasing temperature and the nonradiative decay processes become less efficient resulting in higher emission.

Therefore, we present a study of the emission from high density 1D excitons in carbon nanotubes as a function of temperature and excitation power.

The scope of this thesis is presented as follows. Chapter 2 is a brief overview of SWNT structure and electronic properties. It also highlights groundbreaking works in the optical spectroscopy of nanotubes. Chapter 3 details the unique magnetic properties of carbon nanotubes. This chapter presents the importance of the magnetic susceptibility anisotropy, including previous theory and experiments on the magnetic properties of nanotubes. The following chapter presents experimental work on the magnetic susceptibility anisotropy of metallic carbon nanotubes. Along with estimating this parameter for the first time, there is a secondary experiment which investigates the diameter dependence of the magnetic properties of metallic nanotubes. For example, at 0 T, (7,7) has a higher absorbance, while (6,6) is greater in absorbance in a parallel 35 T field, indicating that (6,6) is aligning more strongly than (7,7). This is contrary to the expectation that the larger diameter nanotube (7,7) would align proportional to the increase in diameter/Aharonov-Bohm flux and be greater than that of (6,6). Chapter 5 presents our work on the light emission from high density 1D excitons as a function of high photoexcitation and temperature. This is followed by our summary and conclusions in Chapter 6.

Chapter 2

Optical Spectroscopy of Single-Walled Carbon Nanotubes

2.1 Crystal Structure

Single-walled carbon nanotubes (SWNTs) are cylindrical sheets of graphene with diameter on the scale of ~ 1 nm and length from 100 nm to 1 mm. Experiments studying the physics of SWNTs can be treated using only one quantum channel with a typical confinement energy ~ 500 meV or larger. The strong quantum confinement drastically changes many of the physical properties in SWNTs as they go from the 2D graphene lattice to 1D nanotube. Furthermore, these properties of SWNTs change depending on the manner in which the graphene sheet is rolled.

Graphene is composed of a hexagonal lattice of sp^2 -bonded carbon atoms (Fig. 2.1) such that the primitive lattice vectors in real space are described by the following:

$$\vec{a}_1 = \frac{\sqrt{3}}{2}a\hat{x} + \frac{1}{2}a\hat{y} \quad (2.1)$$

$$\vec{a}_2 = \frac{\sqrt{3}}{2}a\hat{x} - \frac{1}{2}a\hat{y} \quad (2.2)$$

where the lattice constant a of graphene ($a = |\vec{a}_1| = |\vec{a}_2| = 2.46$ Å) and \hat{x} , \hat{y} , and \hat{z} are cartesian unit vectors. The reciprocal lattice vectors can be derived from the

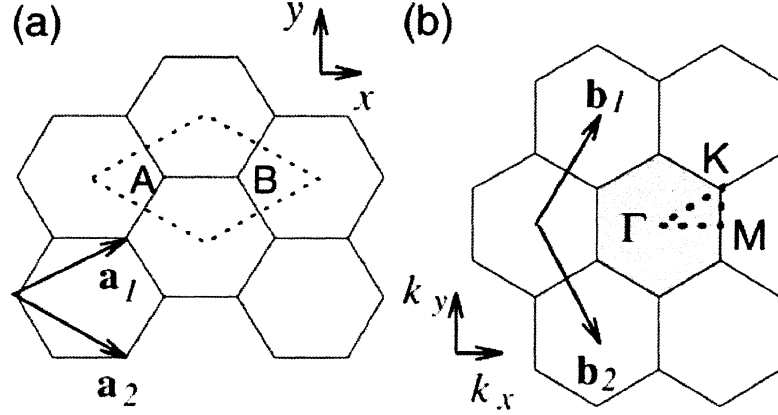


Figure 2.1 : Two-dimensional hexagonal lattice of graphene in real space (a) and reciprocal space (b). Sites labeled A and B represent carbon atoms contained within a parallelogram corresponding to the dotted primitive unit cell. In (b), the symmetry points of the bandstructure are labeled: Γ , K, and M in reference to the 1st Brillouin Zone (shaded). The lattice vectors $\mathbf{a}_{1,2}$ and $\mathbf{b}_{1,2}$ of this figure are defined in the text. Adapted from Ref. [3].

primitive lattice vectors above as follows:

$$\vec{b}_1 = 2\pi \frac{\vec{a}_2 \times \hat{z}}{\vec{a}_1 \cdot (\vec{a}_2 \times \hat{z})} = \frac{2\pi}{\sqrt{3}a} \hat{x} + \frac{2\pi}{a} \hat{y} \quad (2.3)$$

$$\vec{b}_2 = 2\pi \frac{\hat{z} \times \vec{a}_2}{\vec{a}_2 \cdot (\hat{z} \times \vec{a}_2)} = \frac{2\pi}{\sqrt{3}a} \hat{x} - \frac{2\pi}{a} \hat{y} \quad (2.4)$$

The 1st Brillouin Zone for graphene can be seen in Fig. 2.1(b) as the shaded area.

The structure of a carbon nanotube can be defined within the context of the vector that the graphene 2-D sheet (e.g., in Fig. 2.2) is folded into a cylinder, or the chiral vector:

$$|\vec{C}_h| \equiv \vec{OA} \quad (2.5)$$

$$\vec{C}_h = n\vec{a}_1 + m\vec{a}_2 \quad (2.6)$$

In Eqn. (2.5), the vector \overrightarrow{OA} represents the vector connecting two equivalent points of the 2D hexagonal lattice, O and A , in Fig. 2.2. Note that A in this case is not the same A defining the site of a carbon atom of the primitive unit cell. Equation (2.6) defines the chiral vector in terms of the basis vectors and the chiral indices, n and m . The chiral index (n, m) represents a particular type, or *chirality*, of SWNT. There are three classifications for nanotubes defined by (n, m) : chiral ($n \neq m, m \neq 0$), zigzag ($n, 0$), and armchair ($n = m$). From (n, m) , as shown in the rest of this chapter, one can determine parameters such as the diameter, number of hexagons per unit cell, and other electronic/optical properties.

The circumference, L , of the nanotube is equivalent to the length of the chiral vector, $L = |\vec{C}_h|$. Therefore, the diameter of a nanotube can be defined as:

$$d_t = \frac{|\vec{C}_h|}{\pi} = \frac{a}{\pi} \left(\sqrt{n^2 + m^2 + nm} \right) \quad (2.7)$$

The angle between the chiral vector and the basis vector \vec{a}_1 is named the chiral angle,

θ_{C_h} :

$$\theta_{C_h} = \cos^{-1} \left(\frac{\vec{a}_1 \cdot \vec{C}_h}{|\vec{a}_1| \cdot |\vec{C}_h|} \right) = \cos^{-1} \left(\frac{n + m/2}{\sqrt{n^2 + m^2 + nm}} \right) \quad (2.8)$$

For each classification, the following relationships exist for chiral angle: armchair ($\theta_{C_h} = 30^\circ$), zigzag ($\theta_{C_h} = 0^\circ$), and chiral ($0^\circ < \theta_{C_h} < 30^\circ$).

The vector \overrightarrow{OB} , parallel to the nanotube longitudinal axis and perpendicular to \vec{C}_h in Fig. 2.2, is defined as the translational vector, \vec{T} , or in terms of the primitive lattice vectors:

$$\vec{T} = t_1 \vec{a}_1 + t_2 \vec{a}_2 \quad (2.9)$$

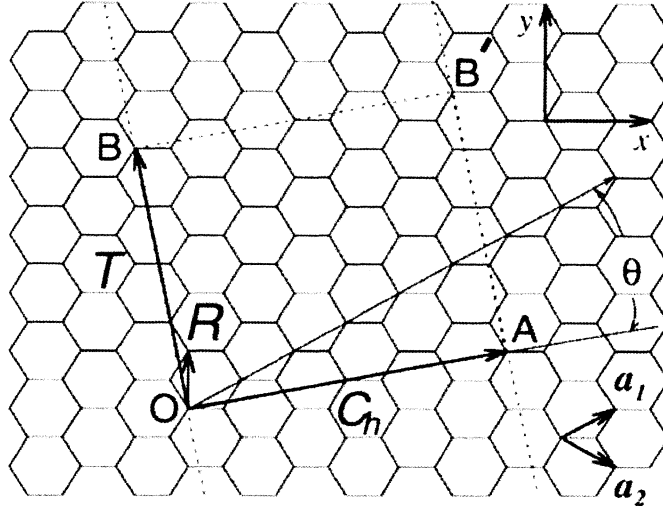


Figure 2.2 : The graphene sheet corresponding to an unrolled (4,2) nanotube in real space. The chiral vector, \vec{C}_h is shown as the vector between the points O and A . Similarly the translational vector, \vec{T} is the vector from points O to B . The chiral angle is also shown as defined in the text. Adapted from Ref. [3].

where $t_1 = \frac{2m+n}{d_R}$, $t_2 = -\frac{2m+n}{d_R}$, and $d_R = \text{gcd}(2m+n, 2n+m)$. The magnitude of \vec{T} is the length of the unit cell for a given (n, m) nanotube:

$$|\vec{T}| = \frac{\sqrt{3}L}{d_R} \quad (2.10)$$

Also, the chiral vector \vec{C}_h and the translational vector are perpendicular, i.e., $\vec{C}_h \cdot \vec{T} = 0$. The two vectors can also be used to define the rectangular area of the unit cell as $|\vec{C}_h||\vec{T}|$. Furthermore, the area of each hexagon is $|\vec{a}_1 \times \vec{a}_2|$, thus the number of hexagons per unit cell (N) is given by:

$$N = \frac{|\vec{C}_h \times \vec{T}|}{|\vec{a}_1 \times \vec{a}_2|} \quad (2.11)$$

$$N = \frac{2(n^2 + nm + m^2)}{d_R} = \frac{2L^2}{a^2 d_R}$$

Each unit cell is repeated periodically along the length of an (n, m) nanotube completing the SWNT crystal structure in real space.

2.2 Band Structure

The primitive unit cell defined by the dotted parallelogram in Fig. 2.1 contains two electron sites **A** and **B**. The electron configuration of carbon consist of four electrons in its valence shell with three being used in sp^2 covalent bonds that hold the honeycomb lattice together. The fourth electron corresponds to the remaining valence electron in the p_z orbital, and the sites **A** and **B** host two such electrons of this orbital. In this section, we will determine the band structure of these two electrons in graphene and then use the crystal structure from Sect. 2.1 to determine their band structure in single-walled carbon nanotubes (SWNTs) within the tight binding approximation.

The wavefunction due to the primitive unit cell is a linear combination of the wavefunctions of the two electron sites **A** and **B**:

$$\psi_{A,B} = c_A\phi_A + c_B\phi_B = \sum_{j=A,B} c_j\phi_j \quad (2.12)$$

where c_A and c_B are constants and ϕ_A and ϕ_B are the wavefunctions at the respective sites for the atomic p_z orbital in carbon. This is a consequence of the tight-binding approximation where the total wavefunction is a superposition of wave functions at each neighboring atomic site. These wavefunctions are traveling in a periodic lattice

structure, and thus are Bloch wavefunctions of the form:

$$\Phi_A(\vec{r}) = \frac{1}{\sqrt{N}} \sum_R^N e^{i\vec{k}\cdot\vec{R}_A} \phi(\vec{r} - \vec{R}_A) \quad (2.13)$$

$$\Phi_B(\vec{r}) = \frac{1}{\sqrt{N}} \sum_R^N e^{i\vec{k}\cdot\vec{R}_B} \phi(\vec{r} - \vec{R}_B) \quad (2.14)$$

where \vec{R} are the lattice vector of the sites A and B , \vec{k} is the wave vector, and N is the total number of unit cells. The total eigenfunction is a linear combination of the Bloch functions (Eqns. (2.13) and (2.14)):

$$\Psi_{\vec{k},j}(\vec{r}) = \sum_j c_j(\vec{k}) \Phi_j(\vec{r}) \quad (2.15)$$

where $j = A, B$ depending on the respective atom site.

Now, we must solve Schrodinger's equation to determine the energy of these orbitals with every other orbital site in the lattice:

$$H\Psi = \epsilon\Psi \quad (2.16)$$

with ϵ as the energy dispersion. For the two parameters, one for each orbital A and B , we need to get two equations to solve for the eigenvalues. Therefore from Eqns. (2.16) and (2.15), we can project Ψ onto the eigenstates ψ_A and ψ_B such that:

$$\langle\psi_A|H|\Psi\rangle = \epsilon_A(\vec{k})\langle\psi_A|\Psi\rangle \quad (2.17)$$

$$\langle\psi_B|H|\Psi\rangle = \epsilon_B(\vec{k})\langle\psi_B|\Psi\rangle \quad (2.18)$$

To approach these two equations, we begin with the left hand side of Eqn. (2.17) for the A site and substitute Eqn. (2.15) for Ψ and Eqn. (2.13) for Φ_A :

$$\langle\psi_A|H|\Psi\rangle = \sum_j c_j \langle\phi_A|H|\Phi_A\rangle = \frac{1}{\sqrt{N}} \sum_R e^{i\vec{k}\cdot\vec{R}} \sum_j c_j \langle\phi_A|H|\phi(\vec{r} - \vec{R}_A)\rangle \quad (2.19)$$

Within the tight-binding approximation, we need to calculate only the nearest neighbor interactions with $\phi_A(r)$. These interactions are 1) between $\phi_A(r)$ and $\phi_B(r)$, 2) between $\phi_A(r)$ and $\phi_B(r - \vec{a}_1)$, 3) between $\phi_A(r)$ and $\phi_B(r - \vec{a}_2)$, and 4) between $\phi_A(r)$ and itself. This leaves the following nonzero terms for Eqn. (2.19):

$$\begin{aligned}\sqrt{N}\langle\psi_A|H|\Psi\rangle &= c_A\langle\phi_A|H|\phi_A\rangle + c_B\langle\phi_A|H|\phi_B\rangle \left(1 + e^{-i\vec{k}\cdot\vec{a}_1} + e^{-i\vec{k}\cdot\vec{a}_2}\right) \\ \sqrt{N}\langle\psi_A|H|\Psi\rangle &= c_A\langle\phi_A|H|\phi_A\rangle + c_B t \left(1 + e^{-i\vec{k}\cdot\vec{a}_1} + e^{-i\vec{k}\cdot\vec{a}_2}\right)\end{aligned}\quad (2.20)$$

where $t = \langle\phi_A|H|\phi_B\rangle$ is the transfer integral between the two neighboring A and B sites. Similarly for the B site, we have for the left hand side of Eqn. (2.18):

$$\sqrt{N}\langle\psi_B|H|\Psi\rangle = c_B\langle\phi_B|H|\phi_B\rangle + c_A t \left(1 + e^{i\vec{k}\cdot\vec{a}_1} + e^{i\vec{k}\cdot\vec{a}_2}\right)\quad (2.21)$$

Following this same approach, we next need to expand the right hand side of Eqn. (2.17) for the A orbital site:

$$\epsilon\langle\psi_A|\Psi\rangle = \epsilon \sum c_j \langle\phi_A|\Phi_A\rangle = \frac{\epsilon}{\sqrt{N}} \sum_R e^{i\vec{k}\cdot R} \sum_j c_j \langle\phi_A|\phi(\vec{r} - \vec{R}_A)\rangle\quad (2.22)$$

And only taken into account the nearest neighbor interactions we have:

$$\epsilon\sqrt{N}\langle\psi_A|\Psi\rangle = \epsilon(c_A\langle\phi_A|\phi_A\rangle + c_B\langle\phi_A|\phi_B\rangle(1 + e^{-1\vec{k}\cdot\vec{a}_1} + e^{-1\vec{k}\cdot\vec{a}_2}))\quad (2.23)$$

but we also know that $\langle\phi_A|\phi_A\rangle = 1$ and $\langle\phi_A|\phi_B\rangle = 0$ therefore for the right hand side of A :

$$\epsilon\sqrt{N}\langle\psi_A|\Psi\rangle = \epsilon c_A\quad (2.24)$$

Similarly, for the right hand side of Eqn. (2.18):

$$\epsilon\sqrt{N}\langle\psi_B|\Psi\rangle = \epsilon c_B\quad (2.25)$$

By combining Eqns. (2.20) and (2.24) for site A and Eqns. (2.21) and (2.25) for B, we have the two equations and two parameters (c_A and c_B) that we set out to gain from the beginning as follows:

$$-c_A\epsilon + c_B t \left(1 + e^{-i\vec{k}\cdot\vec{a}_1} + e^{-i\vec{k}\cdot\vec{a}_2}\right) = 0 \quad (2.26)$$

$$c_A t \left(1 + e^{i\vec{k}\cdot\vec{a}_1} + e^{i\vec{k}\cdot\vec{a}_2}\right) - c_B\epsilon = 0 \quad (2.27)$$

where we set $\langle\phi_A|H|\phi_B\rangle = \langle\phi_B|H|\phi_A\rangle = 0$ because the atom sites A and B are assumed to be identical.

In matrix form we write the above equations as:

$$\begin{pmatrix} -\epsilon & t(1 + e^{-i\vec{k}\cdot\vec{a}_1} + e^{-i\vec{k}\cdot\vec{a}_2}) \\ t(1 + e^{i\vec{k}\cdot\vec{a}_1} + e^{i\vec{k}\cdot\vec{a}_2}) & -\epsilon \end{pmatrix} \begin{pmatrix} c_A \\ c_B \end{pmatrix} = 0 \quad (2.28)$$

To solve for the values of c_A and c_B , we can set the determinant of Eqn. (2.28) to zero, and solve the eigenvalue problem for allowed values of ϵ with:

$$\det \begin{pmatrix} -\epsilon & t(1 + e^{-i\vec{k}\cdot\vec{a}_1} + e^{-i\vec{k}\cdot\vec{a}_2}) \\ t(1 + e^{i\vec{k}\cdot\vec{a}_1} + e^{i\vec{k}\cdot\vec{a}_2}) & -\epsilon \end{pmatrix} = 0 \quad (2.29)$$

$$\epsilon^2 = t^2(3 + e^{i\vec{k}\cdot\vec{a}_1} + e^{i\vec{k}\cdot\vec{a}_2} + e^{-i\vec{k}\cdot\vec{a}_1} + e^{-i\vec{k}\cdot\vec{a}_2} + e^{i\vec{k}\cdot(\vec{a}_1+\vec{a}_2)} + e^{i\vec{k}\cdot(\vec{a}_1-\vec{a}_2)}) \quad (2.30)$$

Applying Euler's relations, Eqn. (2.30) becomes:

$$\epsilon^2 = t^2(3 + 2\cos(\vec{k}\cdot\vec{a}_1) + 2\cos(\vec{k}\cdot\vec{a}_2) + 2\cos(\vec{k}\cdot(\vec{a}_1 - \vec{a}_2))) \quad (2.31)$$

The wave vector, \vec{k} can be defined as $\vec{k} \equiv (k_x + ik_y)$ where k_x and k_y are reciprocal lattice wave numbers. Using this definition, we are now set to get the band structure

of graphene in 2D:

$$\epsilon_{2D} = \pm t \sqrt{3 + \cos(a/2(\sqrt{3}k_x + k_y)) + \cos(a/2(\sqrt{3}k_x - k_y)) + 2 \cos(ak_y)} \quad (2.32)$$

where the + sign is for the conduction π^* band and the - sign corresponds to the valence π band.

We have defined the crystal structure of a carbon nanotube in Sect. 2.1, therefore we can determine the band structure of SWNTs using this information and the band structure of graphene (Eqn. (2.32)). We begin with the reciprocal lattice vectors, \vec{K}_1 and \vec{K}_2 in \mathbf{k} -space that are related to the real space vectors \vec{C}_h and \vec{T} by the relation [4]:

$$\vec{R} \cdot \vec{K}_j = 2\pi \delta_{ij} \quad (2.33)$$

where \vec{R} is a vector in real space. As a consequence of the Kronecker delta (δ_{ij}) in Eqn. (2.33), the following statements are true: $\vec{C}_h \cdot \vec{K}_1 = 2\pi$, $\vec{T} \cdot \vec{K}_1 = 0$, $\vec{C}_h \cdot \vec{K}_2 = 0$, and $\vec{T} \cdot \vec{K}_2 = 2\pi$. Therefore, the reciprocal vectors are defined as:

$$\vec{K}_1 = \frac{1}{N} \left(-t_2 \vec{b}_1 + t_1 \vec{b}_2 \right) \quad (2.34)$$

$$\vec{K}_2 = \frac{1}{N} \left(m \vec{b}_1 - n \vec{b}_2 \right) \quad (2.35)$$

\vec{K}_1 gives discrete values of k in the circumferential direction of \vec{C}_h and \vec{K}_2 represents the reciprocal lattice vector along the nanotube longitudinal axis.

The act of folding the graphene sheet into a cylinder imposes the following boundary conditions:

$$\psi_{n\vec{k}}(\vec{r} + \vec{C}_h) = e^{i\vec{k} \cdot \vec{C}_h} \psi_{n\vec{k}}(\vec{r}) \quad (2.36)$$

Therefore, you have the following quantization of the wavevector \vec{K}_1 :

$$\vec{K}_1 \cdot \vec{C}_h = 2\pi j$$

where j is an integer. After relating these quantized wave vectors into Equation 2.32, you obtain the energy dispersion relation in 1D:

$$\epsilon_\mu(k) = \epsilon_{2D} \left(k \frac{\vec{K}_2}{|\vec{K}_2|} + \mu \vec{K}_1 \right) \quad (2.37)$$

where μ is the quantum number such that $\mu = (1, 2 \dots N)$ and $-\frac{\pi}{a} < k < \frac{\pi}{a}$.

There are three main symmetry points in the 1st Brillouin Zone for graphene, Γ , M, and K corresponding to the highest center point to the lowest band edge. The vector $\mu \vec{K}_1$ can be viewed as a cutting line on the 1st Brillouin Zone. If this vector passes through the K point of the 1st Brillouin Zone, the bandgap = 0 and the nanotube is metallic. When $\mu \vec{K}_1$ does not pass through the K point, then the nanotube is a semiconductor. As a simple rule, a nanotube with index (n, m) is metallic if $(n - m) \bmod 3 = 0$. According to this rule, armchair nanotubes are always metallic; and there exist a subset of chiral nanotubes that are metallic but have a very small band gap. If (n, m) for other types of tubes do not satisfy this rule then the nanotube is semiconducting. For semiconductor nanotubes and non-armchair metallics, the band gap is a function of the diameter [3]:

$$E_g(\text{semiconductor}) \sim 1/d_t \quad (2.38)$$

$$E_g(\text{non - armchair metallic}) \sim 1/d_t^2 \quad (2.39)$$

2.3 Nanotube Optics

2.3.1 Optical Selection Rules for Carbon Nanotubes

Single-walled carbon nanotubes are often studied for their applications as nanoscale electronic devices, but another driving force has been their optical properties. These optical properties stem from the structure-dependent attributes such as length, diameter, and chirality, however before we present them in this context, we set forth to present selection rules for the manner in which nanotubes absorb and emit light.

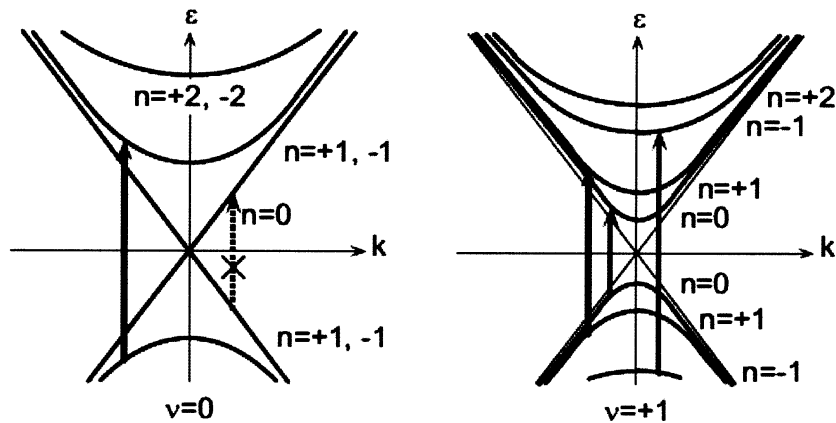


Figure 2.3 : The optical selection rules of (left) metallic ($\nu = 0$) and semiconducting (right) ($\nu = \pm 1$) nanotubes for light incident parallel to the nanotube axis. The indices n correspond to the optical transitions from bands with equal momentum angular momentum.) (Ref. [5])

In general, the selection rules are a consequence of angular momentum and parity of the mirror symmetry planes (Fig. 2.4) for each transition with respect to the polarization of the light. Therefore, you have two cases depending on if the light is linearly polarized or if the light is perpendicularly polarized. With respect to the mir-

ror symmetry planes, optical transitions are only allowed for even states with respect to σ_v for both polarizations. For light with parallel polarization with respect to the nanotube axis, optical transitions are allowed between valence and conduction bands only with the same band index, n , where n is an integer (Fig. 2.3) [5]. Transitions with the same band index integer ($\Delta n = 0$), also have the same change in angular momentum ($\Delta m = 0$). And, transitions are only allowed for states with opposite parity/sign with respect to σ_h for parallel polarization.

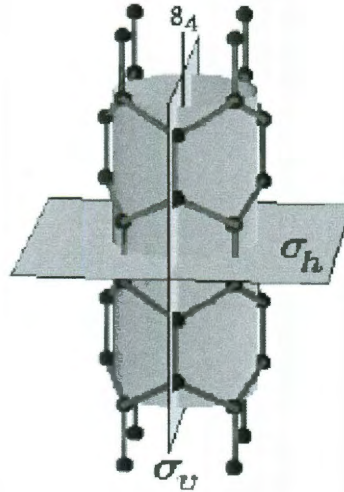


Figure 2.4 : Mirror symmetry planes for the (4,0) zigzag nanotube. The horizontal mirror symmetry plane (σ_h) is transversed by the vertical mirror symmetry plane, σ_v . The nanotube axis or z-axis in this figure is labeled as the 8_4 screw axis. (Ref. [6])

Now for the second case where light is polarized perpendicular to the nanotube axis, optical transitions are allowed for bands with changes in angular momentum of ± 1 ($\Delta m = \pm 1$). With respect to parity of the σ_h plane, optical transitions for the perpendicular polarization are only allowed for the same sign. By these selec-

tion rules, transitions for the perpendicular polarization are allowed, but due to the depolarization effect [7], they can be suppressed. The complex treatment of perpendicular transitions can be reviewed in Ref. [5,8] but for the purposes of this work the perpendicular transitions $E_{i\ i+1}$, where i is an integer, are not investigated.

For the SWNTs studied in the current work, with light polarized parallel to the nanotube axis, the energies at which these transition occur are labeled E_{ii} . E_{11} of metallic nanotubes and E_{22} are in the visible with increasing numbers corresponding to higher energy transitions. Light emission for semiconductor nanotubes in this diameter range (~ 1 nm) usually occurs in the near-infrared and will be highlighted in the following subsection.

2.3.2 Structure Assigned Photoluminescence of Carbon Nanotubes

A key component to the optical spectroscopy of carbon nanotubes was the use of surfactants and ultracentrifugation to allow for individual nanotubes to exhibit an optical response. O'Connell et al. showed that absorption spectroscopy could reveal the degree of individualization for both metallic and semiconducting carbon nanotubes [9]. Nanotubes that are not individualized are bundled through the very strong van der Waals forces. After the process described in Ref. [9], nanotubes are wrapped in surfactants that allowed for many studies of the optical properties of carbon nanotubes through optical spectroscopy.

The field of nanotube optics was catapulted by the discovery that semiconduct-

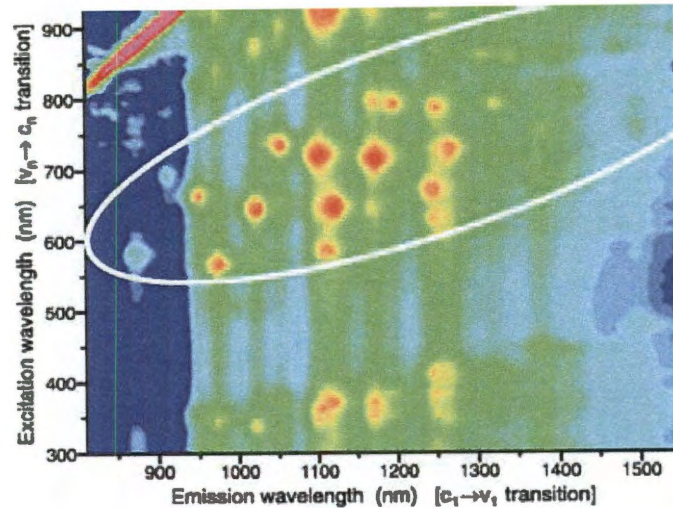


Figure 2.5 : Photoluminescence excitation spectroscopy of SWNTs in solution. Each resonance corresponds to a different (n, m) depending on the structure and band gap of the carbon nanotube (Ref. [10]).

ing nanotubes fluoresce in the near-infrared depending on the (n, m) dependence or crystal structure (Sect. 2.1). Bachilo et al. performed photoluminescence excitation spectroscopy (PLE) on individualized carbon nanotubes solubilized in water [10]. A given chirality will have an excitation and emission wavelength which will correspond to resonances in a photoluminescence excitation (PLE) map, as shown in Fig. 2.5. Light absorption at the E_{22} energy results in light emission at the E_{11} energy. Therefore, the PLE map exhibits resonances in two dimensions.

Table 2.1 gives the emission and excitation wavelengths and photon energies for several chiralities presented in the context of this thesis. Researchers use optical spectroscopy to characterize bulk samples of nanotubes to understand the different chiralities which make up their sample. However, depending on the surfactant or if

Table 2.1 : Table of wavelengths and energies corresponding to E_{22} and E_{11} of (n, m) semiconductor nanotubes studied in this thesis. The values are those presented in Ref. [10].

(n, m)	E_{22} (nm)	E_{11} (nm)	E_{22} (eV)	E_{11} (eV)
(6,4)	581	873	2.13	1.42
(6,5)	567	975	2.19	1.27
(8,3)	663	952	1.87	1.30
(7,5)	644	1023	1.93	1.21
(9,4)	720	1101	1.72	1.13
(10,2)	734	1052	1.69	1.18
(7,6)	647	1122	1.92	1.11

the nanotubes are dispersed in film or in solution, the E_{11} and E_{22} energies can be slightly different than those found in the figure or in the table.

2.3.3 Excitons in Carbon Nanotubes

Excitons are bound states that form as a result of the Coulomb interaction of electrons and the vacancies (holes) that are left when electrons transition between the valence and conduction bands of solids. Coulomb interactions are heavily influenced by a reduction in the dimensionality of a system. For instance in 3D (bulk semiconductors), the appearance of excitons in optical spectra occurs at low temperatures but a reduction to 2D (quantum wells) results in excitons being observed as high as

room temperature [11]. Further confinement, reduces dimensionality to 1D excitons, where the ideal case is represented by the 1D hydrogen atom with infinitesimal diameter [12]. Characteristics of 1D excitons are long radiative lifetimes (~ 100 s of ps for quantum wires) [13], infinite binding energy [12], and a Sommerfeld factor less than unity [14, 15].

The uniqueness of low dimensionality in the context of excitons is easily illustrated through the presentation of the Sommerfeld factor, or the ratio of the absorption intensities of the continuum to the free exciton above the band edge. In 3D, this ratio increases as a function of energy with a $1/\sqrt{E}$, where E is a function of the photon energy, binding energy and band gap. When reducing down to 2D, the Sommerfeld factor is constant. In 1D, the strong Coulomb interaction diminishes the absorption intensity and the majority of the oscillator strength is contained by the lowest exciton state below the band gap. This results in a Sommerfeld factor less than 1 [14, 15].

Reduction from 3D bulk semiconductors to 2D systems like quantum wells also results in a binding energy four times larger. For 1D excitons, further confinement causes an even large overlap between the electrons and holes. In chain polymers of diameter ~ 1 nm, the binding energy is on the order of 1 eV [16], and in 10 nm semiconductor wires it is about two orders of magnitude lower [17]. Binding energies for SWNTs are predicted and experimentally measured to be on the order of two magnitudes greater than those found in empirical bulk semiconductors, or 300 - 500 meV for [18–22].

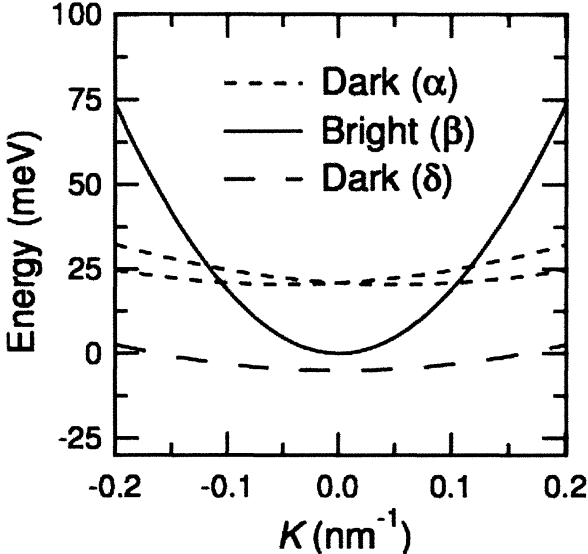


Figure 2.6 : Energy dispersion of singlet exciton states for the (9,4) nanotube. The $1u$ bright band (solid) is a few meV above the lowest $1g$ dark state (large dashes). The higher energy states (small dashes) are dark due to finite angular momentum. Adapted from Ref. [23]).

Theoretically, the strong Coulomb interactions of electrons and holes causes SWNTs to have their own exciton energy levels and optical selection rules for excitons [24–26]. It is predicted that an exciton is optically active if it has the same symmetry; i.e. zero angular momentum and odd parity. As seen for the (9,4) nanotube in Fig. 2.6, there are predicted to be four singlet exciton states. Of the four singlet exciton states, the only optically-active singlet exciton state is termed the $1u$ state [24–26]. The two highest energy states of the other three are predicted to be dark exciton states due to the finite angular momentum. The lowest state, $1g$, is dark due to even parity. The effect of magnetic field on the predicted excitonic picture is presented in Sect. 3.2 of this work.

Experimentally, the exciton nature of nanotube optics was difficult to prove in one-photon photoluminescence excitation (PLE) experiments, like in Ref. [10]. Two groups independently utilized the method of two-photon PLE as a way of proving the excitonic nature of optical spectra at room temperature in SWNTs [21, 22]. By exciting at the energy of the $2g$ state, the researchers were exciting at an energy where absorption of two-photons would be above half of the first optical transition, $E_{exc} > E_{11}/2$. If there was no influence of excitons on the optical spectra, then absorption of the two photons would occur at exactly $E_{11}/2$ ($E_{exc} = E_{11}/2$). As seen in Fig. 2.7, it occurred at energies above $E_{11}/2$. The difference in energy between the absorption at E_{2g} and the emission at E_{1u} from the two-photon PLE plots brought about estimations of the binding energy for SWNTs of diameters ~ 1 nm to be in the range of 300-500 meV [21, 22]. This work stimulated a vast field in exciton physics of SWNTs, leading to reports on exciton size and mobility [27], multiple exciton generation [28], and exciton density and annihilation [29–37].

The radiative lifetime in nanotubes has also been a major focus in the study of excitons in carbon nanotubes both theoretically [19, 20, 38, 39] and experimentally [23, 34, 40–44]. Temperature dependence of photoluminescence (PL) was used to study the radiative lifetime with it being predicted to be influenced by the inclusion of dark states [38]. As you decrease the temperature from room temperature, photoluminescence decreases until it reaches a maximum. After this maximum, it decreases again; this is due to the thermalization of excitons from the bright state

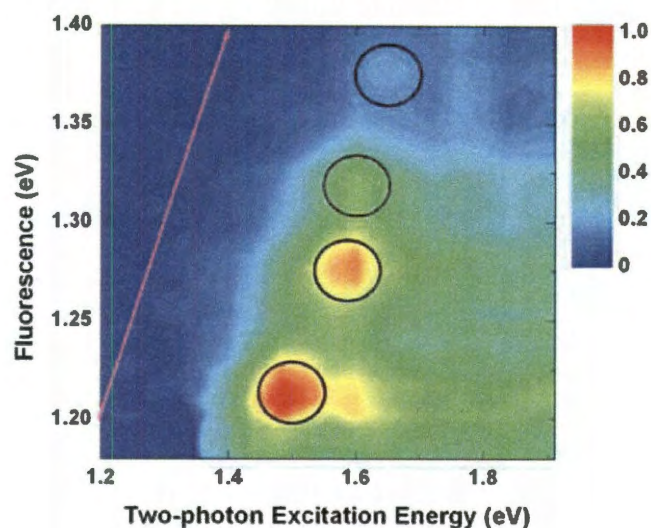


Figure 2.7 : Two photon photoluminescence excitation spectroscopy of SWNTs. The red line corresponds to the energy at which the laser excitation would be equal to half of the optical transition. Each resonance falls above this energy corresponding to a difference and experimental evidence of excitons at room temperature in SWNTs.(Ref. [22]).

to the dark state causing less PL to be emitted. Depending on chirality and local environment, there is a different peak temperature at which the PL is the highest. For the diameter range ~ 1 nm, the peak temperature is from 50-100 K [23, 42–44]. Different temperature dependent plots of PL intensity are shown for several chiralities in Fig. 2.8.

A particularly interesting aspect for applications in nanotube optics is the reported low quantum efficiencies of carbon nanotubes. This is probably the main obstacle standing in the way of widespread nanotube optoelectronic devices. The quantum efficiency is directly related to radiative and nonradiative lifetime of excitons in carbon

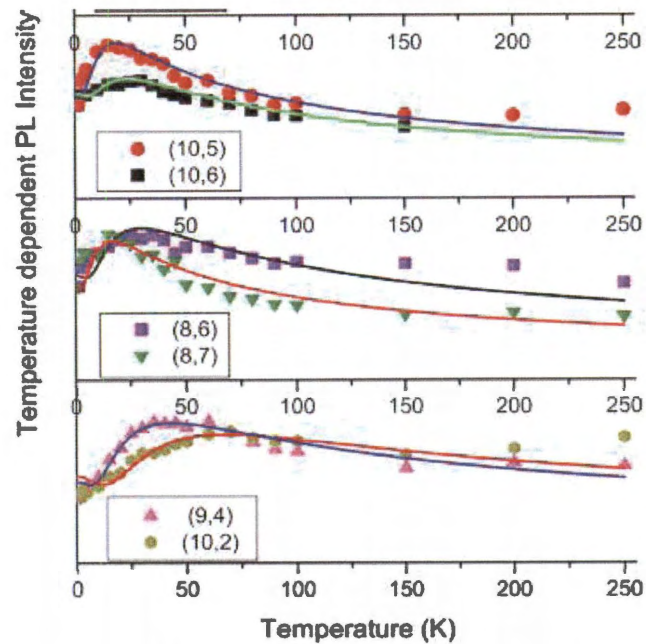


Figure 2.8 : Photoluminescence intensity as a function of Temperature for different (n, m) SWNTs. For the nanotubes shown, there is a temperature maximum dependent on chirality and then a drop in intensity at lower temperature. (Ref. [44]).

nanotubes. It is uncertain whether these low efficiencies are a product on optically inactive exciton states or structural defects. Current values of the quantum efficiency of single carbon nanotubes at room temperature vary from $\sim 10^{-2} - 10^{-6}$ [45, 46].

Chapter 3

Magnetic Properties of Carbon Nanotubes

3.1 Diamagnetism of Graphite

The magnetic susceptibility, χ , is defined as [4]:

$$\chi \equiv \frac{M}{H} \quad (3.1)$$

where M is the magnetization of the material and H is the applied magnetic field. A material is paramagnetic when $\chi > 0$ or the magnetic dipole moment of the system orients toward the direction of the applied magnetic field [4]. Conversely, when $\chi < 0$, the magnetic dipole moment repels away from the applied magnetic field, and is diamagnetic [4]. The third class of magnetism is ferromagnetism, in which no applied magnetic field is necessary for magnetization to be present in the material. Ferromagnetic materials have characteristically high values for magnetic permeability, μ .

The well-known diamagnetic nature of graphite was first reported by Honda and Owen, where they measured magnetic susceptibility for a total of 58 elements over a vast range of temperatures (room temperature to 1000 degrees [47] and low temperatures, down to liquid air [48]). Owen also discovered anisotropy in the magnetic response of graphite citing a 6 fold increase in magnetization perpendicular to the

hexagonal plane versus that parallel to the hexagonal plane. The magnetic susceptibility of graphite at room temperature is reported to be more than ten times larger than that of diamond ($\chi(\text{diamond}) = -5.5 \times 10^{-6}$ emu/mol and $\chi(\text{graphite}) = -88 \times 10^{-6}$ emu/mol) [2].

As a comparison, the only other materials with larger diamagnetism than graphite are superconductors which are perfectly diamagnetic, $\chi(\text{superconductor}) = -1$ emu/mol [4]. This unusually large diamagnetism, according to C. V. Raman in his letter to *Nature*, is a result of the crystal structure and electrical conductivity [1]. Further understanding of the magnetic properties of graphite yields the analogy of a ring current system. In this picture, each hexagon (benzene ring) of each plane of graphene exhibits an induced closed-current loop. The susceptibility is determined by the area of the loop and the total current, and described by the following as [2]:

$$\chi = -\frac{Ne^2}{4mc^2}\rho^2$$

where N is Avogadro's number, c is the speed of light, e is the electron charge, m is the mass of the electron, and the area of the loop is $\pi\rho^2$. This susceptibility yields a magnetic moment in the opposite direction of the magnetic field, hence diamagnetism in graphite.

Graphene is the starting material for many carbon allotropes including graphite, graphene oxide [50], graphene nanoribbons [51], fullerenes [52], and single-walled carbon nanotubes (SWNTS) [53, 54]. Although different allotropes have their own unique physical properties depending on structure/chirality, size, and dimensionality,

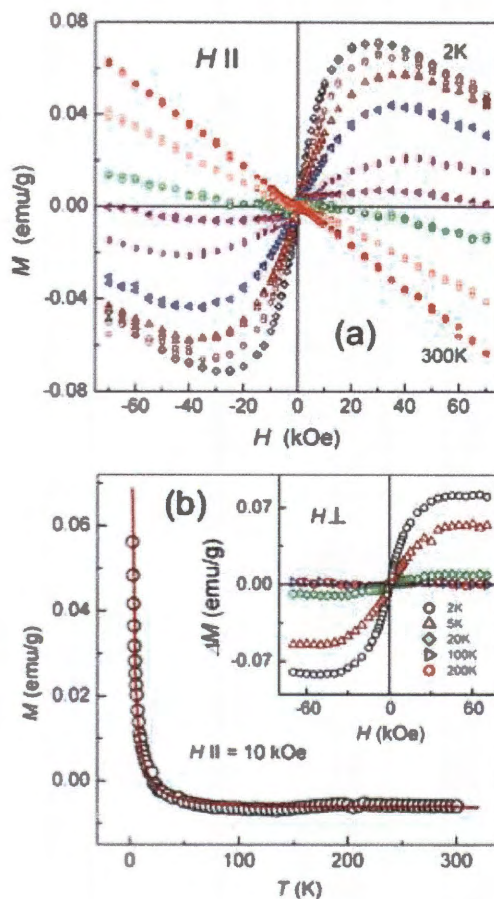


Figure 3.1 : Temperature dependence of magnetization in graphene laminates with a) parallel magnetic field and b) perpendicular magnetic field (inset). The Curie law behavior with temperature is exhibited in (b) (Ref. [49])

the magnetic properties of most graphene derivatives share the diamagnetic nature of their parent material. The magnetic susceptibility of graphene laminates was recently shown to be diamagnetic at room temperature with a value of $\chi_{\perp} \approx -1.5 \times 10^{-5}$ emu/g (about half of that of highly ordered pyrolytic graphite) [49]. The authors also found that at temperatures below 20 K, their sample exhibited unusual paramagnetism in both parallel and perpendicular directions [49]. They explained that the paramag-

netism was not chemically induced, but attributed their findings to structural effects (edge/zigzag) and size effects (not seeing this in large laminates above 200 nm). The results of their SQUID magnetometry measurements can be seen in Fig. 3.1.

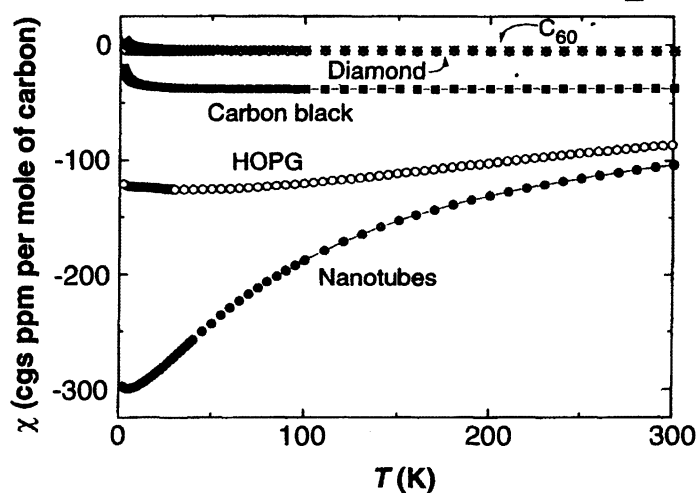


Figure 3.2 : Magnetic susceptibilities as a function of temperature of various carbon derivatives where CGS ppm/mol = $\text{emu} \times 10^{-6}/\text{mol}$. Adapted from [2, 55].

We can briefly introduce the “original” buckyball C_{60} and its close relative C_{70} as another example of how structure and size can play a part in determining differences in magnetic susceptibility. The magnetic susceptibility of C_{60} is given to be $\sim -4 \times 10^{-6}$ emu/mol [55], on the same order as $\chi(\text{diamond})$. However, $\chi(C_{60})$ is more than two times less than $\chi(C_{70})$ even though they are in the same family

of allotropes [56]. Furthermore, C_{60} contains a benzene ring structure which many have attributed to the large diamagnetism seen at room temperature for graphite [2]. At room temperature as seen in Fig. 3.2, nanotubes, regardless of whether they are metallic or semiconductors, were predicted to behave like graphite with the first estimation of diamagnetism for bundled nanotubes even greater than that of graphite. However, structure/chirality and magnetic field play an important role in determining the magnetic susceptibility anisotropy:

$$\Delta\chi = |\chi_{\parallel} - \chi_{\perp}| \quad (3.2)$$

in individual carbon nanotubes. The following sections will detail the physics behind the magnetic susceptibility anisotropy and its role in determining the magnetic properties of carbon nanotubes.

3.2 Aharonov-Bohm Effect in Carbon Nanotubes

The anisotropy of the magnetic susceptibility in carbon nanotubes can be explained in the framework of the Aharonov-Bohm effect [57, 58]. First presented in the context of a double slit interference experiment, the Aharonov-Bohm effect is a phase induced on the periodic boundary conditions of a particle in the presence of an external electromagnetic field. The particle itself is only effected by the additional phase and not the force of the external field. The Aharonov-Bohm effect has been studied in many systems such as quantum dots, metallic rings, and toroidal magnets [].

Ajiki and Ando reported calculations showing that the band structure for SWNTs changes as a function of the amount of Aharonov-Bohm flux through the center of the nanotube [59]. For the case when $B \neq 0$ or finite magnetic field, this boundary condition changes to:

$$\psi_{n\vec{k}}(\vec{r} + |C_h|) = \psi_{n\vec{k}}(\vec{r})e^{2\pi i\phi/\phi_0}$$

Note that there is an additional term, the Aharonov-Bohm Phase, which is a function of the magnetic flux ϕ through the nanotube from the external field and magnetic flux quantum, $\phi_0 = ch/e$. As a result, the discrete wave vector k with B must satisfy the following:

$$\vec{k} \cdot \vec{C}_h = 2\pi \left(j + \frac{\phi}{\phi_0} \right)$$

where j is an integer. A change in the wave vector results in a change in the dispersion relation for the electronic states near the K point and ultimately the band gap [60]:

$$E_{g,metallic} = \frac{6\pi a_{cc}\gamma_0}{|C_h|} \left(\frac{\phi}{\phi_0} \right) \quad (3.3)$$

$$E_{g,semi} = \frac{2\pi a_{cc}\gamma_0}{|C_h|} \left(1 - \frac{3\phi}{\phi_0} \right) \quad (3.4)$$

Here, a_{cc} is the distance between carbon atoms, $a_{cc} = 0.142$ nm, and γ_0 is the band parameter (~ 2.7 eV). The above equations are limited to the limit of $B < \phi_0/2$, which is considerably higher than attainable for most experimental values for B . For nanotubes presented experimentally in this work, $d \sim 1$ nm, $\phi_0/2 \sim 2 \times 10^3$ T. Note that for metallic nanotubes ($\nu = 0$), as in Fig. 3.3, the band gap increases until it reaches a maximum at $\phi_0/2 = 1/2$). After this maximum, the band gap

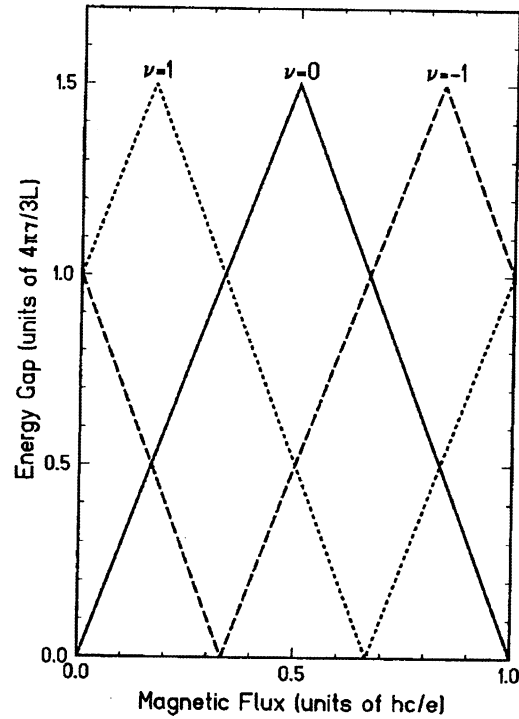


Figure 3.3 : Bandgap as a function of magnetic flux through the nanotube. Note that it oscillates with a period of ϕ (as defined in Section 3.2 for both semiconducting ($\nu = \pm 1$) and metallic ($\nu = 0$) nanotubes. (Ref. [8])

decreases with increasing ϕ until it reaches 0. Above this field, the band gap will begin to increase again oscillating with a period of ϕ . Furthermore, metallic and semiconducting nanotubes respond to Aharonov-Bohm flux in opposite ways; i.e. the band gap shrinks with magnetic field for semiconducting nanotubes.

3.2.1 Optical Signatures of the Aharonov-Bohm Effect in Carbon Nanotubes

Ajiki and Ando also predicted that through polarized optical absorption spectroscopy their theory could be experimentally verified due to the optical selection rules of SWNTs. This is due to the fact that light polarized parallel to the tube axis is absorbed whereas light polarized perpendicular is not absorbed [8]. Zaric et al. successfully showed that this was the case for HiPco SWNTs up to 45 T [61]. At this magnetic field provided by the largest DC field in the world [62], nanotubes with $d \sim 1$ nm are expected to have $\phi/\phi_0 = 8.55 \times 10^{-3}$ [61]. Furthermore, for semiconducting nanotubes where the K-K' degeneracy is lifted, the optical transitions in the E_{11} are predicted to show splitting in the absorption peaks on the order of $\sim 30 - 50$ meV. At fields > 30 T, the authors observed this splitting resulting in the first optical evidence of the Aharonov-Bohm effect in SWNTs (Fig. 3.4).

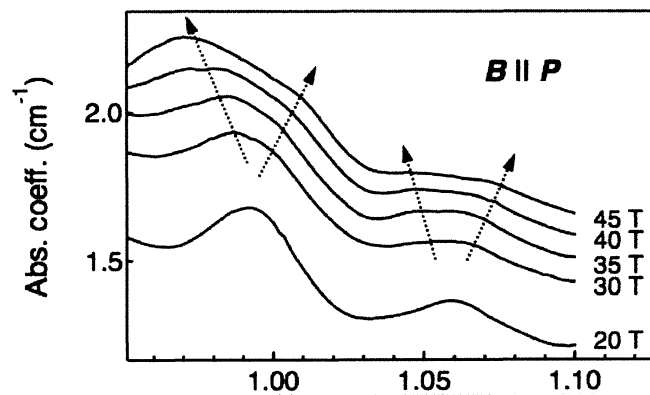


Figure 3.4 : Magneto-absorption of SWNTs above 20 T using the Hybrid magnet at NHMFL. At fields above 30 T, there is splitting that occurs in each absorption peak (Ref. [61]))

Along with magneto-absorption, Zaric et al. also presented magneto-PL data up to 45 T. For each spectrum with increasing B , there was a notable redshift in peak position. From both absorption and PL data, they were able to extract similar numbers to the theoretical values, but the estimated values of splitting from experimental data were consistently lower for the E_{11} semiconductor transitions and non-existent for E_{22} semiconductor and metallic nanotubes. This was attributed to the broad linewidths of E_{22} semiconductor and E_{11} metallic optical transitions in the visible regime making it difficult to resolve splitting.

In a complementary study, Zaric et al. performed magneto-optical spectroscopy up to 74 T utilizing the pulsed magnet facilities at Toulouse, France and Los Alamos National Lab/NHMFL [63]. At fields above 55 T, the authors found two absorption peaks arise from the splitting of each singular peak at zero field. Representative magneto-absorption results above 35 T can be seen in Fig. 3.5. Unlike the results presented in Fig. 3.4, the peaks resulting from splitting at the highest field are now of equal strength in Fig. 3.5. Similar to that experiment, they also compared their absorption with PL and observed marked redshifting of peaks above 16 T.

For the data from Fig. 3.5, Zaric et al. introduced their results in the context of broken time-reversal symmetry in excitons (Fig. 3.6). When $B = 0$, in the single particle picture, it is predicted that intervalley Coulomb mixing causes the lowest energy s -like exciton state to split into 16 levels, one being optically-active, or bright, and the other fifteen optically-inactive, or dark excitons [26]. The two, lowest-energy

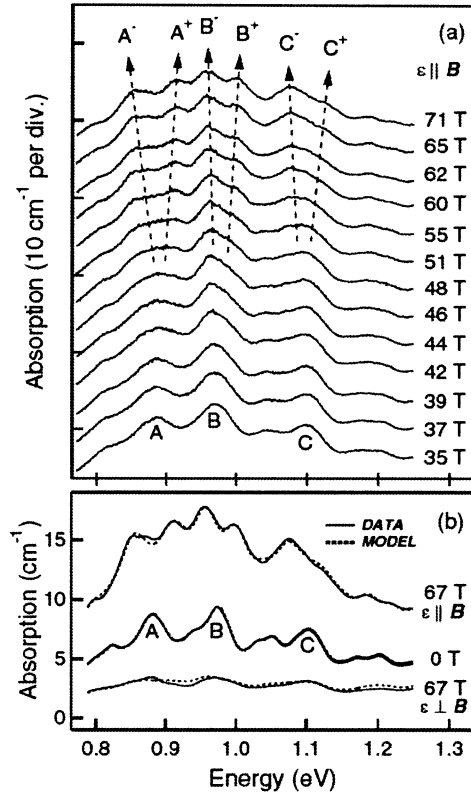


Figure 3.5 : Near-infrared magneto-absorption in semiconducting SWNTs at high magnetic fields for (a) polarization parallel to B up to 74 T (b) B parallel and perpendicular up to 67 T. In each case, splitting occurs at fields above 55 T. Adapted from [63].

spin-singlet exciton states are very close in energy ($\sim 1-9$ meV), separated by a (n,m) -dependent gap Δ_x , the dark-bright splitting. As the magnetic field is applied, the separation increases as evidenced by the redshifts of PL peaks. At the same time, the dark state acquires a finite oscillator strength in a finite magnetic field, while that of the bright state decreases with increasing magnetic field. This can be understood as a result of K-K' degeneracy lifting, since the applied magnetic field breaks the time-reversal symmetry. At the high field limit, the separation of these two states is

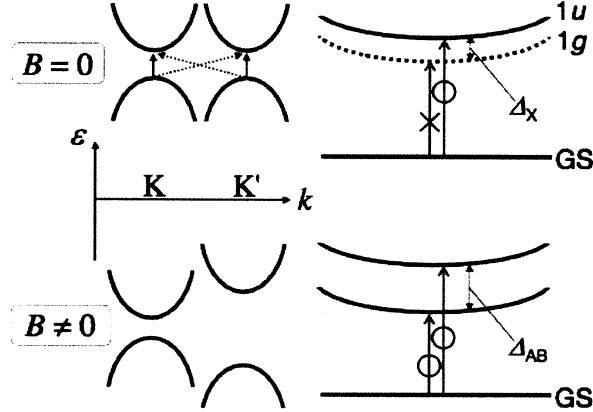


Figure 3.6 : Schematic of Magnetic Brightening. For K-K' degeneracy and intervalley mixing results in dark state ($1g$) to be below the only optically-active ($1u$) state. After a finite B , then the distance between the two states increase causing the $1g$ state to become bright. Adapted from [63].

approximately equal to the Aharonov-Bohm splitting, Δ_{AB} . The absorption and PL data was used to extract values of Δ_{AB} using the following:

$$\Delta_{AB} = \nu B \quad (3.5)$$

For the nanotubes studied by Zaric et al., predicted values for $\nu \sim 1$ meV/T for Eqn. (3.5) and this was confirmed with a value of 0.9 meV/T [63].

3.2.2 Magnetic Brightening of Excitons in Carbon Nanotubes

Although the work by Zaric et al. [61, 63] clearly showed that there were two bright exciton states at high magnetic fields, it was not confirmed that the lowest dark exciton state existed at zero field. The current section highlights studies that utilized magneto-photoluminescence spectroscopy to probe the phenomenon of “magnetic

brightening” of dark excitons in SWNTs (macroscopically [43, 44, 64] and microscopically on single nanotubes [65]).

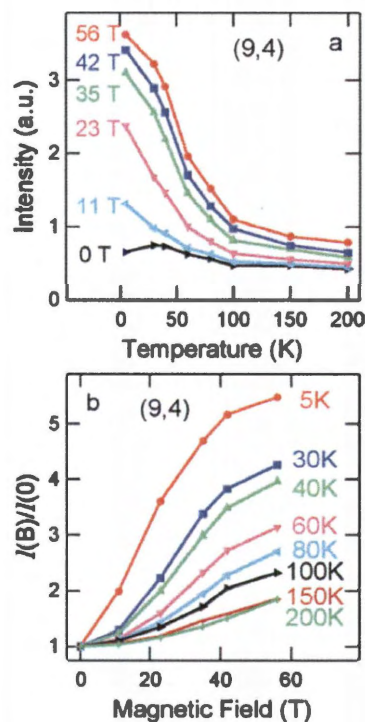


Figure 3.7 : (a) Magneto-PL of the (9,4) SWNT up to 56T as a function of temperature (b) Magnetic Brightening as a function of magnetic field for several temperatures [43].

Magnetic brightening, or the increase in PL intensity as a function of magnetic flux through each SWNT, was reported independently by the Kono group at Rice University and the Nicholas group at Oxford University. Both groups also reported that this increase in PL from the magnetic field was increased with decreasing temperature (Fig. 3.7). For Δ_x , Mortimer and Nicholas found values from 1-5 meV and a nearly $1/d$ dependence, while Shaver et al. found values from 5-8 meV and an uncer-

tain diameter dependence. Shaver et al. also found that the alignment of the carbon nanotubes with magnetic field could drastically influence the amount of magnetic brightening as result of more flux threading the nanotube axis [64].

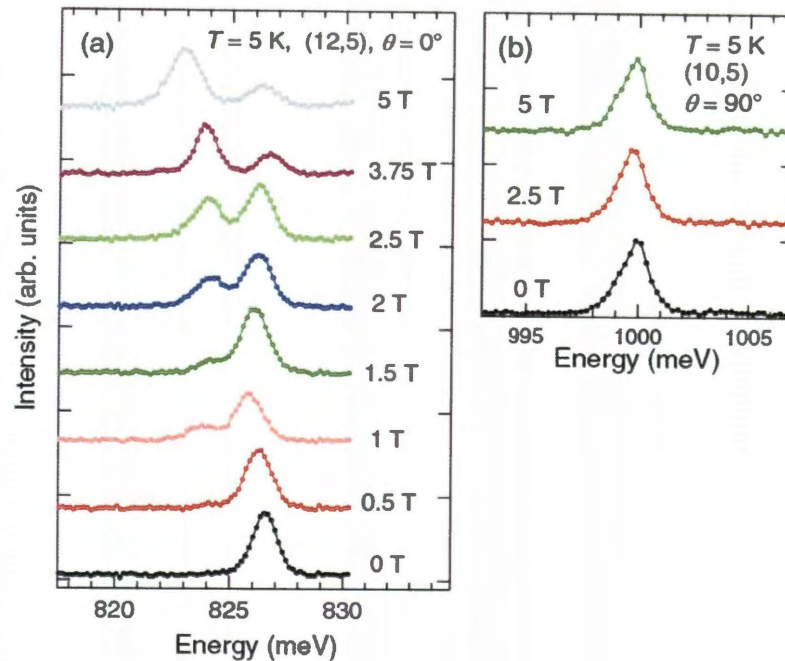


Figure 3.8 : Single nanotube μ -PL at 5 K of the (a) (12,5) nanotube in the Voigt configuration (b) and (10,5) nanotube in the Faraday configuration. Note that only in the Voigt case is there the commencement of a low energy peak and that peak increases with increasing magnetic field. Adapted from [65].

The observation of magnetic brightening by these groups confirmed the existence of a dark state ($1g$) below the first bright state ($1u$), but for an unambiguous determination of Δ_x , measurements needed to be made on single individualized nanotubes at low temperature and high magnetic field. Srivastava et al. studied hundreds of single carbon nanotubes at low T and up to 5 T [65]. They found that as the mag-

netic field increased, there was an additional peak that arose in the PL spectra a few meV below the main PL peak. At a field above 3 T, the oscillator strength began to increase for the lower-energy peak in comparison to the original peak as seen in Fig. 3.8(a). This is thought to be direct observation of the brightening of the dark state excitons. Srivastava et al. also confirmed that the Aharonov-Bohm effect was, in fact, the mechanism behind the magnetic brightening of dark excitons because nanotubes only exhibited this behavior when the nanotube whose axis was parallel to the magnetic field (Fig. 3.8(b)).

3.3 Novel Magnetic Properties of Single-Walled Carbon Nanotubes

Ajiki and Ando extended their theory of the Aharonov-Bohm effect (Section 3.2) to the magnetic properties of single walled carbon nanotubes (SWNTs) [59, 66]. The magnetic properties of SWNTs change with the direction of the magnetic field with respect to the tube axis, yielding a magnetic anisotropy given by $\Delta\chi = |\chi_{\parallel} - \chi_{\perp}|$, where χ_{\parallel} is the magnetic susceptibility in the parallel direction and χ_{\perp} is the magnetic susceptibility in the perpendicular direction. Metallic nanotubes are paramagnetic along the tube axis ($\chi_{\parallel} > 0$) and diamagnetic in the perpendicular direction ($\chi_{\perp} < 0$), whereas semiconducting tubes are diamagnetic in all directions ($\chi_{\parallel} < 0$ and $\chi_{\perp} < 0$). They calculated $\Delta\chi \sim 1-2 \times 10^{-5}$ emu/mol for semiconducting SWNTs and $\Delta\chi \sim 5-10 \times 10^{-5}$ emu/mol for metallic nanotubes as seen in Fig. 3.9. Furthermore, they

found that $\Delta\chi$ scales linearly with diameter and $\Delta\chi > 0$ holds for all types of SWNTs.

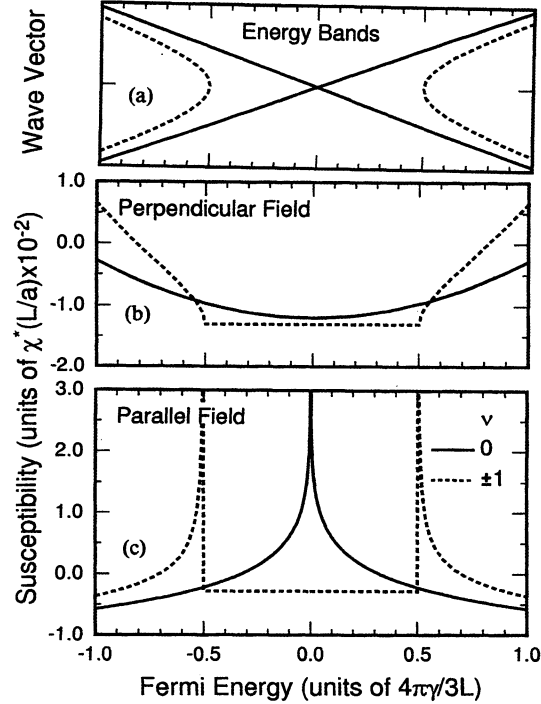


Figure 3.9 : (a) Band dispersions for metallic and semiconducting nanotubes: Wavevector as a function of Fermi energy, E_f . (b) χ_{\perp} for semiconductor ($\nu = \pm 1$) and metallic nanotubes ($\nu = 0$) as a function of E_f . (c) χ_{\parallel} for semiconductor and metallic nanotubes as a function of E_f (Ref. [66]).

Similarly, Lu investigated the magnetic properties of SWNTs using a London approximation in the same manner as theorists at that time used in studying benzene rings in C_{60} [2]. He also predicted that metallic and semiconductor nanotubes have very different magnetic susceptibility anisotropies with values on the same order as Ajiki and Ando. From Fig. 3.10 at 90° (χ_{\perp}), both metallic (6,6) and semiconductor (6,5) are diamagnetic, as a result of the induced current from the benzene rings of graphene. But as θ decreases to 0° (χ_{\parallel}), the metallic nanotube's χ increases to be

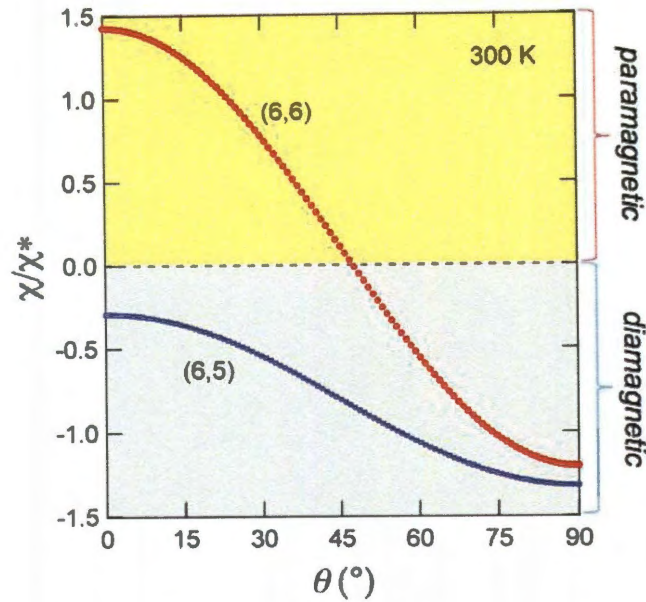


Figure 3.10 : Angular dependence of magnetic susceptibility χ for (6,6) and (6,5) SWNTs at 300 K, where $\theta = 90^\circ$ is χ_\perp and $\theta = 0^\circ$ is χ_\parallel . Note that $\Delta\chi$ for metallic nanotubes (red) is almost 5 times larger than $\Delta\chi$ for semiconductor nanotubes (blue) when $\theta = 0^\circ$.

paramagnetic. Lu calculated magnetic susceptibility from the following equation [67]:

$$\chi = -\frac{\partial^2 F(H, T)}{\partial H^2} \quad (3.6)$$

where the free energy, $F(H, T)$, is a function calculated from the temperature, magnetic field and the band structure. As the magnetic flux increases through the nanotube, the equation changes for metallic nanotubes such that they exhibit orbital paramagnetism in that direction. This is a result of the bandgap increasing as due to the Aharonov-Bohm flux through the nanotube. Similarly, for semiconductor nanotubes, the bandgap decreases with magnetic field resulting in diamagnetism from Eqn. (3.6).

3.3.1 Derivation of Magnetic Alignment Energy for Carbon Nanotubes

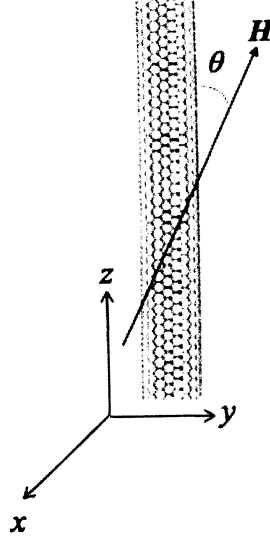


Figure 3.11 : Single carbon nanotube in the presence of magnetic field H in real space (x, y, z coordinates).

Suppose you have a single-walled carbon nanotube (SWNT) in the presence of a parallel magnetic field where the angle between the nanotube and the applied field is given by θ . Then, in real space a coordinate system is defined in Fig. 3.11 such that the z -axis is parallel to the nanotube axis, and the magnetic field is given by:

$$\vec{H} = (0, H \sin \theta, H \cos \theta) \quad (3.7)$$

The magnetic susceptibility in this coordinate system yields a magnetization of:

$$\begin{pmatrix} M_x \\ M_y \\ M_z \end{pmatrix} = \begin{pmatrix} 0 \\ N\chi_{\perp} H \sin \theta \\ N\chi_{\parallel} H \cos \theta \end{pmatrix} \quad (3.8)$$

where N is the number of carbon atoms per mole. Therefore, for the magnetic energy, $E(\theta, H)$, we have the following:

$$\begin{aligned}
 E(\theta, H) &= - \int \vec{M}(\vec{H}) \cdot d\vec{H} \\
 &= - \int M_x dH_x + M_y dH_y + M_z dH_z \\
 &= -N(\chi_{\perp} \sin^2 \theta + \chi_{\parallel} \cos^2 \theta) \int_0^H H dH \\
 &= -\frac{NH^2}{2}(\chi_{\perp} + \Delta\chi \cos^2 \theta)
 \end{aligned} \tag{3.9}$$

For the case when $\Delta\chi > 0$, the magnetic energy reaches a minimum at $\theta = 0$. Therefore, the magnetic alignment energy, $\Delta E(\theta, H)$ is defined as the difference in the magnetic energy between $E(\theta, H)$ and $E(0, H)$. Thus, from Eqn. (3.9):

$$\begin{aligned}
 \Delta E(\theta, H) &\equiv E(\theta, H) - E(0, H) \\
 &= \frac{NH^2}{2} \Delta\chi \sin^2 \theta
 \end{aligned} \tag{3.10}$$

yielding the potential energy of a nanotube with a finite angle θ with respect to the magnetic field. Note that all SWNTs have positive $\Delta\chi$, resulting in the alignment of carbon nanotubes in the direction of the applied magnetic field. Furthermore, the alignment of nanotubes coupled with the optical anisotropy of carbon nanotubes induces many magneto-optical effects where the degree of alignment is experimentally shown through an increase in the absorption of light incident on the nanotube. The following subsections will detail experiments where researchers exploit the novel magnetic properties of carbon nanotubes and the alignment energy to order carbon nanotubes with an applied magnetic field.

3.3.2 Static Magnetic Alignment in Carbon Nanotubes

Fujiwara et al. performed magnetic orientation of single carbon nanotubes suspended in carbon tetrachloride with fields up to 80.0 kOe [68]. They imaged the orientation of each nanotube with an SEM and applied the theory of magnetic alignment energy with Maxwell-Boltzmann statistics to estimate a degree of static alignment after the influence of the magnetic field. At low magnetic fields, Eqn. (3.10), is small, yielding a randomly aligned system by thermal energy. As the field is increased, the alignment energy found from Eqn. (3.10) is increased. Therefore, the probability that the nanotubes are aligned with magnetic field becomes higher. The probability density of an ensemble of SWNTs being at an angle θ with respect to the direction of the magnetic field is given by the angular Maxwell-Boltzmann distribution in spherical coordinates:

$$P(\theta) = \frac{\exp(-\Delta E/k_B T) \sin \theta d\theta}{\int_0^{\pi/2} \exp(-\Delta E/k_B T) \sin \theta d\theta} \quad (3.11)$$

From the orientation distribution (Eqn. (3.11)) and the magnetic alignment energy (Eqn. (3.10)), Fujiwara et al. also estimated the magnetic susceptibility anisotropy to be $\Delta\chi = (9 \pm 5) \times 10^{-6}$ emu/mol [68].

Independently, Walters et al. utilized magnetic energy to align carbon nanotubes in membranes with the 19 T superconducting magnet in Tallahassee [69]. Their goal was to produce a macroscopic film of aligned carbon nanotubes. They predicted that for the metallic armchair (10,10), a field of 15.3 T would be sufficient to align the nanotubes in the sample at room temperature [69]. With the use of a HeNe

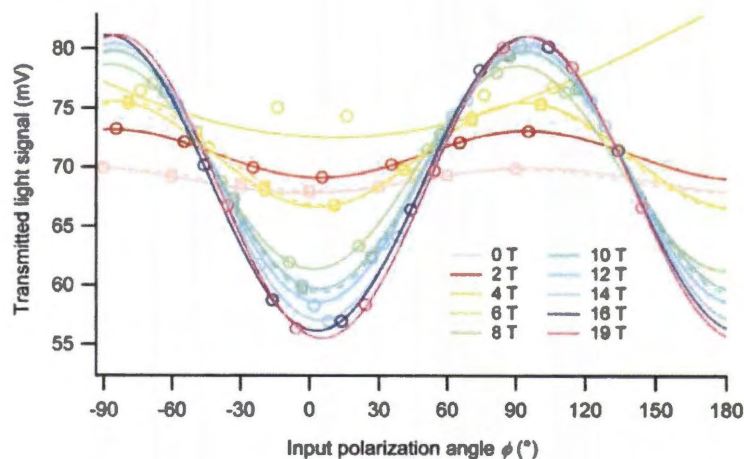


Figure 3.12 : Optical transmission as a function of incident polarization angle at magnetic fields up to 19 T. Fields above 10 T showed the highest alignment as the transmitted signal for those fields had the highest signal at 90° and the lowest signal at 0°. Adapted from Ref. [69].

laser, Walters et al. increased the magnetic field and observed the transmission as a function of polarization angle. From their results (Fig. 3.12), they found that marked alignment occurred at fields above 10 T.

3.3.3 Dynamic Magnetic Alignment in Carbon Nanotubes

The previous section detailed two examples of using high magnetic fields to study the static alignment of carbon nanotubes with the goal of orienting the carbon nanotubes with the applied magnetic field. Shaver et al. posed the question of the dynamics of orientation of carbon nanotubes with magnetic field [70]. They utilized magnetic linear dichroism and pulsed magnetic fields to measure the dynamic alignment of carbon nanotubes in peak fields up to 166 T [70]. As the magnetic field

pulse increases, the carbon nanotubes align with B showing an increase in the transmission of light polarized parallel to B . By measuring the transmission parallel and perpendicular to the magnetic field (Fig. 3.13), the authors were able to estimate length distributions in their respective samples with the implementation of Brownian motion and linear dichroism theory [70].

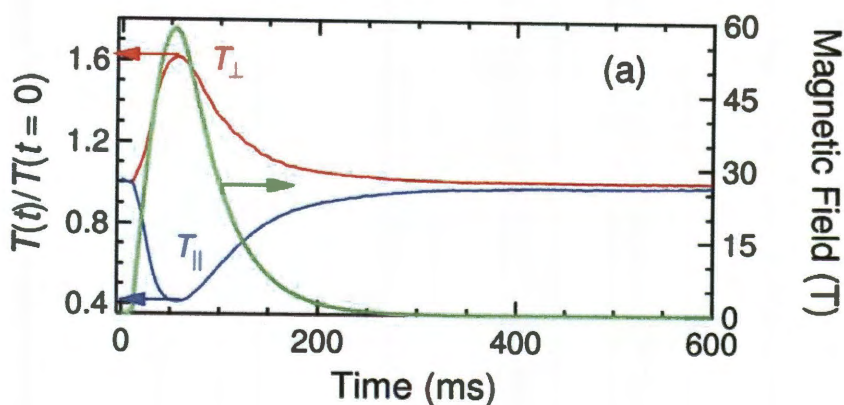


Figure 3.13 : Transmission of laser light as a function of time at magnetic fields up to 60 T. The magnetic field pulse (yellow) is shown with the red perpendicular transmission and blue parallel transmission traces. Therefore, the increase (decrease) in transmission is directly from the alignment of the nanotubes with the magnetic field pulse. From this information, one can calculate the dynamic magnetic linear dichroism. Adapted from Ref. [70].

Although the authors obtained valuable information about the dynamics of the alignment of carbon nanotubes in very large magnetic fields, this particular method of magnetic linear dichroism (using a single laser line), yielded no information about the chirality of nanotubes investigated in this experiment. Therefore, chiral specific estimations of the magnetic susceptibility can not be made with these methods.

3.4 Anisotropy in the Magnetic Susceptibility of Semiconductor Carbon Nanotubes

3.4.1 Estimation of $\Delta\chi$ using Magneto-Photoluminescence

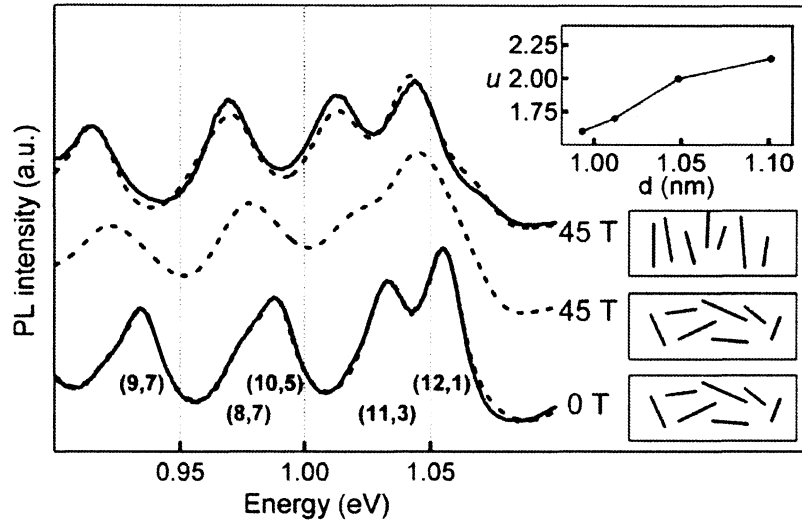


Figure 3.14 : Three magneto-photoluminescence spectra of HiPco SWNTs at 0 T (bottom), 45 T with light polarized perpendicular to B (middle), and 45 T with light polarization parallel to B (top) from Ref. [71]. Note that for all chiralities present, there is a substantial redshift for each peak from 0 T to 45 T. The inset shows the diameter dependence of u as defined in Section 3.4.1 and each of the cartoons correspond to the spectra highlighting the alignment of the nanotubes at each field.

Zaric et al. were the first to experimentally confirm the theoretical predictions presented by Ajiki, Ando, and Lu with their measurements on HiPco nanotubes in solution. They performed magneto-photoluminescence excitation (PLE) spectroscopy up to 45 T [71] as seen in Fig. 3.14. The magnetic susceptibility anisotropy was estimated by measuring the amount of redshift in the photoluminescence (PL) spectrum and extracting values for u , a dimensionless ratio of the alignment energy and the thermal

energy. This parameter u is a function of N the number of carbon atoms per unit length, magnetic field B , and temperature T .

They then related their values for u with the Maxwell-Boltzmann distribution function (Eqn. (3.11)) for the probability density of an ensemble of SWNTs being at an angle θ with respect to the direction of the magnetic field. Using Eqn. (3.11) and the definition of u , they found that for their sample, $\Delta\chi$ increased linearly with diameter. Furthermore, they confirmed that $\Delta\chi$ is $\sim 10^{-5}$ emu/mol for semiconductor SWNTs [59, 66, 67].

3.4.2 Chirality Dependence of $\Delta\chi$ in Semiconductor Nanotubes

Until the work of Marques et al., it was assumed that there was no chiral dependence of the magnetic susceptibility anisotropy only a diameter dependence (χ increases linearly with d). In their study, they showed theoretically that $\Delta\chi$ for zigzag semiconducting nanotubes (where $m = 0$ for (n, m) chirality) is also a function of the chiral angle [72]. In their results, they found a family dependence in which nanotubes of family $l = 2$ showed little diameter dependence but all others showed a decrease in χ as a function of diameter. Interestingly, like Ajiki & Ando and Lu, the values calculated for $\Delta\chi$ were close in agreement earlier studies on the same order of diameter.

At much lower magnetic fields than Zaric et al. (up to 7 T), the Kikkawa group at University of Pennsylvania continued their work on magnetic alignment by carrying

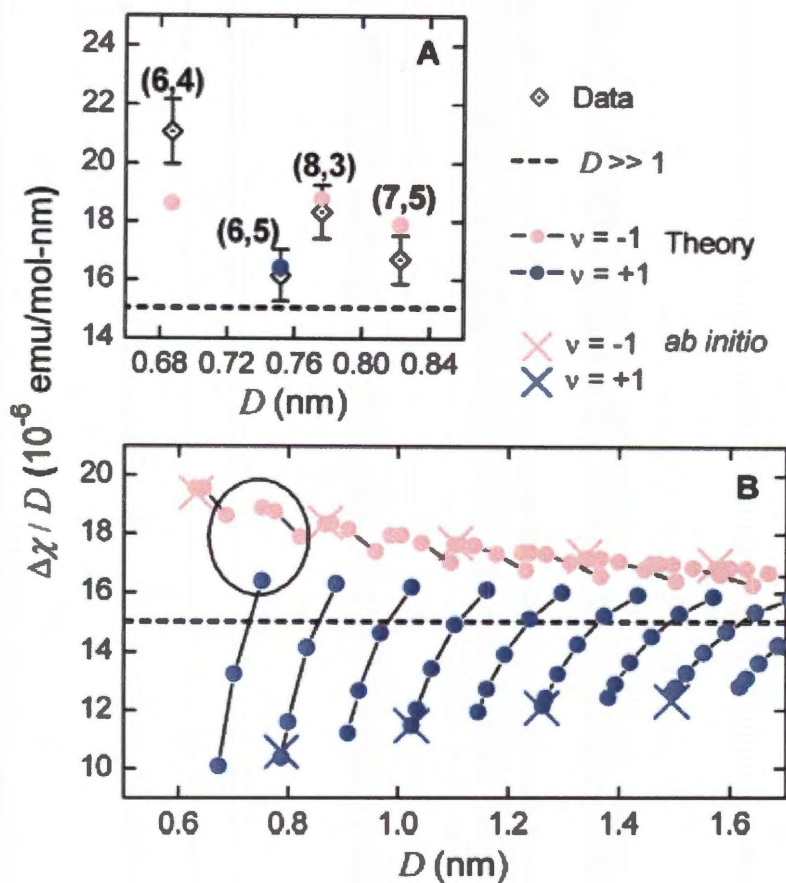


Figure 3.15 : $\Delta\chi$ as a function for diameter for semiconductor CoMoCAT nanotubes from Ref [73]. The data in (a) is fit to the family dependent theory shown in (b) for many nanotubes.

out magneto-PL measurements on DNA-wrapped CoMoCAT SWNTs. They were able to subtract out the magnetic susceptibility anisotropy of DNA [73] ($\Delta\chi \sim 0.86 \pm 0.3 \times 10^{-6}$ emu/mol) to measure four different magnetic susceptibility anisotropies for the (6,5), (7,5), (8,3) and (6,4) semiconducting nanotubes. As a result, they found

that the diameter dependence predicted by Ajiki, Ando, and Lu was not valid for the nanotubes in their sample. Their values for $\Delta\chi$ followed a chiral index/family dependent model as seen in Fig. 3.4.2. This effect is larger for smaller diameter tubes, ($d < 1$ nm). Furthermore, the smallest diameter nanotube (6,4) exhibited the highest $\Delta\chi$. Due to their method of measurement (PL), there was no information on the metallic carbon nanotubes present in their sample to investigate the magnetic susceptibility or the diameter dependence of $\Delta\chi$ in such carbon nanotubes.

Chapter 4

Magnetic Susceptibility Anisotropy in Metallic Carbon Nanotubes

Magnetic linear dichroism spectroscopy measurements on length-sorted, (6,5)-enriched CoMoCAT and metallic armchair-enriched HiPco SWNTs were made using the 35 T Hybrid Magnet in the High Magnetic Field Facility of the National Institute for Materials Science in Tsukuba, Japan. We present the first experimental estimation of the magnetic susceptibility anisotropy of metallic single-walled carbon nanotubes showing their large susceptibility anisotropy [74]. We also present a comparison of the magnetic susceptibilities of metallic and semiconducting nanotubes within the same sample and show that the susceptibilities are 2 - 4 times greater in metallic nanotubes. Finally, we show, contrary to the assumption that $\Delta\chi$ increases linearly with d , that the magnetic susceptibility anisotropy in metallic carbon nanotubes does not depend on diameter.

4.1 Experimental Methods

4.1.1 Sample 1: (6,5)-Enriched CoMoCAT Solution

CoMoCAT SWNTs were suspended in 1% sodium deoxycholate (DOC) and length sorted by dense liquid ultracentrifugation [75] to have an average length of ~ 500 nm.

Photoluminescence excitation (PLE) and absorption spectroscopies for this CoMoCAT sample can be seen in Figs. 4.1 and 4.2, respectively. Note that the sample is separated for a single chirality (6,5) although other chiralities are present in the PLE map. Also, note that PLE is limited to only information about semiconducting nanotubes in the sample because metallic nanotubes do not fluoresce due to the absence of a bandgap. Metallic nanotubes present in this sample are the (5,5), (6,6) and (7,4) chiralities.

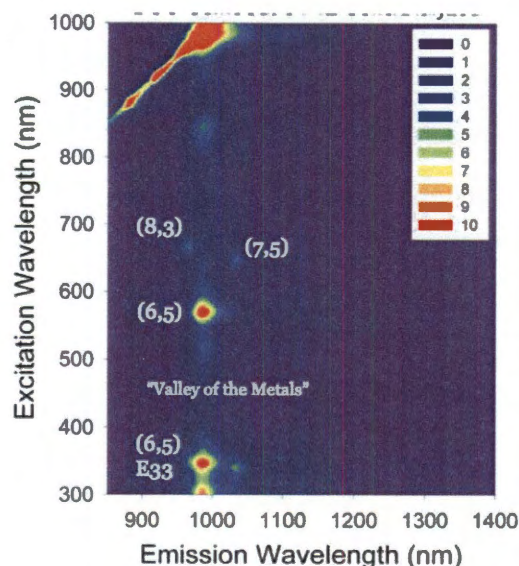


Figure 4.1 : Photoluminescence excitation map of our NIST (6,5)-enriched length-sorted CoMoCAT sample. Note that there are only a few chiralities present. Also note that in the “Valley of the metals”, from excitation wavelength 400 to 500 nm, there is no luminescence present.

Conversely, absorption spectroscopy yields qualitative information about the individualization, interband transitions, and chiralities present in a given sample for both metallic and semiconducting nanotubes. In the range of 1 to 5 eV, there are five

main optical transitions for SWNTs as labeled in Fig. 4.2: a) E_{11} semiconductor, b) E_{11} metallic, c) E_{22} semiconductor, d) E_{33} semiconductor, and e) E_{44} semiconductor transitions. For this sample, there is a very high absorbance in E_{11} of (6,5) in comparison to that of E_{22} and other optical transitions of other chirality nanotubes. This was achieved by combining several long fractions from three different but similar CoMoCAT batches.

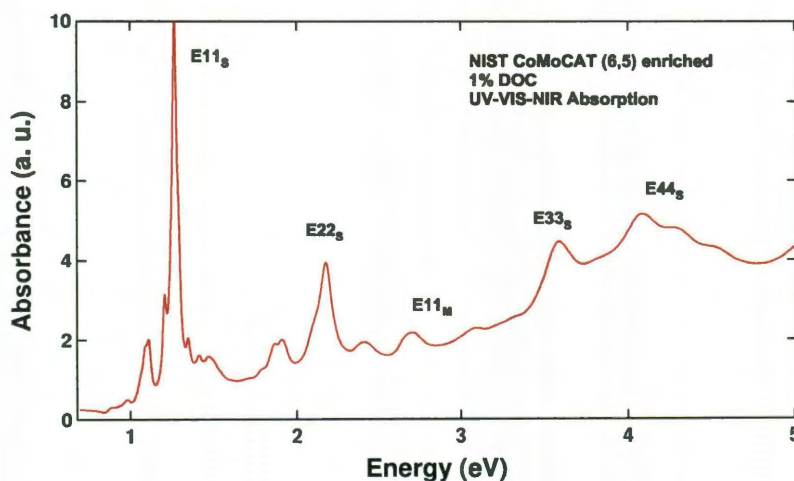


Figure 4.2 : Absorbance spectra from absorption spectroscopy of our NIST (6,5)-enriched length-sorted CoMoCAT sample.

In each case, the nanotubes were dispersed with 1 hour tip sonication (1/4" tip, ~ 35 mL batches, in ice bath) in 2% mass/vol DOC solution. The liquid was then centrifuged for 2 hours at 10 °C and 18000 RPM in a JA-20 rotor, which provides roughly 38000 g max acceleration. After the two hours, the supernatant was collected and the bottoms discarded. These solutions were then concentrated against a 30 kD membrane to increase the concentration, and then length sorted via ultracentrifuga-

tion at either 12000 RPM (15 °C) or 25300 RPM (4 °C) in a SW-32 rotor for either \sim 74 hours or 21 hours, respectively (equivalent integrated accelerations). The length separation was done in either 2% DOC, 18% mass/vol iodixanol top layers or with a 2% DOC, 15% mass/vol iodixanol top layer [76]. Fractions were sequentially extracted from the top and like fractions were combined from multiple tubes/runs. For this sample, fractions from different batches of similar length were added together, and the iodixanol removed by use of a forced filtration cell (with a 30 kD membrane), with exchange into 1% DOC.

In comparison to previous work [61, 71], our sample also provided two distinct advantages for performing this experiment. First, our sample was length-sorted to yield an average length. Size exclusion chromatography is a well developed technique that has been compared with atomic force microscopy (AFM) to insure the accuracy of the lengths produced [75]. Furthermore, in Ref. [61], the average length was reported to be 300 nm, and therefore, the alignment from our sample should be better because we are using longer tubes, \sim 500 nm. The second advantage of our sample comes from the fact that it is enriched for the (6,5) chirality from CoMoCAT batches. For our previous magneto-absorption spectroscopy with unsorted HiPco [61], results and analysis were very complicated due to the many different chirality nanotubes present in that type of sample. With our sample, we are limited to a small number of chiralities with four dominate semiconducting species [(8,3),(6,4),(7,5) and (6,5)] and three metallic species [(6,6), (7,4) and (5,5)].

4.1.2 Sample 2: Armchair-Enriched HiPco Solution by Density Gradient Ultracentrifugation

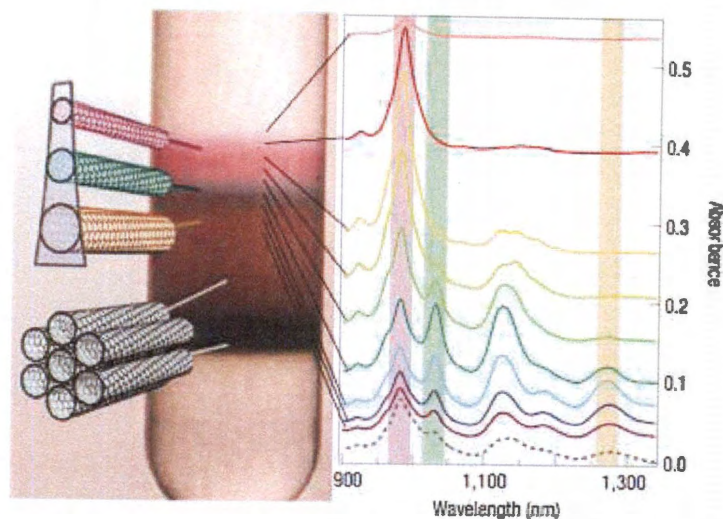


Figure 4.3 : Absorbance spectra with respect to each colored band in the photograph (left) from a density gradient ultracentrifugation process. Note the spectra are intentionally offset to match the layer of the gradient with the most chirality separation occurring at the top layer. Adapted from [77].

Sample preparation methods to achieve chirality and metallic separations have created a very rich field, and further progress will only yield a more ideal system to study 1D physics in nanotubes. It will hopefully also lead to many useful applications for SWNTs. The major challenge preventing widespread technology on chirality separation is that the yields produced by methods like density gradient ultracentrifugation (DGU) [77] and other separation techniques like DNA sequencing are much lower than anything useful for applications at this time; on the order of 0.1 to 0.8 μg per 100 μg [78].

For our measurements, we applied a density gradient method to selectively isolate armchair, (n, n) , metallic nanotubes. Density gradient ultracentrifugation [77] manipulates the density of nanostructures with a series of surfactants to separate nanotube solutions by layers of different density. The selection and procedural application of each surfactant is used to produce a gradient as seen in Fig. 4.3. As a general rule, particles with similar density settle in layers with the most dense particles (pellets, bundles, etc.) composing the bottom layers, and each layer decreases in density as you travel up the gradient. DGU has been shown to be an effective form of separation for metallics, semiconductors, and even specific (n, m) chiralities [77, 79, 80].

Recently, Háróz et al. reported a modified density gradient ultracentrifugation procedure that selects for armchair and near-armchair carbon nanotubes [80]. Thus, it was this procedure that we employed for our study. As with most DGU processes, we began with a usual ultracentrifugation decant as described in Ref. [9]. Then, the SWNTs are taken through a three-surfactant process to yield the metallic enrichment. The first surfactant is dispersion in 1% DOC, which insures individualization, through bath sonication for 30 minutes followed by a long sonication of 17.5 hours at 10°C. This solution is then centrifuged for 1 hour at 208400 g . In the second step, the top 80% of the current solution is combined with a mass density gradient composed of 1.5% (wt/vol) sodium dodecyl sulfate (SDS), 1.5% (wt/vol) sodium cholate (SC), and varying layers of iodixanol. In a centrifuge tube, we first insert the bottom layer of 40% (wt/vol) iodixanol. Then, we create the SWNT supernatant layer (consisting

of 1 mL of our SWNT solution, 30% iodixanol, 1% SDS, and 1% SC) and add it to the centrifuge tube. After this step, we add the following layers of iodixanol in order of addition: 27.5%, 25%, 22.5%, and 20% (wt/vol). This is then centrifuged for 18 hours at 208400 g . The layers are separated by hand-pipetting of 200 μL fractions and finally dialyzed into 1% DOC solution.

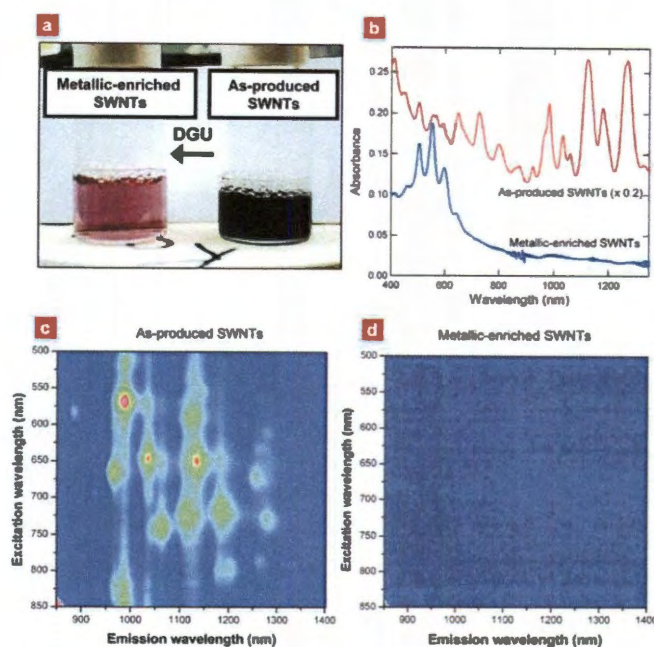


Figure 4.4 : (a) Photograph of metallic and as-produced SWNTs (b) Absorbance spectra of our DGU sample and the as-produced SWNTs. Note that the semiconductor portion of the spectra is not present in the metallic enriched SWNTs. (c) PLE of as-produced SWNTs (d) PLE of metallic-enriched sample. Adapted from [80].

Absorption and PLE comparisons of the as-produced SWNT and metallic-enriched solutions can be seen in Fig. 4.4. Note that in Fig. 4.4(a) the color of the metallic-enriched solution is drastically lighter than the nearly black coloring of the broadly absorbing as-produced SWNTs and the PLE (Fig. 4.4(d)) of the metallic-enriched

sample is completely absent of PL “hotspots”. We chose to use this sample for our secondary study of diameter and not Sample 1 mainly because of this fact, i. e., there is little contribution from overlapping E_{22} semiconductor transitions. Furthermore, we gain additional information not present in the NIST sample (Sect. 4.1.1) due to the presence of larger diameter (n, n) nanotubes.

4.1.3 Hybrid Magnet at Tsukuba Magnet Laboratory, National Institute for Materials Science

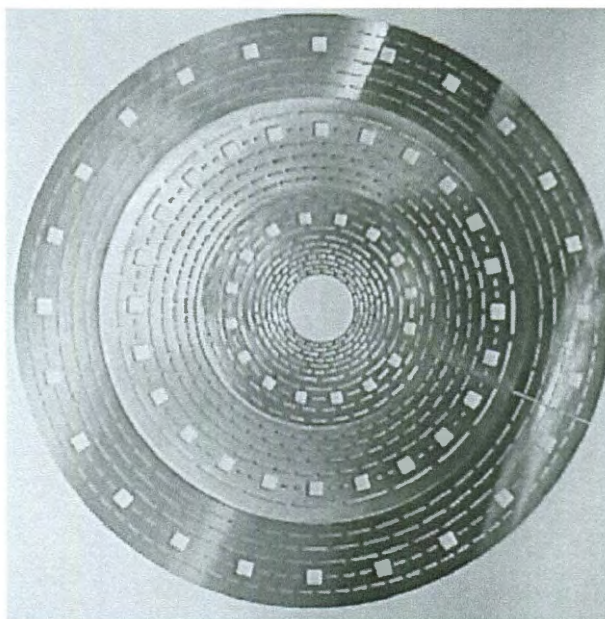


Figure 4.5 : Resistive Magnet Insert Coils of Bitter Magnet for the NIMS 35 T Hybrid Magnet, Tsukuba, Japan. There are three coils that together with the superconducting magnet allow for users to attain a maximum DC magnetic field of 35 T. Adapted from [81].

The hybrid magnet at the National Institute for Material Science allows users to

operate at DC fields up to 35 T [81]. The term hybrid comes from the fact that the resistive insert sits inside of the 400 mm bore of a superconducting magnet whose maximum field is 14.2 T . The resistive insert is made up of three Bitter magnet coils (Fig. 4.5) with 10.4 T coming from the inner coil, 7.9 T from the middle coil and 5.8 T from the final outer coil.

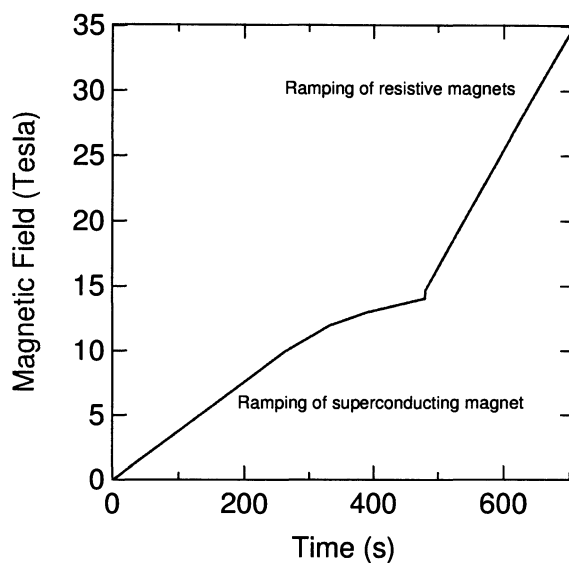


Figure 4.6 : Ramping up-sweep of the Tsukuba Magnet Laboratory Hybrid magnet from 0 to 35 T. The initial rise is due to the increase of B from the superconducting magnet up to 14.2 T. Then there is a sharp rise to 35 T using the resistive magnets.

Adding these fields together gives a total of 37.3 T only surpassed in DC fields by the 45 T Hybrid at the National High Magnetic Field Laboratory in Tallahassee, FL [62]. The sample space for this magnet is 32 mm and is held at room temperature. An example full-field ramping of the magnetic field from 0 to 35 T is plotted in Fig. 4.6.

4.1.4 Experimental Setup

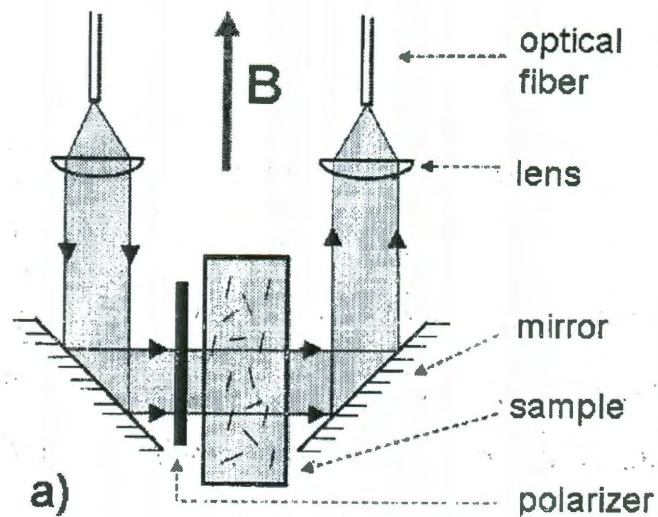


Figure 4.7 : Optical path of Magnetic Linear Dichroism Spectroscopy Probe [82].

For both experiments, a Xe lamp fiber coupled to a custom optical probe allowed for broadband white-light excitation of the E_{11} metallic, E_{22} semiconductor, and E_{33} semiconductor optical interband transitions of SWNTs. The solution sample was held in a cuvette with a film polarizer directly on the front face to allow for linear polarization of the incident light. Collimated light was collected with another fiber and dispersed through a monochromator where the spectra were measured using a Si

CCD. A schematic of the sample probe is shown in Fig. 4.7. The temperature of the sample was ~ 300 K.

4.2 Large Anisotropy in the Magnetic Susceptibility of Metallic Carbon Nanotubes

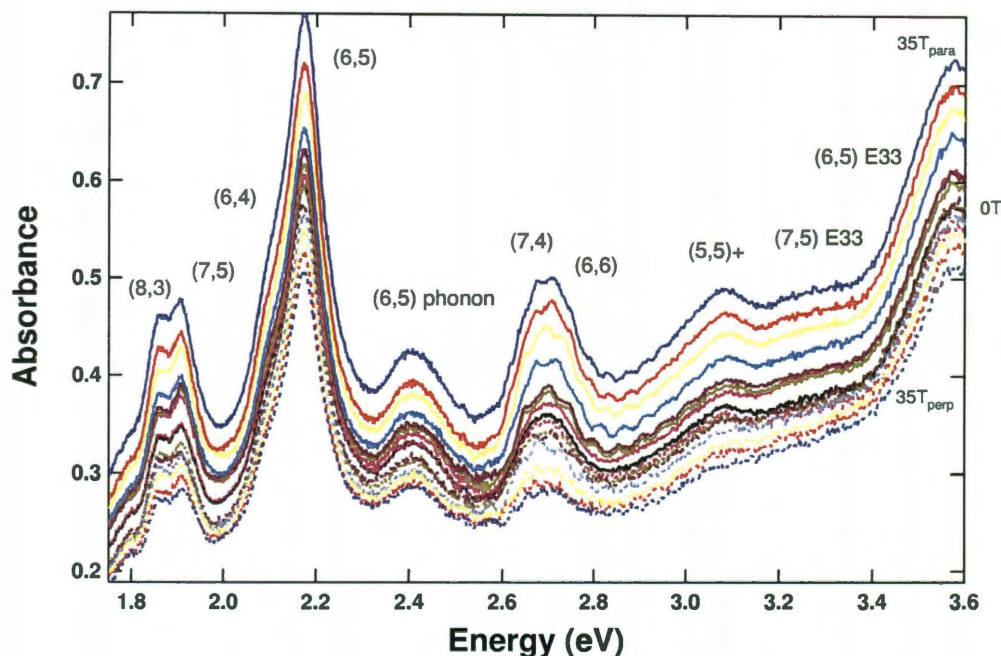


Figure 4.8 : Magnetic linear dichroism spectroscopy of (6,5)-enriched CoMoCAT nanotubes from 0 to 35 T. Each peak corresponds to a different (n, m) nanotube. As the magnetic field is increased the absorbance increases/decreases with light polarized parallel/perpendicular to B .

The spectra from our magnetic linear dichroism spectroscopy of Sample 1 (Sect. 4.1.1) from 0 to 35 T are shown in Fig. 4.8. The data is not intentionally offset, indicating an increase in absorbance for light polarized parallel to the nanotube axis, and a

decrease in absorbance for light polarized perpendicular to the nanotube axis. This is due to the fact that nanotubes selectively absorb light in the direction along the nanotube axis corresponding to the amount of the alignment caused by the increase in magnetic field.

From the theory of linear dichroism for an ensemble of anisotropic molecules [83], the following quantity can be shown to be constant, independent of the degree of alignment:

$$A_0 \equiv \frac{A_{\parallel} + 2A_{\perp}}{3}. \quad (4.1)$$

Here, A_{\parallel} describes the absorption of light polarized parallel to the orientation axis, and A_{\perp} describes absorption of light polarized perpendicular to the orientation axis. A_0 for 35 T is also shown in Fig. 4.9 as a red dashed line. Note that it coincides

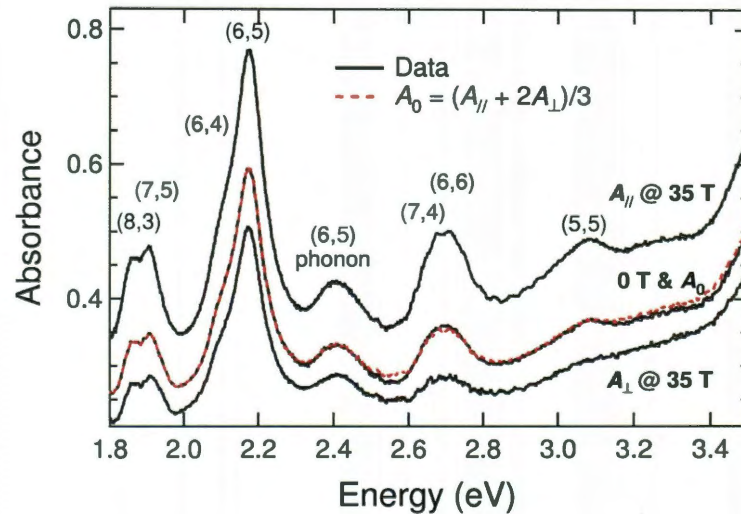


Figure 4.9 : Absorbance spectra (solid black) for 0 T and 35 T with all peaks assigned from our sample. The unpolarized isotropic absorbance (dashed red) is calculated from the magnetic field data and agrees well with that of the 0 T data.

with absorbance at 0 T, confirming that A_0 is indeed independent of alignment (or B). This is because at 0 T, $A_{\parallel} = A_{\perp}$. For subsequent fields ($B \neq 0$), the increase in absorbance for A_{\parallel} and the decrease of absorbance seen in A_{\perp} is such that the ratio of the two still preserves A_0 (Eqn. (4.1)).

Linear dichroism (LD) is defined as the difference between the absorbance of polarized light parallel to the orientation axis and the absorbance of the polarized light perpendicular to the orientation axis. To adjust for differences in relative absorbances due to the fact that our sample is enriched for (6,5), the LD is divided by A_0 yielding the following result for reduced LD (LD^r) [83]:

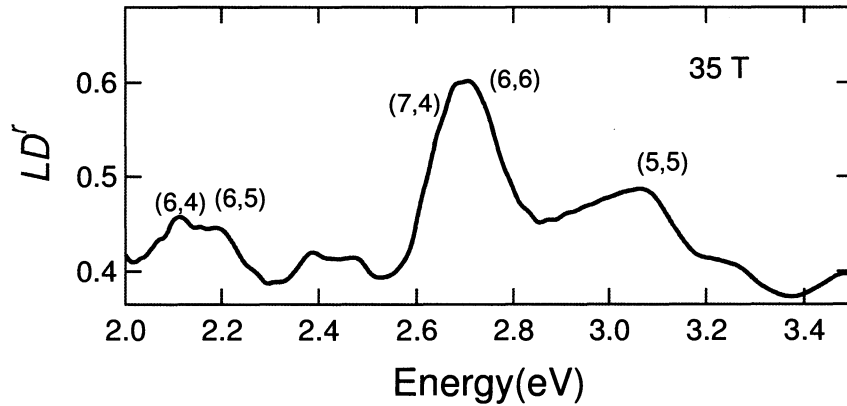


Figure 4.10 : Reduced linear dichroism vs Energy (eV) from measured data. The largest peak is from metallic nanotubes (6,6) and (7,4). This is opposite of the case for the Absorbance spectra from Fig. 4.9, where the semiconductors (6,5) and (6,4) dominate the spectra.

$$LD = A_{\parallel} - A_{\perp} \quad (4.2)$$

$$LD^r = \frac{LD}{A_0} = 3 \left(\frac{3 \cos^2 \alpha - 1}{2} \right) S \quad (4.3)$$

where S is the nematic order parameter describing the degree of alignment for an optically anisotropic rigid rod whose angle α determines the angle between the rigid rod and that of the transition moment. For our case, the absorbance of light that is measured is only from light absorbed along the tube axis. Therefore, $\alpha = 0$; and furthermore, Eqn. (4.3) becomes:

$$LD^r = 3 \left(\frac{3 \cos^2 \alpha - 1}{2} \right) S = 3S \quad (4.4)$$

The measured values for LD^r spectra at $B = 35$ T can be seen in Fig. 4.10. Qualitatively, it is evident that the region of E_{11} metallic transitions (~ 2.5 to 3.2 eV) has the largest values for LD^r , but detailed fitting is required to extract the magnetic alignment properties of each chirality nanotube present in our sample.

4.2.1 Fitting Methods

The results in Fig. 4.8 along with other magnetic fields up to 35 T were fit utilizing the following expression:

$$A_{\text{fit}} = A_{\text{offset}} + \sum_{i=0}^N A_{\text{nanotubes}}^i \quad (4.5)$$

where $i, N \in \mathbb{Z}^+$ and the absorption peak of each chirality in our sample, $A_{\text{nanotubes}}^i$, is represented as a Lorentzian. The linewidth of each Lorentzian was consistent with previous work for absorption spectroscopy in the visible and ultraviolet [36, 84, 85]. Applying this algorithm to each magnetic field, we held the peak centers and widths constant at the values determined at $B = 0$ and allowed amplitudes to float freely.

For increasing magnetic field parallel with the light polarization, the amplitude of each Lorentzian is increased in the same manner as the absorbance of each spectrum. Similarly, as the magnetic field increased with light perpendicular to the tube axis, the amplitudes of the Lorentzians decreased.

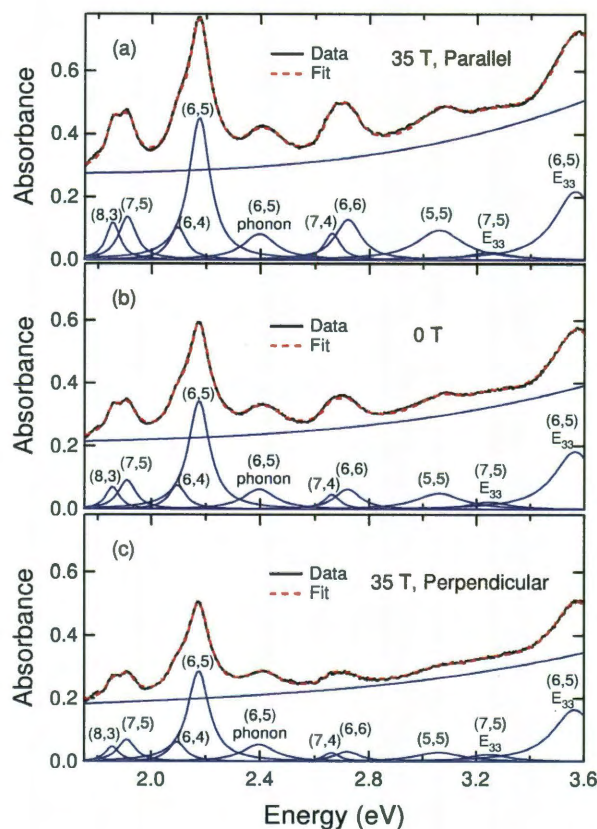


Figure 4.11 : Fitting results for 0 T and 35 T. The data (black) is fit by the sum of each individual chirality nanotube (blue) and the addition of a susceptible offset (blue). The sum of these individual fits is shown as a red line. All spectra were fit simultaneously and data for subsequent fields was performed in the same manner.

Due to the proximity of our spectral range (1.75 to 3.6 eV) with ultraviolet spectral features such as the π plasmon peaks [86] and E_{44} semiconductor transitions, we added

a nonlinear offset to our fitting equation also seen in Fig. 4.11 and denoted by A_{offset} . After adding each Lorentzian with the respective offset, the fit for that field can be made with the experimental data as seen in Fig. 4.11 as a red dashed line. The physics behind this offset can be attributed to π -plasmon peaks, pellets, bundles, light scattering etc. [84,85]. Regardless of its origin, the offset shows a dependence in magnetic linear dichroism, which can be seen in Fig. 4.11 by looking at the difference in each offset for 0, 35 T parallel and 35 T perpendicular.

For each magnetic field, the parallel and perpendicular spectra were fit simultaneously with the 0 T spectrum. The following constraints were imposed on the fitting equation for each Lorentzian to preserve the optical anisotropy intrinsic to each nanotube feature:

$$A_{i0} = \frac{A_{i\parallel} + 2A_{i\perp}}{3} \quad (4.6)$$

where $i = 1, 2, 3$, etc. corresponding to each Lorentzian or chirality nanotube, and the amplitude, A . The decomposed fits for 0 T and 35 T can be seen in Fig. 4.11 with each Lorentzian assigned to a different chirality.

4.2.2 Fitting Results

Figure 4.12 shows the Lorentzians resulting from fitting for the (7,5), (6,5), (6,6), and (5,5) nanotubes at 0 and 35 T. These Lorentzians along with the others for the nanotubes present in our sample were used with Eqns. (4.2) and (4.3) to calculate LD and LD^r , respectively. Note that LD^r shown in Fig. 4.13 is different than that

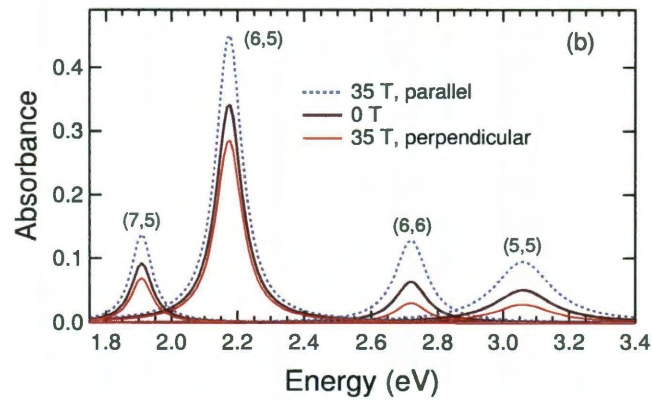


Figure 4.12 : Lorentzians for different chirality nanotubes at 0 and 35 T.

shown previously in Fig. 4.10. This is a direct result of calculating LD^r from each Lorentzian of different chirality versus calculating LD^r from the entire spectra of measured data; i.e., all of the chiralities at once.

Furthermore, from our fitting procedure, LD for each chirality nanotube should just be a Lorentzian. Thus, from mathematics, we know that dividing by a Lorentzian of the same peak center and width should yield a constant value for LD^r . This is also confirmed by the fact that Eqn (4.3) yields a constant value for LD^r because S by definition is constant. As a result, one can extract information on the alignment for each nanotube. It is evident from Fig. 4.13 that the values are much larger for the metallic than the semiconducting nanotubes suggesting that the alignment is higher at 35 T.

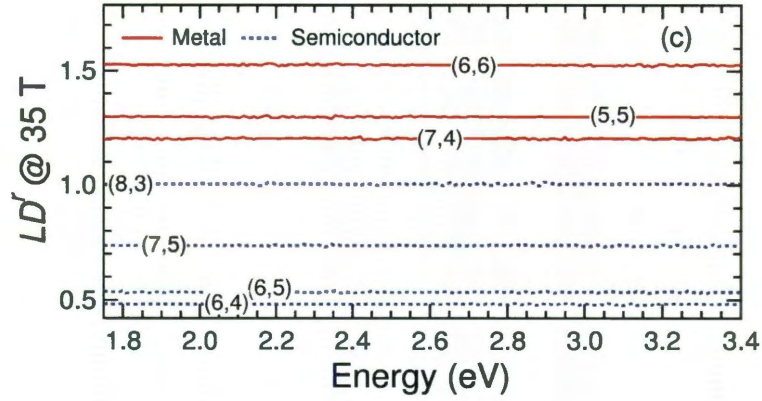


Figure 4.13 : LD^r vs. Energy (eV) derived from fitting for each individual chirality nanotube in our sample. The metallic tubes (red) are higher than the semiconducting nanotubes (blue dotted).

The nematic order parameter S is defined as the degree of alignment such that

$$S \equiv \frac{3 \langle \cos^2 \theta \rangle - 1}{2} \quad (4.7)$$

where $\langle \dots \rangle$ is the average value. For the case of our experiment, θ is the angle between the magnetic field and the nanotube axis. Thus, for the case when $S = 0$, the nanotubes are completely randomized due to Brownian motion. Conversely, when $S = 1$, all nanotubes in the solution are completely aligned upright with the axis.

We can then use the relation $S = LD^r/3$ to calculate measured S from LD^r of each chirality as seen in Fig. 4.14 and extract a measure of alignment. Due to the fact that our measurements were at $B > 1$ T, the effect of ferromagnetic material present in our sample will be saturated and did not effect our measured values for S or $\Delta\chi$ [87]. S as a function of magnetic field is plotted in Fig. 4.14 with the largest alignment seen from both armchair nanotubes ($n = m$ for (n, m) chirality nanotube).

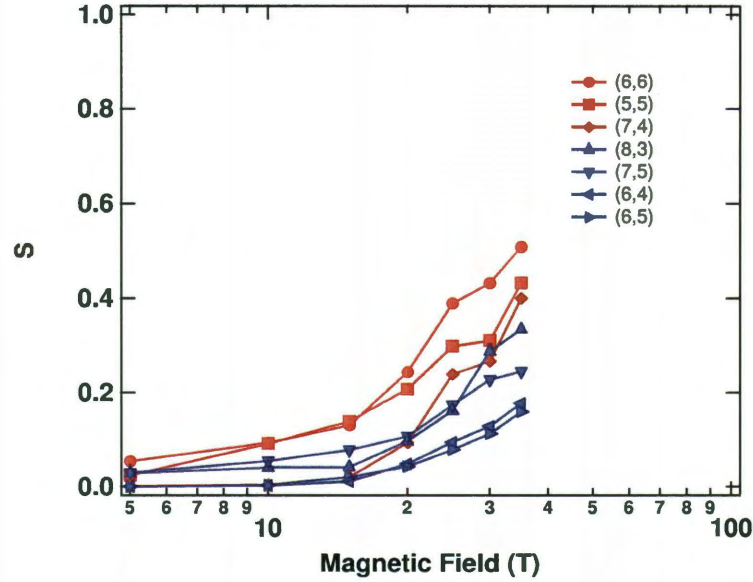


Figure 4.14 : S vs. B for all (n, m) nanotubes present in $(6,5)$ enriched carbon nanotubes. The lines are not fits, but are used to guide the eye. Also, the red metallic nanotubes all have higher S values as a function of B than the blue semiconductor nanotubes.

4.2.3 Discussion

The probability of an ensemble of nanotubes to align with angle θ between the nanotube axis and B can be approximated by the Maxwell-Boltzmann distribution [71]:

$$P_u(\theta) = \frac{\exp(-u^2 \sin^2 \theta) \sin \theta}{\int_0^{\pi/2} \exp(-u^2 \sin^2 \theta) \sin \theta d\theta} \quad (4.8)$$

where $u = \sqrt{\frac{B^2 N \Delta\chi}{2k_B T}}$ is a dimensionless measure of the relative importance of the magnetic alignment energy ($B^2 N \Delta\chi$) and the thermal energy ($k_B T$). Here N is the number of carbon atoms per average length of the nanotubes in our sample (500 nm), k_B represents Boltzmann's constant, and T is the temperature.

For the specific case of an ensemble of nanotubes aligning with magnetic field

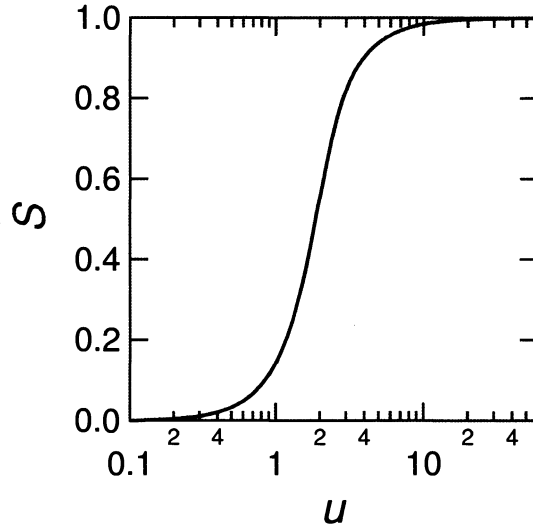


Figure 4.15 : Theoretical model of S vs. u , where S is the nematic order parameter and u is a dimensionless quantity relating the alignment energy and the thermal energy as defined in the text.

in solution with probability $P_u(\theta)$, we can derive the following by making use of Dawson's function [88]:

$$S(u) = \frac{-1}{2} + \left(\frac{3}{4u^2} \right) \left(\frac{u}{\frac{\sqrt{\pi}}{2} e^{-u^2} \operatorname{erfi}(u)} - 1 \right) \quad (4.9)$$

where erfi is the imaginary error function ($\operatorname{erfi}(u) = \frac{2}{i\sqrt{\pi}} \int_0^{iz} e^{-t^2} dt$).

Using this equation for $S(u)$ as plotted in Fig. 4.15, we were able to extract $\Delta\chi$ for each nanotube as seen in Table 4.1. The values for the three metallic nanotubes, (7,4), (5,5), and (6,6), are all higher than those for the semiconducting nanotubes. Furthermore, it is evident that the magnetic susceptibility anisotropy of the metallic nanotubes here are consistent with the prediction [66,67] in that metallic nanotubes have $\Delta\chi \sim 2$ -4 times larger than those in semiconducting nanotubes, depending on

the diameter.

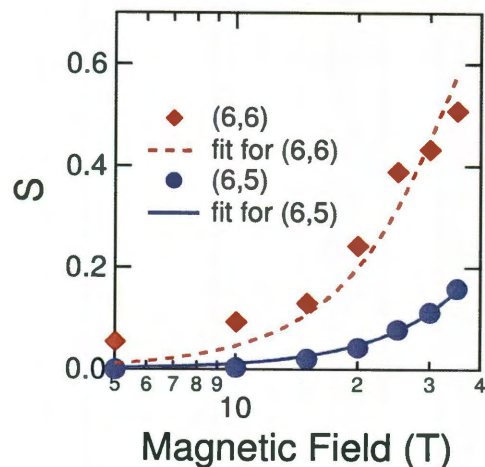


Figure 4.16 : S vs. B of (6,6) vs. (6,5). The nematic order parameter S is a measurement for the degree of alignment determined from Linear Dichroism theory. A higher S value corresponds to a higher degree of alignment. For the case shown in this figure the metallic (6,6) nanotube (red) has a higher S as a function of B than the semiconducting (6,5) nanotube (blue)

This large difference in magnetic susceptibility anisotropy is a direct consequence of the Aharonov-Bohm physics. The band structure changes in the form of the band gap opening in metallic nanotubes and the band gap shrinking for semiconducting nanotubes when the nanotubes are aligned parallel with the magnetic field. Specifically for metallic nanotubes, this causes a large orbital paramagnetism in the direction along the tube axis. This additional attraction towards the magnetic field manifests itself in the form of higher $\Delta\chi$. Figure 4.16 shows a direct comparison of the alignment with magnetic field for (6,6) and (6,5). Theoretically, larger anisotropy results in more alignment at lower fields, and higher at the same field and both of these

attributes are shown in this graph.

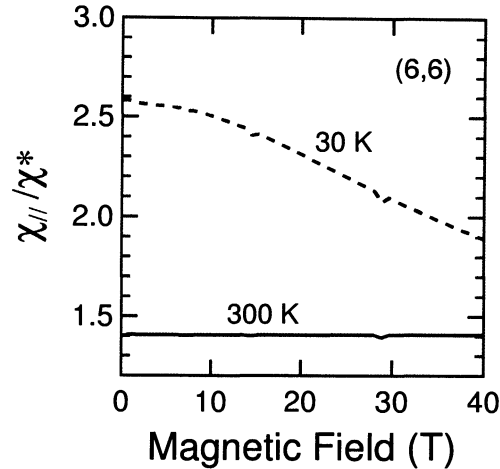


Figure 4.17 : Calculated magnetic field dependence of the parallel magnetic susceptibility of (6,6) nanotube for $T = 30$ K and 300 K in units of $\chi^* = 1.46 \times 10^{-4}$ emu/mol.

However, care must be taken in using this procedure since the values of χ_{\parallel} are expected to depend on B and T , especially for metallic nanotubes. Thus, we calculated $\Delta\chi$ as a function of B and T for all seven SWNTs studied in this work. Fortunately, in the perpendicular direction, for both semiconducting and metallic nanotubes, there is little contribution from these parameters [89]. Figure 4.17 shows a theoretical calculation of the B dependence of χ_{\parallel} for the (6,6) nanotube for 30 K and 300 K. Although χ_{\parallel} decreases by $\sim 27\%$ at 30 K as the field increases from 0 T to 40 T, it stays constant within $\sim 0.7\%$ at 300 K in the same field range, ensuring that the magnetic field dependence can be neglected for our room temperature measurements.

The values for metallic nanotubes in Table 4.1 do not follow a strict diameter dependence which is predicted for zigzag semiconducting nanotubes [72] and shown

Table 4.1 : Comparison of values of magnetic susceptibility anisotropy from previous theoretical and experimental studies and this work. For each chirality nanotube (n, m) , the diameter d and the chiral index ν is given followed by estimated theoretical and experimental values of $\Delta\chi$. All values for $\Delta\chi$ are $\sim 10^{-5}$ emu/mol with the first two columns of $\Delta\chi_{th}$ corresponding to theoretical predictions for 30 K and 300 K respectively. For the last two columns, $\Delta\chi_{exp}$ are measured values for $\Delta\chi$ with the last column for the present work.

(n, m)	d (nm)	ν	$\theta_{C_h} (^{\circ})$	$\Delta\chi_{th,30K}$	$\Delta\chi_{th,300K}$	$\Delta\chi_{exp}$	$\Delta\chi_{exp}$
(6,6)	0.81	0	30	6.38	3.92	—	3.63
(5,5)	0.67	0	30	5.32	3.39	—	3.35
(7,4)	0.75	0	21	5.92	3.70	—	2.44
(8,3)	0.77	-1	15	1.48	1.46	1.4	2.13
(7,5)	0.81	-1	24	1.57	1.55	1.4	1.66
(6,5)	0.74	1	27	1.44	1.42	1.2	1.01
(6,4)	0.68	-1	23	1.31	1.29	1.4	1.24

experimentally in chiral semiconducting nanotubes [73]. It is also important to note that the chiral metallic nanotube, (7,4), has a value for $\Delta\chi$ lower than those found in armchairs of this study. A detailed study on a metallic enriched sample should yield more metallic nanotubes to investigate this result (comparing metallic armchair, zigzag, and chiral nanotubes) in the future. Nonetheless, this work shows experimentally that for SWNTs $\Delta\chi$ is from 2-4 times larger (depending on the chirality) in metallic nanotubes in comparison to semiconducting nanotubes.

When evaluating $\Delta\chi$ for the semiconducting nanotubes in Table 4.1, it is in-

interesting to note that our values for $\Delta\chi$ are in agreement with values previously reported [61, 71, 73, 87]. $\Delta\chi$ extracted for (6,5) and (6,4) are similar to theoretical predictions for those chiralities. Our values for (8,3) and (7,5) are higher than those predicted [59, 66, 67, 72] and found experimentally by [61, 71, 73], but are lower than estimates previously reported for $\Delta\chi$ of similar diameter [87]. There may also be contribution from overlapping metallic transitions due to larger diameter metallic carbon nanotubes not resolved by our methods but still present in small quantities in our sample. Nonetheless as in previous studies [72, 73], our work does not follow a strict diameter dependence yielding further experimental evidence that $\Delta\chi$ is not just a function of diameter, but the chiral angle and the family dependence of chiral index ν are important factors to be explored by future work.

4.3 Diameter Dependence of $\Delta\chi$ in Metallic Carbon Nanotubes

Using Sample 2 (as described in Sect. 4.1.2), we were able to perform magnetic linear dichroism (MLD) spectroscopy on metallic-enriched carbon nanotubes up to 35 T. In comparison to our previous work (Sect. 4.2) on the magnetic susceptibility of metallic carbon nanotubes, in this study, we had the advantage of additional metallic nanotubes. We also utilized the absence of semiconducting nanotubes for less complication in our analysis in the form of overlapping semiconductor E_{22} transitions.

From Fig. 4.18, we see that there is a strong increase in absorbance for the spec-

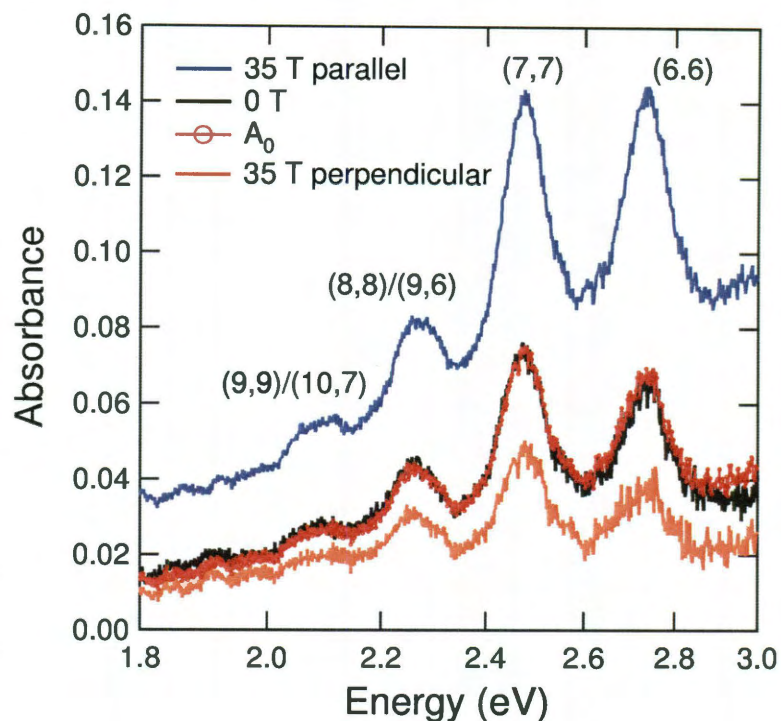


Figure 4.18 : Magnetic linear dichroism spectroscopy of metallic-enriched carbon nanotubes from 0 to 35 T. Each peak corresponds to a different (n,m) nanotube. As the magnetic field is increased the absorbance increases/decreases with light polarized parallel/perpendicular to B . Linear dichroism theory dictates that A_0 shown as red dotted line is equal to that of 0 T (black).

trum taken at 35 T parallel in all metallic chiralities. Furthermore, there is a decrease with respect to 0 T for the spectrum representing light polarized perpendicular at 35 T. The calculated A_0 , as was the case in the previous experiment (Sect. 4.2), lines up perfectly with data taken at 0 T. Another aspect of interest is the relative intensities at 0 T of the (6,6) versus that of the (7, 7) nanotube peak. It is clear that the (7,7) peak has a higher absorbance at 0 T. In fact, for 0 T, the (7,7) peak is the most dominant feature in the spectrum. However, this is not the case in the

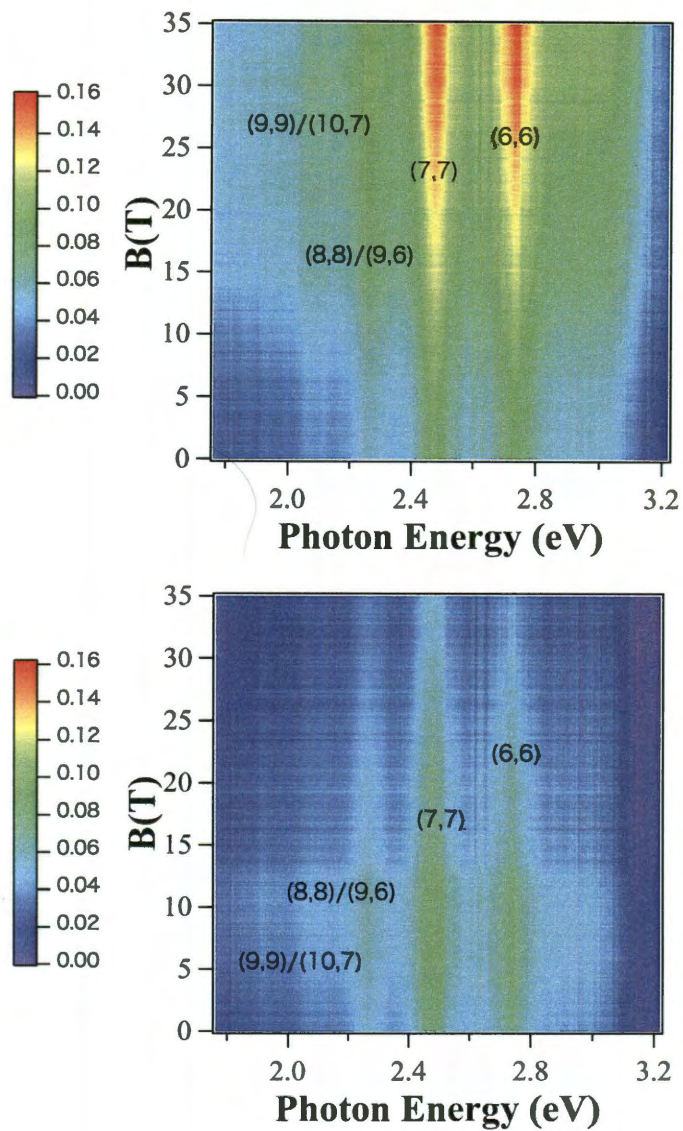


Figure 4.19 : (a) Absorbance as a function of magnetic field and energy for light parallel to the magnetic field. As the field increases you can see that the absorbance peaks corresponding to the metallic carbon nanotubes in our sample increase with increasing field. (b) Absorbance as a function of magnetic field for light perpendicular to B . As the field is increased, you see a decrease in the absorbance peaks with B .

parallel polarization spectrum at the highest field (35 T), where the (6,6) peak is now the most dominant feature. Furthermore, at the highest field and for perpendicular polarization, the (6,6) peak is smaller than the (7,7) peak, almost the same size as the (8,8)/(9,6) peak. All of this is indicative that the magnetic susceptibility anisotropy of the smaller diameter (6,6) nanotube is higher than the larger diameter (7,7) and other (n, n) nanotubes present in this sample. Colormaps of the absorbance as a function of magnetic field for light parallel (a) and perpendicular (b) are presented in Fig. 4.19.

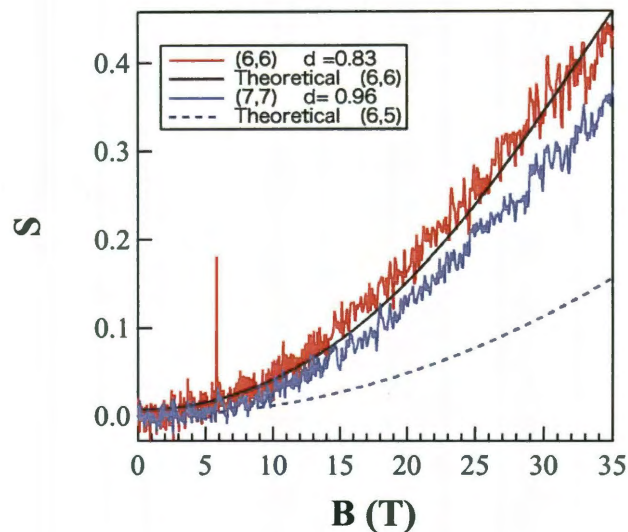


Figure 4.20 : S vs. B of (6,6) vs. (7,7) deduced from magnetic linear dichroism spectroscopy. The smaller diameter metallic (6,6) nanotube (red) has a higher S as a function of B than larger diameter metallic (7,7) nanotube (blue). The black dashed line corresponds to the theoretical curve for (6,6) nanotube and the dashed navy line is for the semiconducting (6,5) nanotube.

We took this data presented in Fig. 4.19, and performed the same analysis proce-

dures as described by Sect. 4.2.1. For the cases of the (8,8) and (9,9) peaks, we were hesitant to make many conclusions until we can perform Raman spectroscopy on this sample in order to know the relative abundances of the non-armchair species. This is not the case for the (7,7) and (8,5) peak in which we are certain by the smaller line width that the contribution of the (8,5) nanotube will be minimal. As such, we will focus the remainder of our discussion on the (6,6) and (7,7) nanotube.

We have S vs. B up to 35 T plotted for the (6,6) and (7,7) nanotube along with the theoretical curves for (6,6) and (6,5) in Fig. 4.20. The $S(B)$ value at 35 T for (6,6) is 0.46 whereas the value for (7,7) is 0.34. Furthermore, the values that we found for (6,6) are also very close to the theoretical curve. Finally, both armchair nanotubes presented in Fig. 4.20 are much higher than the theoretical curve corresponding to the semiconducting (6,5) nanotube.

4.4 Future Work on Magnetic Susceptibility Anisotropy in Metallic Nanotubes

We are presently working with theory developed during our previous work in order to estimate the magnetic susceptibility anisotropy of the (6,6) and (7,7) nanotubes in our diameter dependence study. We also want to perform additional experiments on more metallic species both armchair and non-armchair. Specifically, it would be interesting to compare the effect of chiral angle on the $\Delta\chi$ of metallic nanotubes by investigating chirality-enriched metallic species like (7,4), (8,5), etc. Currently, there

is no method for enriching chiral metallic carbon nanotubes and that would be a crucial step in this investigation. Without this step, the armchair and non-armchair absorbance peaks would have too much overlap in the E_{11} metallic regime and would require complementary resonance Raman spectroscopy data along with complicated fitting routines to gain a meaningful result.

Finally, an interesting experiment would be the temperature dependence of the magnetic susceptibility of metallic carbon nanotubes. As stated in Sect. 4.2.3, the magnetic field dependence of the paramagnetic χ_{\parallel} of metallic nanotubes is a function of magnetic field, temperature, and Fermi energy. At low temperature as the magnetic field increases, the divergence seen in the density of states, which occurs when the Fermi energy comes in agreement with the band edge [89], will cause a significant decrease in the χ_{\parallel} of metallic nanotubes (27% from 0 to 40 T). As a result, it will cause a decrease in overall χ not seen at room temperature. Unfortunately, low temperatures would not allow for our method of magnetic linear dichroism spectroscopy because the magnetic alignment of carbon nanotubes is not possible due to the fact that the solution would freeze below a certain temperature. As such, one would probably have to use a SQUID magnetometer and measure magnetization directly as a function of temperature on a metallic enriched powder sample.

Chapter 5

Light Emission from High Density 1D Excitons

In Chapter 2, we presented excitons as bound electron-hole pairs that dominate the absorption and emission spectra for single-walled carbon nanotubes (SWNTs). The study of excitons has created the framework for the development of new optoelectronic devices from these nanostructure semiconducting materials. In SWNTs, most of the studies on optical properties and excitons have been with weak excitation in quasi-equilibrium regime. The work presented in this section is one of the first attempts looking at the temperature dependence of the emission properties of high density excitons in one dimension.

5.1 Previous work on High Density 1D Excitons in Single-Walled Carbon Nanotubes

5.1.1 Room Temperature Upper Limit of Exciton Density in SWNTs

Although limited, there have been a few studies of optical properties of nanotubes under high photoexcitation specifically looking at exciton-exciton annihilation (EEA) in nanotubes [30–37]. One of them proved that correlated electron hole-pairs, or excitons, are very stable under high photoexcitations [29]. However, it was not until

recently that it was realized that there is an upper limit on the exciton density of SWNTs at room temperature [31, 32]. This is due to the very efficient diffusion-limited exciton-exciton annihilation process under high pump fluences. Namely, immediately after excitation of a high energy laser pulse, excitons created within the diffusion lengths of each other will be “annihilated” non-radiatively, resulting in lower photoluminescence. Experimentally, this is measured thru the intensity of the photoluminescence as a function of pump fluence.

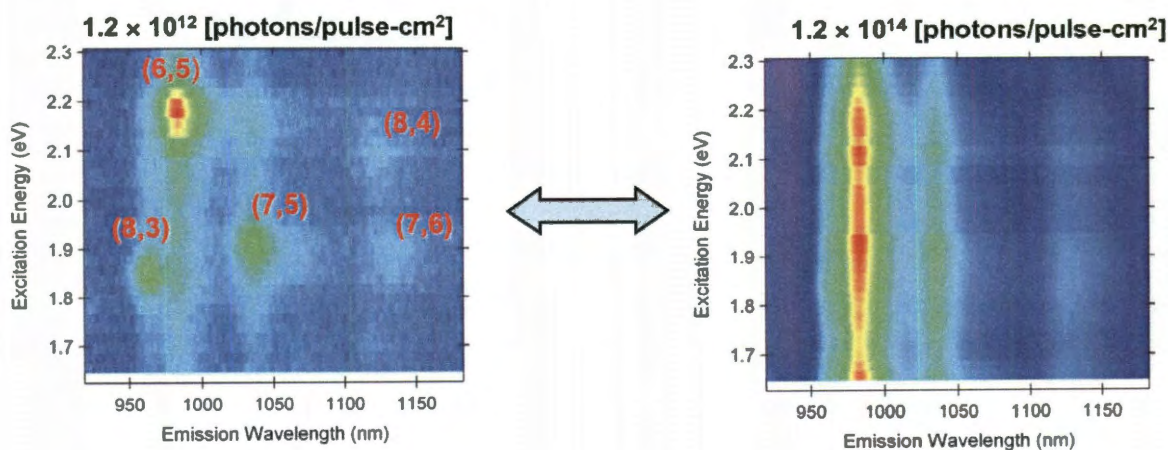


Figure 5.1 : Nonlinear photoluminescence excitation (PLE) spectroscopy of CoMoCAT SWNTs at low (left) and high photoexcitation (right). The low fluence PLE is similar to that of CW PLE but the high excitation PLE shows complete flattening of the excitation spectra [32].

Murakami and Kono performed photoluminescence excitation (PLE) spectroscopy at room temperature on CoMoCAT SWNTs in solution (Fig. 5.1). They discovered that at low fluence the data is similar to linear CW PLE with each “hotspot” corresponding to luminescence at a resonant E_{22} and E_{11} energy for each chirality present

in their sample. As the photoexcitation is increased, the excitation spectrum is observed to gradually flatten, indicating that at high fluence carbon nanotube emission is independent of the excitation energy [31,32].

The authors then estimated the exciton density by comparing the PL versus excitation intensity curves with theoretical curves. As seen in Fig. 5.2, they observed that at high fluence, the PL intensity saturates and for each chirality and excitation wavelength there was a different saturation value corresponding to a certain exciton density. For the (7,5) nanotube under resonant excitation at the highest fluence, this upper limit at room temperature was found to be $1.5 \times 10^5 \text{ cm}^{-1}$, an order of magnitude below the Mott density [31,32].

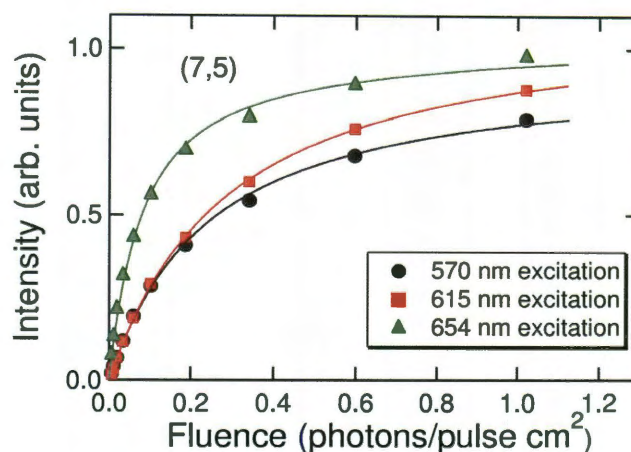


Figure 5.2 : PL Intensity as a function of fluence for the (7,5) nanotube at three different excitation wavelengths. There is a sharp rise at low fluence for the green triangles, or resonant excitation (654 nm). This rise results in a higher saturation value than the other wavelengths shown; 570 nm (black circle) and 615 nm (red squares) . The data is fit to a diffusion-limited exciton-exciton annihilation model described in Subsect. 5.1.2. Adapted from [32].

5.1.2 Diffusion Limited Exciton-Exciton Annihilation Model

After a high-intensity optical pulse is incident on a nanotube, many excitons are created instantaneously. Thermal agitations cause them to make random walks along the nanotube. During these random walks, excitons can only survive if they are created a distance away from each other longer than the diffusion length, l_x . The diffusion length has been estimated to be about 45 nm at room temperature [90]. Within this diffusion limit, when two excitons encounter each other, there is either partial or absolute annihilation through nonradiative processes. If the annihilation is partial and an exciton remains after the time that the pulse hits the nanotube, then when the exciton relaxes it will emit a photon.

To describe their results from this phenomenon, Murakami and Kono employed a *diffusion-limited* EEA model [31]. Their model had two assumptions: 1) when two excitons are within the diffusion limit, EEA happens instantaneously and absolutely (probability of EEA = 1) and 2) the positions of exciton creation happen randomly along the nanotube. In this model, the pump intensity, I_{pump} , is related to the initial exciton density N_0 by $I_{\text{pump}} = c_2\psi$, where c_2 is a scaling factor. Here, ψ , is a dimensionless quantity describing the light intensity. The definition of ψ includes the diffusion length (l_x), the length of the nanotube (L), and the initial exciton density:

$$\psi \equiv \frac{N_0 l_x}{L} \quad (5.1)$$

Similarly, the measured photoluminescence intensity, I_{PL} , is related to the exciton density after EEA (N) by $I_{\text{pump}} = c_1\zeta$, where c_1 is a scaling factor and ζ is the

dimensionless quantity representing the exciton population. This quantity is defined such that:

$$\zeta \equiv \frac{Nl_x}{L} \quad (5.2)$$

where $0 \leq \zeta < 1$. To relate Eqn. (5.2) to Eqn. (5.1), we can utilize the following

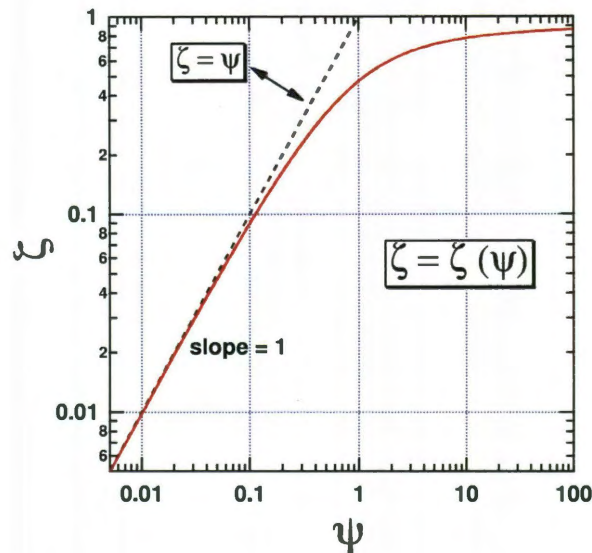


Figure 5.3 : Model function of ζ vs. ψ (red). At low excitation intensity, the slope = 1 representing the CW linear regime. The dashed line corresponds to the model is $\zeta = \psi$.

expression:

$$\psi = \frac{1}{e} \left[\text{Ei} \left(\frac{1}{1 - \zeta} \right) - \text{Ei}(1) \right] \quad (5.3)$$

where e is the transcendental number and $\text{Ei}(x)$ is the exponential integral function [91].

A plot showing the relationship of $\zeta(\psi)$ is plotted in Fig. 5.3. In the low excitation regime, the model has a slope of 1, indicating a linear increase in exciton density as

a function of pump power. This regime also represents the CW steady-state PL experiments. As one increases the photoexcitation, the exciton density begins to saturate and transitions out of the ability to describe steady-state experiments. This indicates the influence of nonradiative EEA processes at higher power. One can utilize the definitions of I_{pump} , I_{PL} , and the scaling factors within this model to extract N for each power saturation curve in data. The point at which each curve completely saturates implies that the exciton density reaches an upper limit. The fits to the data modeled by Eqn. (5.3) for the (7,5) nanotube are seen in Fig. 5.2 where the authors used scaling factors to extract exciton densities from their PL data.

5.1.3 Temperature Dependent Theory of High Density 1D Excitons in Single-Walled Carbon Nanotubes

Srivastava and Kono also investigated exciton-exciton annihilation in SWNTs using time-domain analysis [92]. The authors based their model on diffusion-limited reactions to resolve analytical expressions for the population of both excitons and photons (PL) as a function of time. By including the radiative recombination decay as a Poissonian process in the problem of one-dimensional diffusion-driven two-particle annihilation, they correctly modeled the dynamics of excitons as a function of time with different initial densities. They then compared their results to Monte Carlo simulations to quantitatively explain the existence an upper limit on the exciton density in SWNTs at room temperature as shown by Murakami and Kono (Sect. 5.1.1) [31,32].

As a way to surpass this upper limit on the density of 1D excitons in SWNTs, Srivastava and Kono also investigated the effect of temperature and magnetic field on the EEA process in SWNTs [92]. From Fig. 5.4, it is clear that the diffusion length decreases from 300 K with a \sqrt{T} dependence until it reaches a minimum due to the presence of the $1g$ dark exciton state. The central idea is that, if the diffusion length decreases, then EEA will become less efficient resulting in higher emission from the higher density of 1D excitons.

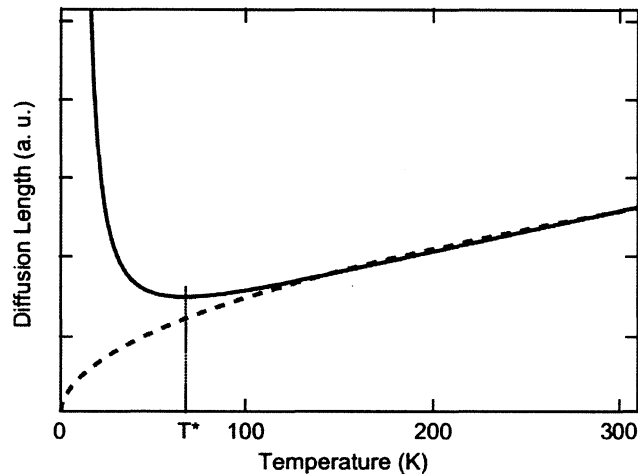


Figure 5.4 : Diffusion length as a function of temperature. T^* denotes a critical temperature at which the diffusion length reaches a minimum and begins to increase to infinity at lower temperature. The dashed line represents the value of the diffusion length if dark excitons were not taken into account. Adapted from Ref. [92].

With the introduction of dark exciton effects, it is theorized that at a critical temperature T^* there would be an increase in diffusion length and a decrease in EEA causing lower photoluminescence under this temperature. The large increase in the diffusion length at low temperatures is a result of the predicted approach to infinity

of the radiative lifetime. It is also important to note that the critical temperature is a function of diameter, local environment, and magnetic field. From this theory that through manipulating exciton density by varying temperature, we predict that we can realize higher exciton density through temperature dependent PL measurements.

5.2 Experimental Methods

5.2.1 Sample 1: HPR 188.1 HiPco Solution

We followed the procedure to produce a solution decant as described by Ref. [9] . Individualization of the SWNTs was achieved by dispersion of raw HiPco nanotube material into 1% sodium deoxycholate (DOC) through bath sonication for 30 minutes. Then, the resulting solution was further sonicated for 17.5 hours at 10°C. Finally, the solution was centrifuged for 1 hour at 208400 g and the top 80% of the solution was extracted, assuming that most of the more dense bundles and pellets are settled in the bottom of the centrifuge tubes. A photoluminescence excitation map of the solution we used is displayed in Fig. 5.5.

5.2.2 Sample 2: HPR 188.1 HiPco Single-Walled Carbon Nanotubes in ι -carrageenan film

For our low temperature studies, we embedded our nanotube solution from Sample 1 (Sect. 5.2.1) into an ι -carrageenan polymer matrix. The use of a polymer host for carbon nanotubes is a common practice for optical spectroscopy, particularly in low

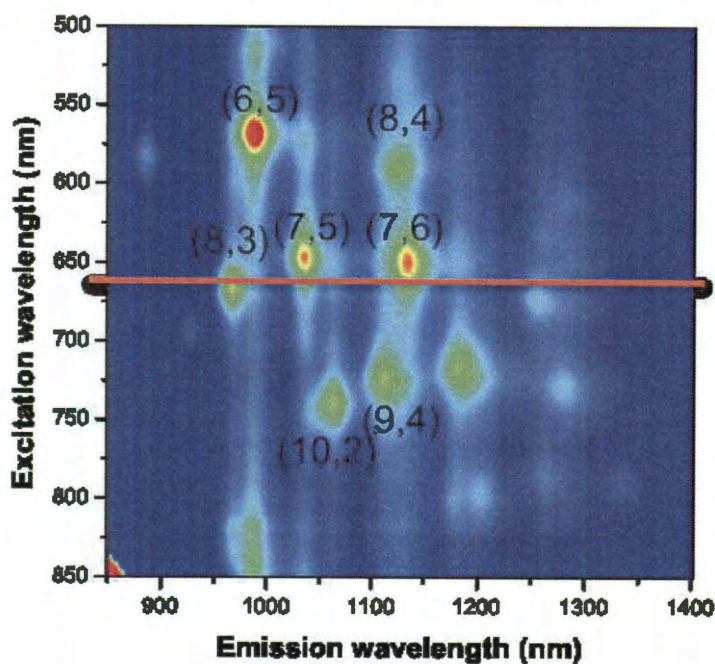


Figure 5.5 : Photoluminescence excitation (PLE) map of HPR 188.1 HiPco solution sample. The red line corresponds to the slice of the excitation wavelength 658 nm for all experiments in Chapter 5. Also note that the (6,5) nanotube is the brightest nanotube in this sample with other small d_t chirality nanotubes present.

temperature and high magnetic field experiments [23, 42, 64]. The particular polymer *ι*-carrageenan, found readily in products such as beer and shampoo, has proven to be transparent through the visible and near-infrared ranges [93].

To achieve this film sample, we employed the following methodology. We prepared

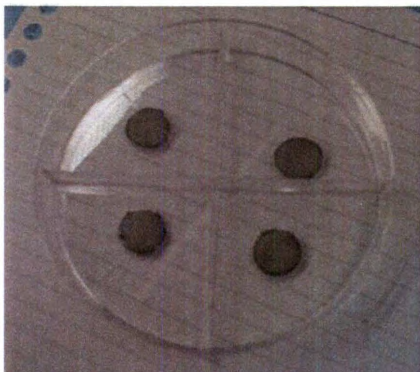


Figure 5.6 : Photograph of four ι -carrageenan films after process described in the text.

1%(wt/vol) ι -carrageenan solution with 1% DOC solution in vial by vortex mixing. We then heated the solution up to 70°C under continuous stirring and maintaining a constant temperature. After turning off the heater and waiting for the solution temperature to drop to 55°C, we placed our SWNT in 1 % DOC solution (from Sect. 5.2.1) and the same volume of carrageenan solution into the vial. Then, we turned back on the heater and kept it at 55°C. We mixed the two solutions by stirring for 10 minutes. We casted the final solution into a teflon mold on plastic sheet for 36 hours. Finally, we gently removed the casted film from the mold with a razor blade. A photograph of our films is presented in Fig. 5.6.

5.2.3 Nonlinear Photoluminescence Spectroscopy Experimental Setup

To create high densities of 1D excitons, we utilized intense 150 fs long pulses from an optical parametric amplifier (OPA) tuned to 658 nm (1.88 eV) to be on resonance with the E_{22} exciton energy of the (7,5) nanotube found in our carbon nanotube

embedded polymer. The OPA was initially pumped by a chirped pulse amplifier (CPA) at a 1 kHz repetition rate. There was a spatial filter in the beam path to ensure the best overall beam quality from the OPA.

In addition to this source, we referenced our spectra with data taken simultaneously with continuous-wave (CW) excitation under similar pump conditions, i.e., spot size, beam quality, beam path, and average power. This was achieved by the introduction of our 658 nm laser diode beam into the OPA beam path through the use of a flipper mirror mount. When wanting to take PL data in the linear excitation regime, we flipped the mirror down, and the laser diode beam was allowed to travel into our main excitation line. When taking high photoexcitation data, the mirror was then flipped up to allow for the OPA beam to travel along the main excitation line.

In the main excitation line, either form of excitation traveled along the same exact path and through the same optics. The first optic was a 658 nm band pass filter that was used to eliminate additional wavelengths from the CPA/OPA photoexcitation. Next, there was a variable neutral density filter to control the excitation power incident on the sample. To make certain that the power was the same, we used a neutral density filter of variable optical density and adjusted this with a calibrated power meter. Also, to ensure normal incidence of the excitation onto the sample, we utilized two additional mirrors. The beam traveled through a focusing lens to the sample. For the room temperature solution studies, the nanotube solution was held in a 1 mm cuvette. For the low temperature studies, the film was placed on the cold

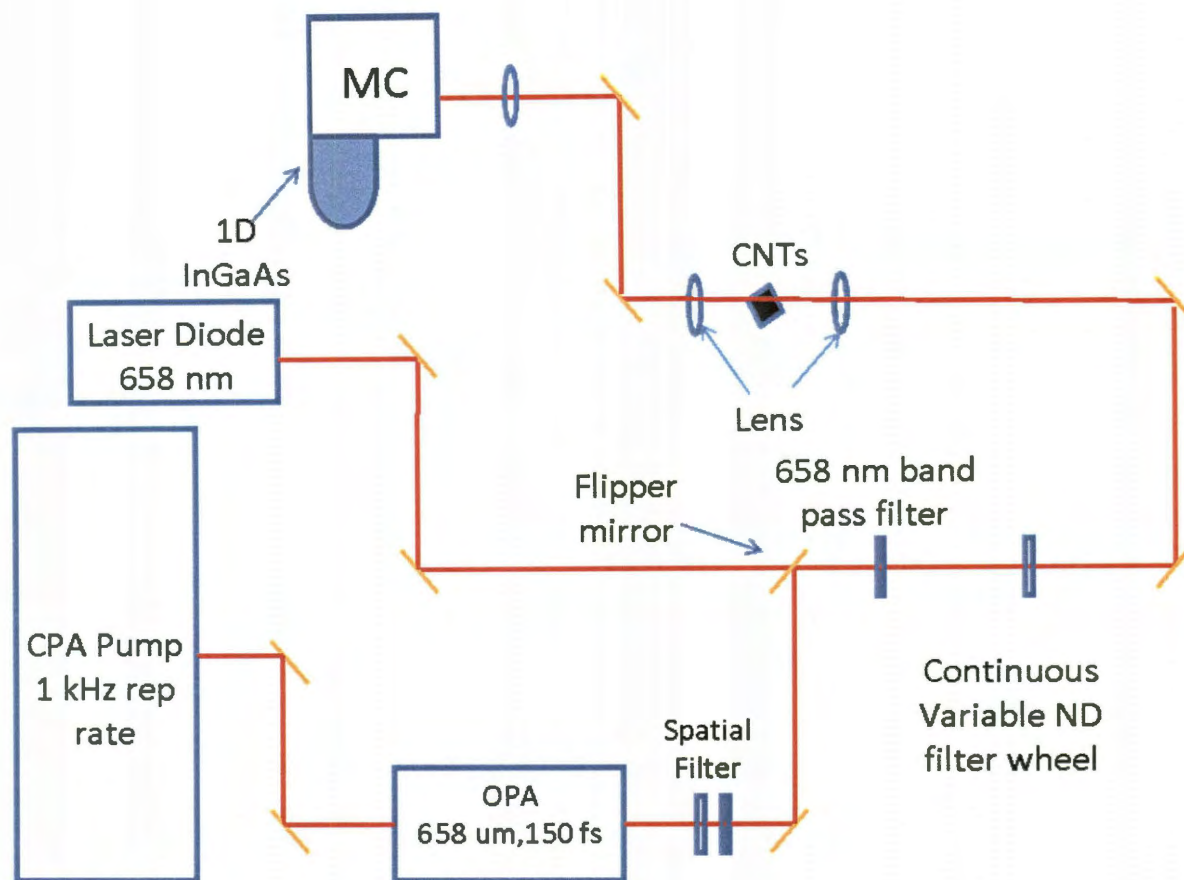


Figure 5.7 : Schematic of experimental setup for nonlinear photoluminescence spectroscopy of HiPco SWNTs. There are two sources of single wavelength excitation, CW from a 658 nm laser diode and high energy pulsed excitation from OPA. The photoluminescence, created by either form of excitation, is collected with a monochromator and detected by an InGaAs 1D camera.

finger of a LHe flow-cryostat.

Photoluminescence is emitted isotropically, but in our case it is collected in transmission. The photoluminescence was collected by a lens, that collimated the PL until it was focused onto the entrance slit of a monochromator. The diffraction grating inside the monochromator (MC) dispersed the PL as a function of wavelength in the

near-infrared and the data was recorded with an InGaAs linear-array detector. The experimental setup is shown as a schematic in Fig. 5.7.

5.3 Results

5.3.1 Room Temperature Results

Before lowering the temperature, we first wanted to study our solution sample over many decades of excitation average powers to reproduce the PL saturation seen at the room temperature by Murakami and Kono [31,32]. Furthermore, we set out to study the difference in PL emission between excitation from the steady-state CW diode and that of high photoexcitation under the same conditions for the first time. Our experimental setup allowed for us to do just that with the use of average powers in this study from 10 nW to 2 mW.

For our study on the solution sample at room temperature, our results shown in Fig. 5.8 indicate that, as we increase the power of the CW diode, we see a linear increase in PL. For the (7,5) nanotubes in our sample, the peak height corresponds to $\sim 7 \times 10^6$ counts per second at 2 mW. Additionally, all chiralities present in this sample seem to increase linearly at their respective rates corresponding to the relative abundance of each carbon nanotube under 658 nm excitation. For the case of high photoexcitation pulses across the same excitation range, at higher powers the data is no longer linear for any chirality nanotubes. It is also important to note that the overall intensity is much lower with the peak height of (7,5) at 2 mW $\sim 1.2 \times 10^4$

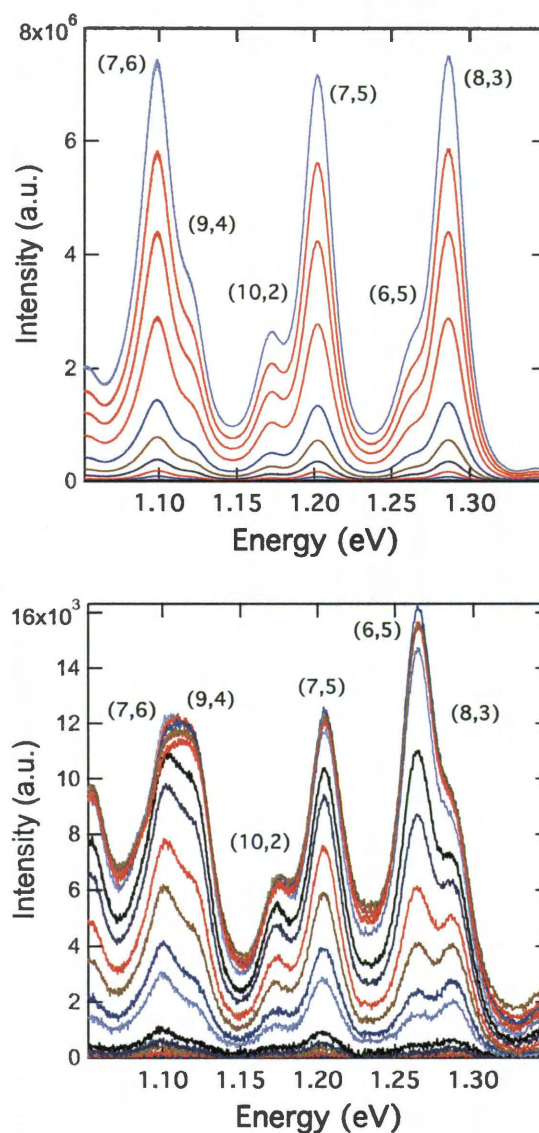


Figure 5.8 : Power dependent PL spectra for Sample 1 solution. The diode excitation (top) scales linearly for each chirality present in the sample. This is in stark contrast to the case of high photoexcitation (bottom). Note that the relative intensities are different from the diode to the OPA cases.

counts per second.

From every spectrum taken, we fit the data using a series of Voigt peaks. The

composition of the peak is a 50% Gaussian and 50% Lorentzian convolution, with each representing a corresponding nanotube feature in the PL spectrum [31, 32, 94]. From each Voigt peak, one can take the peak area as the PL integrated intensity from that particular (n, m) chirality. The integrated peak area for (7,5) as a function of pump power is plotted in Fig. 5.9.

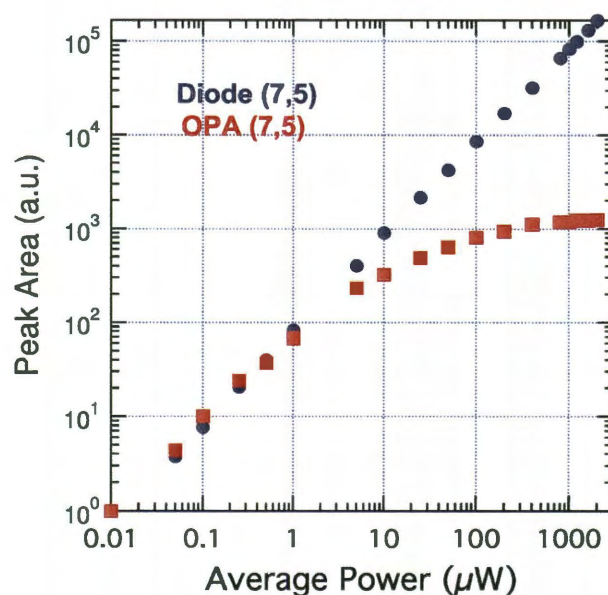


Figure 5.9 : Power dependent PL for (7,5) in HPR solution. The diode excitation (navy) is completely linearly over the entire power range. Conversely, at high photoexcitation (red squares), the PL from OPA excitation saturates at high fluence. The saturation corresponds to the upper limit on exciton density at room temperature.

At room temperature, the data points from the OPA excitation increase linearly as a function of pump power until you reach a regime in which the PL signal saturates at higher fluence. In contrast, for the case of diode excitation, the PL signal keeps increasing linearly with higher pump power. The deviation seen in nonlinear PL is a

direct result of the exciton-exciton annihilation at room temperature.

5.3.2 Temperature Dependent Results

At room temperature in solution, we found that for the (7,5) nanotube for the case of diode excitation, the PL increased linearly with higher pump power. However under high photoexcitation, due to the highly efficient EEA process, as seen previously in Ref. [31, 32], there was a saturation value corresponding to the existence of an upper limit on exciton density at room temperature. Therefore, we embedded our solution into an ι -carrageenan matrix and performed temperature dependent PL measurements from 15 to 295 K. The power range in this investigation was from 10 μ W to 2 mW because the overall PL efficiency of SWNTs decreased after being embedded into a polymer matrix [95]. In other words, there was little PL measured below 10 μ W although it is expected to increase linearly with increasing pump power. Furthermore, depending on the environment imposed by the matrix there has been reported slight peak shifts, broadening, and even quenching due to the process of embedded nanotubes into polymers.

Our PL results at 15 K for the diode and high excitation cases are presented in Fig. 5.10. Note that each trace actually represents two PL spectra taken at separate times and the temperature was varied in a random fashion. This confirms that there was no heating that occurred during our experiment and the results were repeatable. Also note that as with the room temperature spectra (Sect. 5.3.1), the relative in-

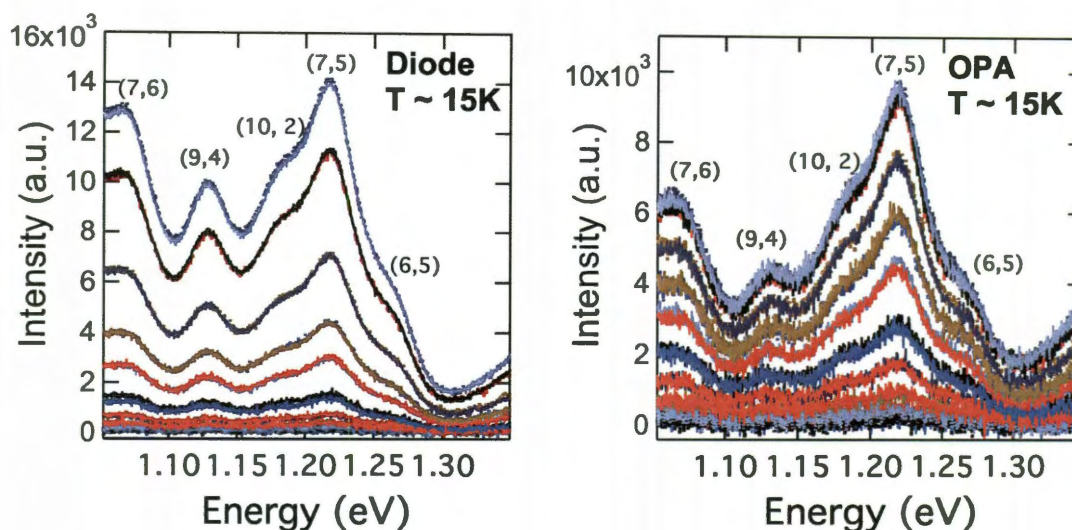


Figure 5.10 : Power dependent PL spectra for HPR SWNTs embedded in polymer matrix at 15 K. The diode excitation (left) is linear up to 2 mW maximum average power. At high photoexcitation (right), PL from OPA excitation saturates at high powers. Both data are fit to extract peak areas as a function of power plots.

tensities of the chiralities are different for each case (CW or high photoexcitation). Also, the spectra from high photoexcitation look to be saturating at higher pump intensities.

From every spectrum taken in our temperature dependent study, we fit the data using a series of Voigt peaks just as in Sect. 5.3.1. From each peak area, we were able to compare the PL intensity vs. average pump power for each temperature taken in our range. At 295 K, just as in the case of the solution at room temperature, at higher pump fluences the diode data was completely linear, and in the high photoexcitation case there was a saturation indicating exciton-exciton annihilation. As we decreased the temperature, there was a decrease in the separation from the linear and nonlinear

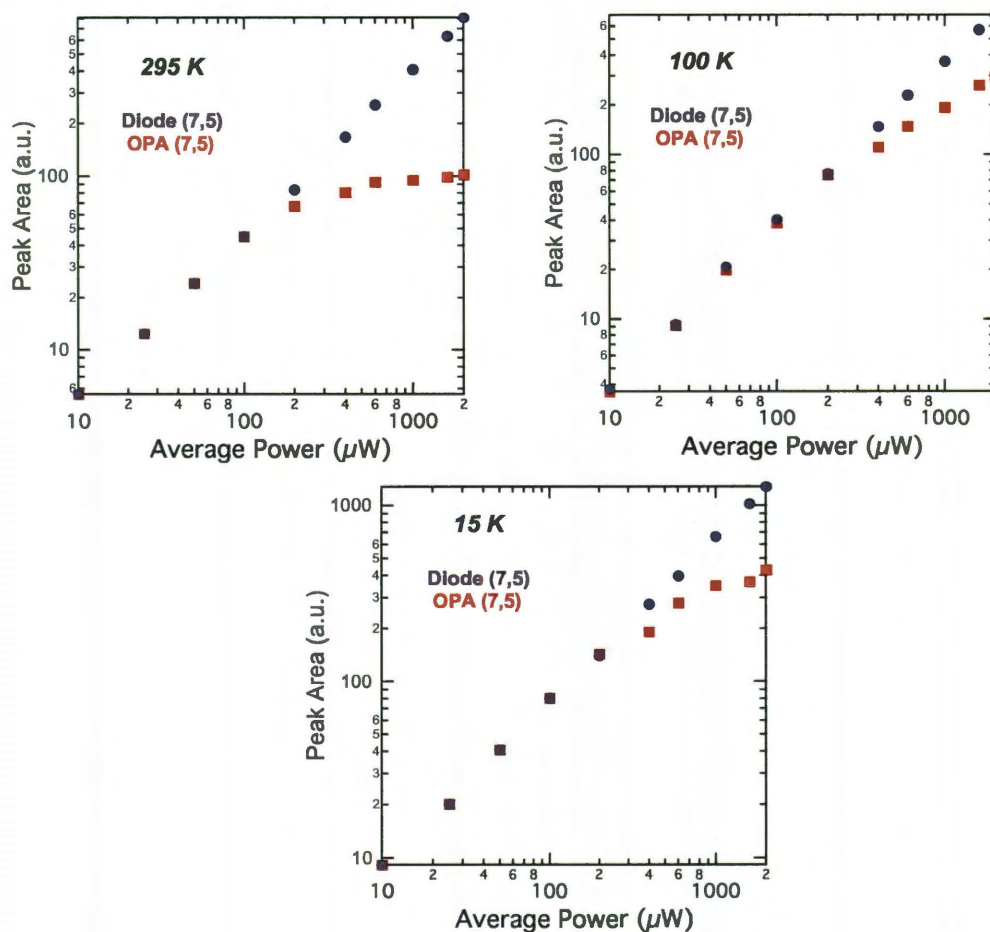


Figure 5.11 : Power dependent PL as a function of pump power for HPR SWNTs embedded in polymer matrix at 295, 100, and 15 K. The separation of between two traces of each at higher power indicates the efficiency of the EEA process at that temperature.

plots in the power dependent spectra down to 100 K. After that temperature, we saw that the separation began to increase again at lower temperatures. This is indicative of the predicted temperature dependence of the EEA efficiency from Sect. 5.1.3. Fig-

ure 5.11 shows representative power dependence plots for (7,5) at three temperatures taken in our study (295 K, 100 K, and 15 K).

5.4 Analysis

Using our model of diffusion-limited exciton-exciton annihilation (Sect. 5.1.2), we were able to extract estimates of the exciton density at several temperatures. According to our results, the largest density at 100 K was $2.7 \times 10^5 \text{ cm}^{-1}$, still an order of magnitude lower than the predicted Mott density in SWNTs. However it is important to note that, by analyzing our data in this manner, it does not take into account the temperature dependence of excitons even seen in the linear regime [23,42].

This is the very impact of the manner in which we took this data because each power dependent plot represented by Fig. 5.11 allows for us to gain new information about the emission properties of SWNTs in the context of the temperature dependent relative photoluminescence (PL) efficiency. Due to both sets of data being taken at the same temperature under similar pumping conditions (spot size, beam quality, beam path, average power), we can determine for the first time the contribution from the nonradiative rate of the exciton-exciton annihilation process, γ_{xx} as a function of temperature and excitation power.

We first begin with the measured data for the diode and high photoexcitation cases at each temperature, which is I_{PL} as a function of I_{pump} . The measured I_{PL} is

a function of the PL efficiency of our experimental setup such that:

$$I_{PL} = \alpha \eta_T I_{\text{pump}} \quad (5.4)$$

where α is the instrumental response constant and η_T is the temperature-dependent relative PL efficiency. For the case of linear CW excitation, the relative PL efficiency is not dependent on the pump intensity, and therefore, it is represented by $\eta_{T,CW}$. This is not the case for OPA excitation, for which the relative PL efficiency depends on the pump intensity, i.e., $\eta_{T,NL}(I_{\text{pump}})$.

This comes from the fact that there is an additional intensity dependent term due to EEA in the formal definition of $\eta_{T,NL}(I_{\text{pump}})$:

$$\eta_{T,CW} \equiv \frac{\gamma_r}{\gamma_r + \gamma_{nr}} = \frac{\gamma_r}{\Gamma_0} \quad (5.5)$$

$$\eta_{T,NL}(I_{\text{pump}}) \equiv \frac{\gamma_r}{\gamma_r + \gamma_{nr} + \gamma_{xx}(I_{\text{pump}})} = \frac{\gamma_r}{\Gamma_0 + \gamma_{xx}(I_{\text{pump}})} \quad (5.6)$$

In the above equations, γ_r is the radiative decay rate, γ_{nr} is the nonradiative decay rate without including EEA, Γ_0 is the total decay rate in the absence of EEA, and γ_{xx} is the nonradiative decay rate due to exciton-exciton annihilation processes.

So what we want to determine is γ_{xx} as a function of T and I_{pump} from our current data. At a constant temperature, we can utilize Eqn. (5.4) to relate to our data:

$$\frac{I_{PL,NL}}{I_{PL,CW}} = \frac{\eta_{NL}(I_{\text{pump}})}{\eta_{CW}} \quad (5.7)$$

Next if we divide Eqn. (5.6) by Eqn. (5.5), then we are able to solve for γ_{xx} from the following:

$$\frac{I_{PL,NL}}{I_{PL,CW}} = \frac{\Gamma_0}{\Gamma_0 + \gamma_{xx}(I_{\text{pump}})} \implies \gamma_{xx}(I_{\text{pump}}) = \Gamma_0 \left(\frac{I_{PL,CW}}{I_{PL,NL}} - 1 \right) \quad (5.8)$$

5.5 Discussion

Now we are in a position to determine γ_{xx} as a function of pump intensity and temperature. At room temperature, we can find the ratio of the relative PL efficiency for each particular chirality by plotting the ratio of $I_{PL,NL}$ and $I_{PL,CW}$ vs. I_{pump} . This data can then be used to plot γ_{xx}/Γ_0 from Eqn. (5.8). These plots for the (7,5) nanotube at 295 K are shown in Fig. 5.12.

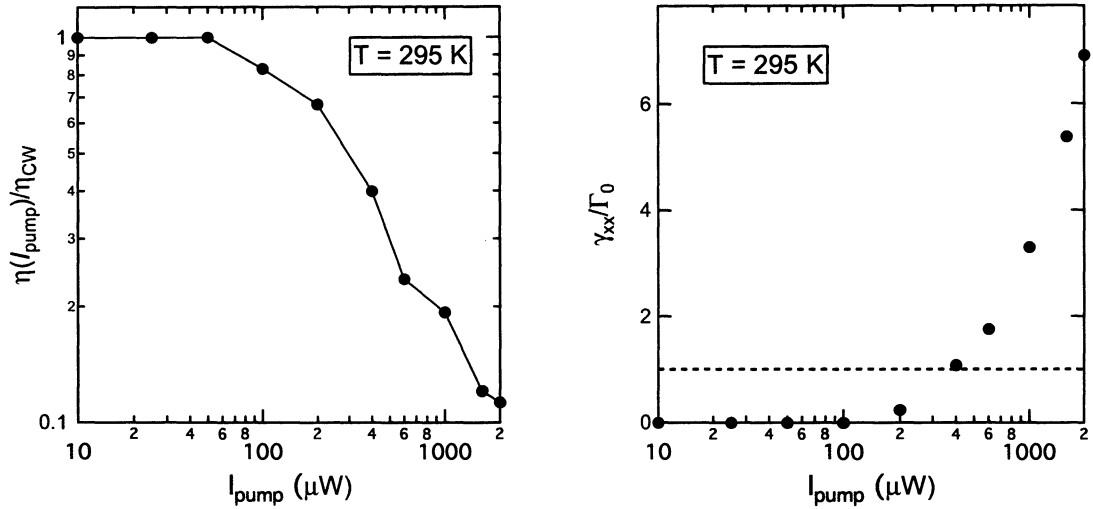


Figure 5.12 : Normalized relative quantum efficiency for (7,5) at room temperature (left). The normalized nonradiative rate γ_{xx}/Γ_0 for (7,5) nanotube at 295 K (right). The dashed line corresponds to the line where $\gamma_{xx} = \Gamma_0$.

If we utilize this same method for the other temperatures taken in our experiment, we can then find γ_{xx}/Γ_0 as a function of temperature and pump intensity. For the (7,5) chirality at the highest pump intensity, we found $\gamma_{xx} \sim 7 \Gamma_0$ for room tempera-

ture. From our current experimental methods, no estimate can be drawn on the true absolute value for Γ_0 . Nonetheless, estimates for Γ_0 range from 10 – 300 ps⁻¹ at room temperature [33–35]. As the temperature decreases from 300 K to 125 K, the ratio of γ_{xx}/Γ_0 also decreases in Fig. 5.13. This indicates that not only the diffusion length is increasing, as predicted, but also that the PL efficiency reaches an optimum value at around 125 K for (7,5). This is the temperature at which the nonradiative radiative decay rate due to exciton-exciton annihilation is least ($\gamma_{xx} \sim 1.17 \Gamma_0$ at the highest excitation power). Therefore, the density of excitons at this temperature is also at a maximum.

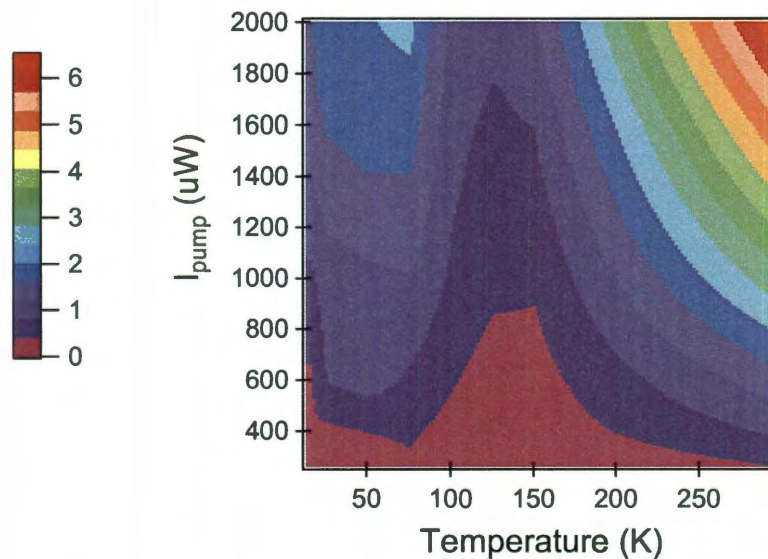


Figure 5.13 : The normalized nonradiative rate γ_{xx}/Γ_0 for (7,5) nanotube vs. temperature and excitation power from 295 K to 15 K. γ_{xx}/Γ_0 decreases until it reaches a minimum at 100 K - 150 K.

After this temperature, the values for γ_{xx}/Γ_0 begin to increase again indicating that nonradiative decay rate for exciton-exciton annihilation is increasing up to 50 K. After 50K, the ratio begins to decrease again (Fig. 5.13). γ_{xx} at temperatures less than 75 K in this study all are in the $1.7 - 2.4 \Gamma_0$ range at the highest power. The second decrease can be attributed to changes in the time-dependence of the exciton population at low temperatures [92].

In the context of photonic devices, where light is the primary medium of sending signals through emission, transmission, amplification etc., carbon nanotubes absorb light in the visible and emit in the near-infrared/telecom frequencies dependent on their diameter-dependent bandgap. As a result, nanotubes are of interest for applications in photonics on the nanoscale. The largest obstacle in the applications of carbon nanotubes as photonic devices has been the low quantum efficiency at room temperature. This is this case for the saturation of photoluminescence at high excitation and high temperature. In relation to the results of this work, we have shown that potential photonic devices can operate at an optimum temperature, higher than that of liquid nitrogen temperatures. The nonradiative decay due to EEA can be decreased and in turn the amount of light absorbed and in our case emitted can be increased through an increase in the relative quantum efficiency.

5.6 Future Work

In this chapter, we showed that the nonradiative decay rate due to EEA is decreased from $\sim 7 \Gamma_0$ at room temperature to $\sim 1.17 \Gamma_0$ at 125 K and the highest intensity, where Γ_0 is the total decay rate without the inclusion of exciton-exciton annihilation. Below this temperature, there is decrease in diffusion length and an increase in exciton density. As a way to further investigate the decrease in the efficiency of EEA and increase the density of excitons, we propose to apply our experimental methods inside a magnetic field.

As shown in Sect. 5.1.3 and shown experimentally in this chapter, the diffusion length continues to decrease as a function of temperature until it reaches a minimum and then the diffusion length begins to increase again. Experimentally, we saw that the photoluminescence intensity began to decrease after reaching a moderate temperature (100-125 K). This is a direct consequence of the effect of dark excitons. If we do not take into account dark exciton effects, then the diffusion length is expected to continue to decrease as a function of temperature. From our theory of magnetic brightening (Sect. 3.2.2) and previous single nanotube magneto-PL experiments, we show that the dark exciton state becomes bright at finite B . Therefore, at high B and low temperature, the density of excitons should be able to achieve close to the Mott Density.

Chapter 6

Conclusion

In conclusion, we have successfully presented the magnetic susceptibility, $\Delta\chi$, for metallic single-walled carbon nanotubes and confirmed that they are much larger than those of semiconducting nanotubes as predicted. We also compared magnetic susceptibilities of semiconducting and metallic nanotubes of the same sample experimentally. Lastly, we were able to confirm previous experimental results for the chirality dependence of the magnetic susceptibility anisotropy in semiconducting nanotubes and found that this is also true for metallic nanotubes.

Furthermore, we performed temperature dependent PL on SWNTs in a polymer film under high photoexcitation. We found that the nonradiative decay rate for exciton-exciton annihilation decreases from 300 K to 125 K for the (7,5) nanotube indicating an increase in the maximum allowed density for nanotubes around that temperature. This work is promising for applications in nanotube optoelectronics.

Bibliography

- [1] C. V. Raman, “Diamagnetism and Crystal Structure,” *Nature*, vol. 123, no. 3112, p. 945, 1929.
- [2] R. C. Haddon, “Magnetism of the carbon allotropes,” *Nature*, vol. 378, pp. 249–255, 1995.
- [3] M. S. Dresselhaus, G. Dresselhaus, and P. Avouris, eds., *Carbon Nanotubes: Synthesis, Structure, Properties, and Applications*. Springer, 2001.
- [4] C. Kittel, *Intro to Solid State Physics*. Wiley Scientific, 8th ed., 2005.
- [5] T. Ando, “Theory of electronic states and optical absorption in carbon nanotubes,” *Proceedings of Optoelectronics: Physics and Simulation of Optoelectronic Devices XII*, 2004.
- [6] I. Bozovic, N. Bozovic, and M. Damnjanovic, “Optical dichroism in nanotubes,” *Phys. Rev. B*, vol. 62, pp. 6971–6974, Sep 2000.
- [7] S. Uryu and T. Ando, “Exciton absorption of perpendicularly polarized light in carbon nanotubes,” *Phys. Rev. B*, vol. 74, p. 155411, Oct 2006.
- [8] H. Ajiki and T. Ando, “Aharonov-Bohm effect in carbon nanotubes,” *Physica*

- B*, vol. 201, pp. 349–352, 1994.
- [9] M. J. O. Connell, S. M. Bachilo, C. B. Huffman, V. C. Moore, E. H. Haroz, K. L. Rialon, P. J. Boul, W. H. Noon, C. Kittrell, J. Ma, R. H. Hauge, R. B. Weisman, and R. E. Smalley, “Band-Gap Fluorescence from Individual Single-Walled Carbon Nanotubes,” *Science*, vol. 297, p. 593, 2002.
- [10] S. M. Bachilo, M. S. Strano, C. Kittrell, R. H. Hauge, R. E. Smalley, and R. B. Weisman, “Structure-Assigned Optical Spectra of Single-Walled Carbon Nanotubes,” *Science*, vol. 298, p. 2361, 2002.
- [11] D. S. Chemla and D. A. B. Miller, “Room-temperature excitonic nonlinear-optical effects in semiconductor quantum-well structures,” *J. Opt. Soc. Am. B*, vol. 2, pp. 1155–1173, Jul 1985.
- [12] R. Loudon, “One-dimensional hydrogen atom,” *American Journal of Physics*, vol. 27, no. 9, pp. 649–655, 1959.
- [13] D. S. Citrin, “Long intrinsic radiative lifetimes of excitons in quantum wires,” *Phys. Rev. Lett.*, vol. 69, pp. 3393–3396, Dec 1992.
- [14] T. Ogawa and T. Takagahara, “Optical absorption and sommerfeld factors of one-dimensional semiconductors: An exact treatment of excitonic effects,” *Phys. Rev. B*, vol. 44, pp. 8138–8156, Oct 1991.
- [15] T. Ogawa and T. Takagahara, “Interband absorption spectra and sommerfeld fac-

- tors of a one-dimensional electron-hole system,” *Phys. Rev. B*, vol. 43, pp. 14325–14328, Jun 1991.
- [16] A. Ruini, M. J. Caldas, G. Bussi, and E. Molinari, “Solid state effects on exciton states and optical properties of ppv,” *Phys. Rev. Lett.*, vol. 88, p. 206403, May 2002.
- [17] F. Rossi and E. Molinari, “Coulomb-induced suppression of band-edge singularities in the optical spectra of realistic quantum-wire structures,” *Phys. Rev. Lett.*, vol. 76, pp. 3642–3645, May 1996.
- [18] M. S. Dresselhaus, G. Dresselhaus, R. Saito, and A. Jorio, “Exciton photophysics of carbon nanotubes,” *Annual Review of Physical Chemistry*, vol. 58, no. 1, pp. 719–747, 2007.
- [19] C. D. Spataru, S. Ismail-Beigi, L. X. Benedict, and S. G. Louie, “Excitonic effects and optical spectra of single-walled carbon nanotubes,” *Phys. Rev. Lett.*, vol. 92, p. 077402, Feb 2004.
- [20] C. D. Spataru, S. Ismail-Beigi, R. B. Capaz, and S. G. Louie, “Theory and *Ab Initio* calculation of radiative lifetime of excitons in semiconducting carbon nanotubes,” *Phys. Rev. Lett.*, vol. 95, p. 247402, Dec 2005.
- [21] J. Maultzsch, R. Pomraenke, S. Reich, E. Chang, D. Prezzi, A. Ruini, E. Molinari, M. S. Strano, C. Thomsen, and C. Lienau, “Exciton binding energies in

- carbon nanotubes from two-photon photoluminescence,” *Phys. Rev. B*, vol. 72, p. 241402, Dec 2005.
- [22] F. Wang, G. Dukovic, L. E. Brus, and T. F. Heinz, “The optical resonances in carbon nanotubes arise from excitons,” *Science*, vol. 308, no. 5723, pp. 838–841, 2005.
- [23] J. Shaver and J. Kono, “Temperature-dependent magneto-photoluminescence spectroscopy of carbon nanotubes: evidence for dark excitons,” *Laser and Photonics Review*, vol. 1, p. 260, 2007.
- [24] T. Ando, “Excitons in Carbon Nanotubes,” *Journal of the Physical Society of Japan*, vol. 66, no. 4, pp. 1066–1073, 1997.
- [25] T. Ando and S. Uryu, “Theory of excitons in carbon nanotubes,” *physica status solidi (c)*, vol. 6, no. 1, pp. 173–180, 2009.
- [26] T. Ando, “Effects of Valley Mixing and Exchange on Excitons in Carbon Nanotubes with Aharonov–Bohm Flux,” *J. Phys. Soc. Jpn.*, vol. 75, no. 2, p. 024707, 2006.
- [27] L. Luer, S. Hoseinkhani, D. Polli, J. Crochet, T. Hertel, and G. Lanzani, “Size and mobility of excitons in (6, 5) carbon nanotubes,” *Nat Phys*, vol. 5, pp. 54–58, 01 2009.
- [28] S. Wang, M. Khafizov, X. Tu, M. Zheng, and T. D. Krauss, “Multiple exci-

- ton generation in single-walled carbon nanotubes,” *Nano Letters*, vol. 10, no. 7, pp. 2381–2386, 2010.
- [29] G. N. Ostojic, S. Zaric, J. Kono, V. C. Moore, R. H. Hauge, and R. E. Smalley, “Stability of High-Density One Dimensional Excitons in Carbon Nanotubes under High Laser Excitation,” *Phys. Rev. Lett.*, vol. 94, p. 097401, 2005.
- [30] L. Valkunas, Y.-Z. Ma, and G. R. Fleming, “Exciton-exciton annihilation in single-walled carbon nanotubes,” *Phys. Rev. B*, vol. 73, p. 115432, Mar 2006.
- [31] Y. Murakami and J. Kono, “Existence of an Upper Limit on the Density of Excitons in Carbon Nanotubes by Diffusion-Limited Exciton-Exciton Annihilation: Experiment and Theory,” *Phys. Rev. B*, vol. 80, p. 035432, 2009.
- [32] Y. Murakami and J. Kono, “Nonlinear Photoluminescence Excitation Spectroscopy of Carbon Nanotubes: Exploring the Upper Density Limit on One-Dimensional Excitons,” *Phys. Rev. Lett.*, vol. 102, p. 037401, 2009.
- [33] S. Moritsubo, T. Murai, T. Shimada, Y. Murakami, S. Chiashi, S. Maruyama, and Y. K. Kato, “Exciton Diffusion in Air-Suspended Single-Walled Carbon Nanotubes,” *Phys. Rev. Lett.*, vol. 104, p. 247402, 2010.
- [34] A. Hagen, M. Steiner, M. B. Raschke, C. Lienau, T. Hertel, H. Qian, A. J. Meixner, and A. Hartschuch, “Exponential Decay Lifetimes of Excitons in Individual Single-Walled Carbon Nanotubes,” *Phys. Rev. Lett.*, vol. 95, p. 197401, 2005.

- [35] Y. F. Xiao, T. Q. Nhan, M. W. B. Wilson, and J. M. Fraser, "Saturation of the Photoluminescence at Few-Exciton Levels in a Single-Walled Carbon Nanotube under Ultrafast Excitation," *Phys. Rev. Lett.*, vol. 104, p. 017401, 2010.
- [36] T. Hertel, V. Perebeinos, J. Crochet, K. Arnold, M. Kappes, and P. Avouris, "Intersubband decay of 1-d exciton resonances in carbon nanotubes," *Nano Lett.*, vol. 8, no. 1, pp. 87–91, 2008.
- [37] Y.-Z. Ma, L. Valkunas, S. L. Dexheimer, S. M. Bachilo, and G. R. Fleming, "Femtosecond spectroscopy of optical excitations in single-walled carbon nanotubes: Evidence for exciton-exciton annihilation," *Phys. Rev. Lett.*, vol. 94, p. 157402, Apr 2005.
- [38] V. Perebeinos, J. Tersoff, and P. Avouris, "Radiative lifetime of excitons in carbon nanotubes," *Nano Letters*, vol. 5, no. 12, pp. 2495–2499, 2005.
- [39] T. Liu and Z. Xiao, "Exact and closed form solutions for the quantum yield, exciton diffusion length, and lifetime to reveal the universal behaviors of the photoluminescence of defective single-walled carbon nanotubes," *The Journal of Physical Chemistry C*, vol. 115, no. 34, pp. 16920–16927, 2011.
- [40] F. Wang, G. Dukovic, L. E. Brus, and T. F. Heinz, "Time-resolved fluorescence of carbon nanotubes and its implication for radiative lifetimes," *Phys. Rev. Lett.*, vol. 92, p. 177401, Apr 2004.

- [41] T. Gokus, A. Hartschuh, H. Harutyunyan, M. Allegrini, F. Henrich, M. Kappes, A. A. Green, M. C. Hersam, P. T. Araujo, and A. Jorio, "Exciton decay dynamics in individual carbon nanotubes at room temperature," *Applied Physics Letters*, vol. 92, no. 15, p. 153116, 2008.
- [42] S. Berger, C. Voisin, G. Cassabois, C. Delalande, and P. Roussignol, "Temperature Dependence of Exciton Recombination in Semiconducting Single-Wall Carbon Nanotubes," *Nano Lett.*, vol. 7, p. 398, 2007.
- [43] J. Shaver, J. Kono, O. Portugall, V. Krstic, G. L. Rikken, Y. Miyauchi, S. Maruyama, and V. Perebeinos, "Magnetic Brightening of Carbon Nanotubes Photoluminescence through Symmetry Breaking," *Nano Lett.*, vol. 7, no. 7, pp. 1851–1855, 2007.
- [44] I. B. Mortimer, L. J. Li, R. A. Taylor, G. L. Rikken, O. Portugall, and R. J. Nicholas, "Magneto-optical studies of single-wall carbon nanotubes," *Phys. Rev. B*, vol. 76, pp. 085404–1 – 085404–9, 2007.
- [45] D. A. Tsyboulski, J. R. Rocha, S. M. Bachilo, L. Cognet, and R. B. Weisman, "Structure-Dependent Fluorescence Efficiencies of Individual Single-Walled Carbon Nanotubes," *Nano Lett.*, vol. 7, p. 3080, 2007.
- [46] L. J. Carlson, S. E. Maccagnano, M. Zheng, J. Silcox, and T. D. Krauss, "Fluorescence efficiency of individual carbon nanotubes," *Nano Letters*, vol. 7, no. 12, pp. 3698–3703, 2007.

- [47] K. Honda, “Die thermomagnetischen Eigenschaften der Elemente,” *Ann. d. Physik*, vol. 32, no. 1027, 1910.
- [48] M. Owen, “Magnetochemische Untersuchungen. Die thermomagnetischen Eigenschaften der Elemente. II,” *Ann. d. Physik*, vol. 37, p. 657, 1912.
- [49] M. Sepioni, R. R. Nair, S. Rablen, J. Narayanan, F. Tuna, R. Winpenny, A. K. Geim, and I. V. Grigorieva, “Limits on Intrinsic Magnetism in Graphene,” *Phys. Rev. Lett.*, vol. 105, p. 207205, 2010.
- [50] J. W. S. Hummers and R. E. Offeman, “Preparation of Graphitic Oxide,” *J. Am. Chem. Soc.*, vol. 80, no. 6, pp. 1339–1339, 1958.
- [51] K. Wakabayashi, M. Fujita, H. Ajiki, and M. Sigrist, “Electronic and magnetic properties of nanographite ribbons,” *Phys. Rev. B*, vol. 59, no. 12, pp. 8271–8282, 1999.
- [52] H. W. Kroto, J. R. Heath, S. C. O’Brien, R. F. Curl, and R. E. Smalley, “C₆₀: Buckminsterfullerene,” *Nature*, vol. 318, pp. 162–163, 1985.
- [53] S. Iijima and T. Ichihashi, “Single-shell carbon nanotubes of 1-nm diameter,” *Nature*, vol. 363, pp. 603–605, 1993.
- [54] D. S. Bethune, C. H. Kiang, M. S. deVries, G. Gorman, R. Savoy, J. Vazquez, and R. Beyers, “Cobalt-catalysed growth of carbon nanotubes with single-atomic-layer walls,” *Nature*, vol. 363, pp. 605–607, 1993.

- [55] A. P. Ramirez, R. C. Haddon, O. Zhou, R. M. Fleming, J. Zhang, S. M. McClure, and R. E. Smalley, "Magnetic Susceptibility of Molecular Carbon: Nanotubes and Fullerite," *Science*, vol. 265, pp. 84–86, 1994.
- [56] R. S. Ruoff, D. Beach, J. Cuomo, T. McGuire, R. L. Whetten, and F. Diederich, "Confirmation of a Vanishingly Small Ring-Current Magnetic Susceptibility of Icosahedral C₆₀," *J. Phys. Chem.*, vol. 95, no. 9, pp. 3457–3459, 1991.
- [57] Y. Aharonov and D. Bohm, "Significance of Electromagnetic Potentials in the Quantum Theory," *Phys. Rev.*, vol. 115, p. 485, 1959.
- [58] Y. Aharonov and D. Bohm, "Further Considerations on Electromagnetic Potentials in the Quantum Theory," *Phys. Rev.*, vol. 123, p. 1511, 1961.
- [59] H. Ajiki and T. Ando, "Magnetic properties of carbon nanotubes," *J. Phys. Soc. Jpn.*, vol. 62, pp. 2470 – 2480, 1993.
- [60] J. Kono and S. Roche, "Magnetic properties," in *Carbon Nanotubes: Properties and Applications* (M. J. O. Connell, ed.), ch. 5, pp. 119–151, Boca Raton: CRC Press, Taylor & Francis Group, 2006.
- [61] S. Zaric, G. N. Ostojic, J. Kono, J. Shaver, V. C. Moore, M. S. Strano, R. H. Hauge, R. E. Smalley, and X. Wei, "Optical Signatures of the Aharonov-Bohm Phase in Single-Walled Carbon Nanotubes," *Science*, vol. 304, pp. 1129–1131, 2004.

- [62] B. L. Brandt, S. Hannahs, H. J. Schneider-Muntau, G. Boebinger, and N. S. Sullivan, "The national high magnetic field laboratory," *Physica B*, vol. 294-295, pp. 505–511, 2001.
- [63] S. Zaric, G. N. Ostojic, J. Shaver, J. Kono, O. Portugall, P. H. Frings, G. L. Rikken, M. Furis, S. A. Crooker, X. Wei, V. C. Moore, R. H. Hauge, and R. E. Smalley, "Excitons in Carbon Nanotubes with Broken Time-Reversal symmetry," *Phys. Rev. Lett.*, vol. 96, pp. 016406–1, 2006.
- [64] J. Shaver, S. A. Crooker, J. A. Fagan, E. K. Hobbie, N. Ubrig, O. Portugall, V. Perebeinos, P. Avouris, and J. Kono, "Magneto-optical spectroscopy of highly aligned carbon nanotubes," *Phys. Rev. B*, vol. 78, p. 081402(R), 2008.
- [65] A. Srivastava, H. Htoon, V. I. Klimov, and J. Kono, "Direct Observation of Dark Excitons in Individual Carbon Nanotubes: Inhomogeneity in the Exchange Splitting," *Phys. Rev. Lett.*, vol. 101, pp. 087402–1 – 087402–4, 2008.
- [66] H. Ajiki and T. Ando, "Magnetic properties of ensembles of carbon nanotubes," *J. Phys. Soc. Jpn.*, vol. 64, p. 4382, 1995.
- [67] J. P. Lu, "Novel magnetic properties of carbon nanotubes," *Phys. Rev. Lett.*, vol. 74, pp. 1123–1126, 1995.
- [68] M. Fujiwara, E. Oki, M. Hamada, and Y. Tanimoto, "Magnetic Orientation and Magnetic Properties of a Single Carbon Nanotube," *J. Phys. Chem. A*, vol. 105, no. 18, p. 4383, 2001.

- [69] D. A. Walters, M. J. Casavant, X. C. Qin, C. B. Huffman, P. J. Boul, L. M. Ericson, E. H. Haroz, M. J. O. Connell, K. Smith, D. T. Colbert, and R. E. Smalley, "In-plane-aligned membranes of carbon nanotubes," *Chem. Phys. Lett.*, vol. 338, no. 1, pp. 12–20, 2001.
- [70] J. Shaver, A. N. G. Parra-Vasques, S. Hansel, O. Portugall, C. H. Mielke, M. von Ortenberg, R. H. Hauge, M. Pasquali, and J. Kono, "Alignment Dynamics of Carbon Nanotubes in Pulsed Ultrahigh Magnetic Fields," *ACS Nano*, vol. 3, p. 131, 2009.
- [71] S. Zaric, G. N. Ostojic, J. Kono, J. Shaver, V. C. Moore, R. E. Smalley, R. H. Hauge, and X. Wei, "Estimation of Magnetic Susceptibility Anisotropy of Carbon Nanotubes Using Magneto-Photoluminescence," *Nano Lett.*, vol. 4, pp. 2219–2221, 2004.
- [72] M. A. L. Marques, M. d'Avezac, and F. Mauri, "Magnetic response and NMR spectra of carbon nanotubes from ab initio calculations," *Phys. Rev. B*, vol. 73, p. 125433, 2006.
- [73] O. N. Torrens, D. E. Milkie, H. Y. Ban, M. Zheng, G. B. Onoa, T. D. Gierke, and J. M. Kikkawa, "Measurement of chiral-dependent magnetic anisotropy in carbon nanotubes," *J. Am. Chem. Soc.*, vol. 129, no. 2, pp. 252–253, 2007.
- [74] T. A. Searles, Y. Imanaka, T. Takamasu, J. A. Fagan, E. K. Hobbie, H. Ajiki, and J. Kono, "Large Anisotropy in the Magnetic Susceptibility of Metallic Carbon

- Nanotubes,” *Phys. Rev. Lett.*, vol. 105, no. 017403, 2010.
- [75] X. Huang, R. S. Mclean, and M. Zheng, “High-resolution length sorting and purification of dna-wrapped carbon nanotubes by size-exclusion chromatography,” *Anal. Chem.*, vol. 77, pp. 6225–6228, 2005.
- [76] J. A. Fagan, M. L. Becker, J. Chun, P. Nie, B. J. Bauer, J. R. Simpson, A. Hight-Walker, and E. K. Hobbie, “Centrifugal Length Separation of Carbon Nanotubes,” *Langmuir*, vol. 24, pp. 13880–13889, 2008.
- [77] M. S. Arnold, A. A. Green, J. F. Hulvat, S. I. Stupp, and M. C. Hersam, “Sorting carbon nanotubes by electronic structure using density differentiation,” *Nature*, vol. 1, p. 60, 2006.
- [78] X. Tu, S. Manohar, A. Jagota, and M. Zheng, “DNA sequence motifs for structure-specific recognition and separation of carbon nanotubes,” *Nature*, vol. 460, pp. 250–253, 2009.
- [79] K. Yanagi, Y. Miyata, and H. Katura, “Optical and Conductive Characteristics of Metallic Single-Wall Carbon Nanotubes with Three Basic Colors; Cyan, Magenta, and Yellow,” *Appl. Phys. Exp.*, vol. 1, p. 034003, 2008.
- [80] E. H. Haroz, W. D. Rice, B. Y. Lu, S. Ghosh, R. H. Hauge, R. B. Weisman, S. K. Doorn, and J. Kono, “Enrichment of Armchair Carbon Nanotubes via Density Gradient Ultracentrifugation: Raman Spectroscopy Evidence,” *ACS Nano*, vol. 4, no. 4, p. 1955, 2010.

- [81] T. Asano, K. Koyanagi, S. Matsumoto, T. Kiyoshi, M. Kosuge, M. Yuyama, A. Sato, H. Wada, M. Hoshino, and Y. Dozono, “Resistive insert magnet for a 37.3T hybrid magnet,” *Physica B*, vol. 294-295, pp. 635–638, 2001.
- [82] S. Zaric, *Optical Spectroscopy of Single-Walled Carbon Nanotubes in High Magnetic Fields*. PhD thesis, Rice University, 2007.
- [83] A. Rodger and B. Norden, *Circular Dichroism and Linear Dichroism*. Oxford: Oxford University Press, 1997.
- [84] N. Nair, M. L. Usrey, W. Kim, R. D. Braatz, and M. S. Strano, “Estimation of the (n,m) Concentration Distribution of Single-Walled Carbon Nanotubes from photoabsorption spectra,” *Anal. Chem.*, vol. 78, pp. 7689–7696, 2006.
- [85] J. A. Fagan, V. Bajpai, B. J. Bauer, and E. K. Hobbie, “Anisotropic polarizability of isolated semiconducting single-wall carbon nanotubes in alternating electric fields,” *Appl. Phys. Lett.*, vol. 91, p. 213105, 2007.
- [86] Y. Murakami, E. Einarsson, T. Edamura, and S. Maruyama, “Polarization dependence of the optical absorption of single-walled carbon nanotubes,” *Phys. Rev. Lett.*, vol. 94, p. 087402, 2005.
- [87] M. F. Islam, D. E. Milkie, O. N. Torrens, A. G. Yodh, and J. M. Kikkawa, “Magnetic heterogeneity and alignment of single wall carbon nanotubes,” *Phys. Rev. B*, vol. 71, p. 201401(R), 2005.

- [88] J. P. Boyd, "Evaluating of Dawson's Integral by solving its differential equation using orthogonal ration Chebyshev functions," *Applied Mathematics and Computation*, vol. 204, pp. 914–919, 2008.
- [89] H. Ajiki, "Supplementary Information on the Theoretical Calculations of the Magnetic Susceptibility of Single-Walled Carbon Nanotubes," *Phys. Rev. Lett.*, vol. 105, no. 017403, 2010.
- [90] L. Cognet, D. A. Tsybouski, J. R. Rocha, C. D. Doyle, J. M. Tour, and R. B. Weisman, "Stepwise Quenching of Exciton Fluorescence in Carbon Nanotubes by Single-Molecule Reactions," *Science*, vol. 316, p. 1465, 2007.
- [91] E. W. Weisstein. "Exponential Integral". Internet Resource. Accessed on 31 July 2011. <http://mathworld.wolfram.com/ExponentialIntegral.html>.
- [92] A. Srivastava and J. Kono, "Diffusion-Limited Exciton-Exciton Annihilation in Single-Walled Carbon Nanotubes: A Time-Dependent Analysis," *Phys. Rev. B*, vol. 79, p. 205407, 2009.
- [93] W. D. Rice, "Electron Dynamics in Single-Walled Carbon Nanotubes," Master's thesis, Rice University, 2009.
- [94] M. Jones, C. Engtrakul, W. Metzger, R. Ellingson, A. Nozik, M. Heben, and G. Rumbles, "Analysis of photoluminescence from solubilized single-walled carbon nanotubes," *Phys. Rev. B*, vol. 71, p. 1, 2005.

- [95] A. Nish, J. Hwang, J. Doig, and R. J. Nicholas, "Highly selective dispersion of single-walled carbon nanotubes using aromatic polymers," *Nature Nanotech.*, vol. 2, p. 640, 2007.